A MESOSCALE STUDY OF FRONTAL AIRFLOW, MOISTURE, AND CUMULUS CONVECTION

by

ROBERT JOHN PAINE

S.B., State University of New York at Albany
1973

SUBMITTED IN
PARTIAL FULFILLMENT
OF THE REQUIREMENTS FOR THE
DEGREE OF MASTER OF SCIENCE
at the
MASSACHUSETTS INSTITUTE OF
TECHNOLOGY

January, 1975

Signature of Author _____
Department of Meteorology, January 17, 1975

Certified by _____
Thesis Supervisor

Accepted by _____
Chairman, Departmental Committee
on Graduate Students

A Mesoscale Study of Frontal Airflow, Moisture, and Cumulus Convection

by

Robert J. Paine

Submitted to the Department of Meteorology on January 17, 1975, in partial fulfillment of the requirements for the degree of Master of Science.

ABSTRACT

A convectively active cold front which passed through the National Severe Storms Laboratory (NSSL) network in Oklahoma on 14 May 1970 is examined to determine the mesoscale structure of the motion, temperature, and humidity fields, and the interaction of these fields and the convection. One objective of this study is to find out how the preliminary convection modified the mesoscale environment so as to support the major convective line aloft, 20 to 40 km behind the surface front. Analyses are based upon data from 42 rawinsonde ascents to the 400 mb level, 44 automatically recording surface stations, and continuous radar PPI coverage.

The distribution of vertical motion, determined by the conventional kinematical technique, shows a strong downdraft of more than 3 m sec^{-1} in the middle and upper troposphere above the frontal wind-shift line at the surface, and an updraft of greater than 2 m sec^{-1} at the same levels, 35 km behind the line. However, calculations based upon balloon ascent rates do not confirm this pattern, and leave some doubts concerning its correctness. On the

other hand, the values of vertical motion derived from the balloon ascent rates are also suspect; and there is evidence that the balloon soundings in the region of vigorous convection do not represent an unbiased sample of the mesoscale mean. The kinematical version of the vertical motions is considered to be the best available and it is used throughout the rest of the paper.

Individual time derivatives of mixing ratio, potential temperature, and equivalent-potential temperature, following the mesoscale motion, show much evaporative cooling in the area of descent and condensation and warming in the ascent region. Typical modification rates are of the order of 0.05×10^{-3} per minute for mixing ratio and 0.1 deg C per minute for potential and equivalent-potential temperature. A comparison of these changes to estimates of the (presumably convective) eddy transports, in the case of equivalent-potential temperature, shows qualitative consistency.

Calculations for a simple steady-state convective-plume model suggest, however, that the temperature and moisture stratification is no more favorable for convection near the line of cumulonimbus and intense radar echoes than in the area of scattered-to-broken cumulus congestus ahead of the front. Therefore, the heavy convection cannot be explained in this case by mesoscale modification of the static structure of the air column. It appears, rather, that the more intense convection occurs because the horizontal size of the convective elements is greater, for reasons which this analysis cannot provide.

Thesis Supervisor: Frederick Sanders

Title: Professor of Meteorology

TABLE OF CONTENTS

LIST OF ILLUSTRATIONS

1. Introduction

Direct measurements of the effects of the environment upon cloud and precipitation structures and the effects of the vertical transfer of momentum, heat, and water vapor by clouds upon the environment have been made on a limited basis in the past. The majority of studies have been concerned with an air-mass storm, a single supercell, or a squall line case. The primary focus of investigation has been upon airflow in and around storms and the motion of convective cells relative to environmental winds. Examples of such studies include those by Fankhauser (1969, 1971, 1974) and Newton and Newton (1959), among others.

Detailed measurements are especially needed on a mesoscale basis, since synoptic-scale observations are inadequate for the resolution of convective processes. In response to this need, the National Severe Storms Laboratory (NSSL) established a mesoscale rawinsonde network in Oklahoma in 1966, supplemented by surface stations, instrumented aircraft, and radar.

A detailed mesoscale analysis of a convectively active cold front that passed through the NSSL network on 14 May 1970 is presented here using analysis techniques similar in some respects to those used by Fankhauser (1969, 1974) in other case studies. The considerable amount of data gathered during this storm includes data from 44 automatically recording surface stations, 58 rawinsonde ascents originating at nine launch sites, and continuous PPI radar coverage at elevations from 0 deg to 20 deg. This data set is one of the most complete and extensive of all of the storm cases documented at the NSSL network from 1966 through 1970 (Barnes et. al., 1971).

One of the objectives of this paper is to determine the influence of convection upon the mesoscale environment, with the aid of a one-dimensional, steady-state cloud model. Another goal is to calculate individual time derivatives of mixing ratio, potential temperature, and equivalent-potential temperature, following the mean mesoscale motion. There are appreciable rates of change of equivalent-potential temperature, due mostly to vertical eddy fluxes. Rough estimates of these fluxes are used to attempt to establish qualitative agreement between the mean-motion and eddy fluxes of equivalent-potential temperature.

2. Synoptic situation

The synoptic features at 1600 CST, 14 May 1970 (0000 GMT, 15 May 1970) are shown in Fig. 1. In the surface analysis, a cold front extends from northern Indiana and Illinois southwestward into New Mexico. This front is just entering the northwest corner of the NSSL network at 1800 CST, progressing southeastward at a speed of about 24 km hr^{-1}. Squall-line and air-mass showers are occurring ahead of the front, using the broad southeasterly flow from the Gulf of Mexico as a moisture source. The surface analysis shows a pronounced frontogenetical deformation in the wind field along the cold front.

The 400-mb analysis features a deep short-wave trough in the upper Great Plains with a weak extension into western Oklahoma and Texas. The region of strongest winds is located well to the north of Oklahoma. An ageostrophic wind reported at Abilene, Texas, is possibly the result of local convective activity.

3. Observations and organization of data

a. surface observations

In 1970, the NSSL network included 44 automatically recording surface stations in a 70-km-square area in central Oklahoma. Each station was equipped to measure wind direction and speed, temperature, relative humidity, pressure, and rainfall.

The sequence of sky conditions at a typical station on 14 May 1970 in central Oklahoma was as follows. There was a cirrostratus overcast present essentially all day. Before the cold front arrived in late afternoon or early evening, scattered-to-broken cumulus congestus were observed, with cumulonimbus clouds in the northwest quadrant. As the cold front passed, a low overcast started to move in, accompanied by thunder and lightning to the north and west. Rain began fifteen minutes to one hour after the surface wind shift and it lasted for several hours. The rainfall was between light and moderate in intensity and was accompanied by frequent lightning in its early stages.

A study of the surface winds reveals that an abrupt wind-shift line progressed steadily through the network at an average speed of 24 km hr^{-1}. Fig. 2 shows the distribution of surface stations and the advance of the line of the surface wind shift (hereafter referred to as SWS). A coordinate system moving with the front is shown in Fig. 2. The y-axis, where use is made of it, passes through the radar site.

Before the arrival of the SWS line, the wind at a typical station blew steadily from a direction between southeast and south-southwest. The frontal passage was marked by a decrease in wind

speed, followed by a wind shift to a direction between northwest and northeast. This event took place in a one- to three-minute period in general and was followed by moderate gusts and variations in wind direction. Widespread precipitation at the surface did not commence at most stations until 40 to 70 minutes after the SWS passage.

Although this system might be regarded as a squall line because of the associated thunderstorm activity, there is evidence to support the fact that a true front, separating two different air masses, passed through the network. After the wind shifted at each station, no instance of a southerly wind component was reported. Surface temperatures fell steadily from the middle twenties to the middle teens (deg C) without showing any signs of recovery. In addition, there is no evidence that the SWS line was a result of a downdraft-produced gust-front, which often accompanies squall lines.

b. rader data

The 10-cm WSR-57 radar used in the NSSL network presents a PPI isoecho-contoured display of the effective reflectivity factor, Z_e, at 10-decibel Z_e (or 1-log Z_e) intervals. A sequence of PPI sweeps starts at 0 deg elevation, followed by an automatic increase of one or two degrees in the elevation angle with each successive sweep, to a maximum of 20 deg. The radar pictures from the 14 May 1970 storm have been used to identify the location of surface rainfall and to study the relative positions of updrafts and downdrafts. In addition, cloud-top heights and liquid-water distributions have been examined. Meneely (1972) made extensive use of the radar data available for this case in his preliminary study of the 14 May 1970 storm.

c. rawinsonde data

From a total of 58 available balloon ascents, this study utilizes 42 rawinsondes that were launched during a five-hour period within the NSSL network. In accordance with project requirements, tracking of rawinsondes was ceased at about the 400-mb level, except during relatively quiescent weather, in order to maximize the number of launches. Balloons were not launched at any particular predetermined time, nor were they released in conjunction with others at different stations, since past experience had shown that coordinated launches did not result in optimum data coverage (Barnes et. al., 1971).

While the collection of data for this case is impressive by ordinary standards, it is not sufficiently dense to be used in resolving the effects of individual convective cells in all three spatial dimensions and in time. However, the organization of the storm system into a well-defined line and the short time span of the observations suggest the assumptions of a steady-state system and of no appreciable variations of meteorological quantities along the x-axis as defined in Fig. 2. Therefore, a transverse display of variables has been adopted. Rough measurements of variations along the x-axis and in time generally confirm the validity of the above assumptions, although nonuniformities certainly do exist.

Smoothing techniques are used to suppress unwanted details of vertical structure, in a manner similar to that of Fankhauser (1969). The rawinsonde data is averaged vertically in 50-mb layers. Where data is missing or is doubtful, interpolation is used in order to complete the data set. A horizontal running mean of meteorological quantities is obtained by averaging data from about ten adjacent

balloons for each layer, then attributing that average value to the centroid of the balloon positions.

Some balloons became so weighted down with ice that they descended; the descending portions are not used in this study. Other balloons entered high speed updrafts. Any rawinsonde-measured value of wet-bulb potential temperature (or equivalent-potential temperature) that exceeds the highest (low-level) temperature that is an average of ten observations is set equal to that highest temperature. A similar method is carried out for a lower bound on temperature. The limits actually used in this study are 16 deg C and 22 deg C for wet-bulb potential temperature.

The density of the vertically averaged rawinsonde data in the y-p plane is shown in Fig. 3. There are several points where two or three balloons are superimposed. The horizontal averaging scheme is demonstrated at one of the levels by seven groups of circled data points. The resulting seven columns of horizontal centroids of balloon groups are also shown. In appendix A, a special averaging technique that deals effectively with extreme measurements, some of which appear in the data, is discussed.

Derivatives in y and p of any quantity, where needed, are calculated using finite differences. Values at grid points of a rectangular mesh are obtained by means of subjective analysis. The pressure interval is 50 mb, while the interval in the y-direction is 8 km (or 20 min). Derivatives in the x-direction are calculated by dividing the balloons into two equal groups by means of a line parallel to the y-axis in each 50-mb layer. In each of the seven balloon groups shown in Fig. 2, there are about five balloons on each side

of the dividing line. An average value for any quantity of interest is calculated for the five observations, and is assigned to the centroid of the balloon positions. Analysis and finite differencing follow, using a mesh length of about 40 km.

Fankhauser (1969) advises that releases of balloons into convective storms should be avoided because of possible equipment failure and the unresolvability of scales of motion of the size of convective cells. In 1970, however, there were attempts to launch balloons into active cells by NSSL personnel (Henderson, 1971). Evidence that some balloons entered updrafts (and survived) during the 14 May 1970 storm is presented in the next section. The configuration of the storm, which permits compositing of data into a two-dimensional display, increases the resolution to the extent that the gross influences of cumulus convection can be examined.

4. Distribution of meteorological variables

a. identification of cloud and environmental soundings

In this paper, the properties of the mean mesoscale atmosphere (including both clouds and environment) are examined. However, in a later section, a one-dimensional cloud model is used to simulate convection. The properties of the environment must be known in order to use the model. Here, only updrafts are excluded from the mean in order to determine the environment, since most downdrafts are located well behind the convective line, away from the area of interest for the cloud model calculations, as will be seen below.

It is necessary to examine individual soundings to determine whether any of them entered convective updrafts or downdrafts. In order to do this, the vertical velocity of the air through which each balloon rose must be determined. This calculation requires a knowledge of a balloon's still air ascent rate as a function of pressure. Since balloon heights are calculated hydrostatically, it is necessary to assume that the errors in the computed in-cloud heights are small. This assumption is also used by Davies-Jones (1974), who finds that dynamic corrections applied to the hydrostatically-determined heights are insignificant. Davies-Jones also discusses a source of height error due to the fact that the vertical profile of temperature above a single point is not known, since the balloons do not rise vertically. This problem is not considered to be significant, even though large horizontal gradients of temperature exist in this frontal case. Precipitation and icing tend to slow the balloon's rate of ascent. They are discussed below.

Two methods are used in this study to find the still-air ascent rate of balloons. One involves theoretical considerations supplemented by experiments, while the other utilizes pre-frontal ascent rates using rawinsondes that were launched at least one hour before the SWS arrived, when the vertical motion of the air was presumably slight. Thirteen such ascents are available. In appendix B, the details of the theoretical and experimental calculations are discussed, and results are found to agree well with pre-frontal observations. Both indicate that the ascent rate of the balloons increases from about 6 m sec^{-1} at the ground to about 7 m sec^{-1} at 400 mb.

For each individual balloon throughout the entire area of analysis, the still air ascent rate near the ground is assumed to be the balloon's actual ascent rate in the lowest 200 meters. In most cases, this rate is between 5.5 m sec^{-1} and 6.5 m sec^{-1}. For any balloons whose initial ascent rate is lower than 5.5 m sec^{-1} (such as those affected by precipitation or icing), the still air ascent rate is assumed to increase by 1 m sec^{-1} over its ground value by the time that the 400-mb level is reached. This method, which utilizes a variable initial ascent speed, is a crude attempt to alleviate the error introduced by the effects of precipitation. The effects of icing, which occur at high altitudes, are very difficult to deal with.

In addition to ascent-rate measurements, equivalent-potential temperatures are used to identify updraft and downdraft soundings. Positive and negative anomalies in the equivalent-potential temperature measurements are used to trace positively and negatively buoyant air parcels, respectively.

Updrafts are assumed to be characterized by vertical motions exceeding +4 m sec^{-1} in at least two adjacent 50-mb layers and simultaneously by θ_e values higher than the mean of about ten observations by at least 3 deg K. There are very few cases above 800 mb in which only one requirement is satisfied. Downdrafts are similarly identified by vertical velocities less than -2 m sec^{-1}, accompanied by θ_e values colder than the mean by at least 3 deg K in at least two adjacent 50-mb layers. There are several cases in which the vertical-motion requirement is satified for downdrafts, but not the θ_e requirement. These balloons were probably being impeded by precipitation and/or icing.

Figure 4 is an x-y plot of the horizontal projections of the paths of the 42 rawinsonde balloons, relative to the moving front. Updrafts, downdrafts, and precipitation and/or icing regions are identified as explained above. One interesting feature is the configuration of updrafts and downdrafts with respect to each other. With the aid of the radar data, it is found that most of the updrafts are located a few km ahead of the echoes. Downdrafts are evident behind the echoes.

Radar PPI displays at half-hour intervals are shown in Fig. 5, along with the position of the SWS line and any balloons that were in the air at the time of each display. Individual balloons shown can be compared by number with those in Fig. 4. Zero elevation contours of log Z_e are shown along with the lowest detectable Z_e contour (log Z_e = 1) at anvil level. The arrangement of the convective cells in a line is apparent in all displays.

Near 1800 CST, most balloons were being sent up ahead of the SWS line. By 1830, the line had advanced farther into the network, and the convection was somewhat more consolidated. A few isolated echoes appeared ahead of the SWS line in the vicinity of Chickasha, the southwesternmost rawinsonde station. At 1900 CST, pronounced anvils appeared downwind of the line of cells. One balloon (#5) was entering an updraft in an echo-weak region and another (#4) was caught between two echoes as it suddenly acquired a large horizontal velocity in its passage. The system had undergone significant development by 1930 CST with a line of growing cells in front of a line of dying ones. Anvils were more fully developed, and more updraft soundings were being made. By 2000 CST, ground clutter near the radar site started to interfere with the display of the advancing line of cumulus clouds. Then, as at 2030 CST, there were several balloons that were encountering either updrafts or precipitation and/or icing.

Generally speaking, most updraft soundings are located just in front of or slightly within the zero elevation radar echoes. In addition, echoes at anvil level (in particular, the most intense echoes at that level, which are not reproduced here) are located in front of those at zero degrees elevation, except for the anvils themselves. This observation reveals the rearward (downwind) sloping of raindrop trajectories. The location of anvils behind the main cell line clearly shows the direction of the wind shear. In the vicinity of the most intense cells, there is much penetrative convection above the anvil line.

Figure 6 shows one of Meneely's figures (1972), which is worthy of reproduction here. Tracks followed by individual cells revealed by the radar display between 1730 and 2220 CST are shown. These positions are based upon zero elevation PPI pictures which show the locations of falling rain rather than cell updrafts. The position at ten-minute intervals of the most intense part of each cell is plotted for all of those cells that were identifiable for at least three consecutive ten-minute times. Broken lines connect the locations of the strongest cells at half-hour intervals. The cell isochrones tend to progress southeastward at an irregular speed, in contrast to the more uniform advance of the SWS line. Rapid advances of the line of cells occurs when a new line forms a few km ahead of the existing line. As the newly-formed cells develop and the old ones weaken, a discontinuous advancement of the cell line results. Figure 6 shows this occurring between 1800 and 1830 CST and also between 1900 and 1930 CST.

The paths taken by individual cells are in almost all cases to the right of the upper level environmental winds, which are shown in the figure. Newton and Newton (1959) show that this movement is accomplished by a nonhydrostatic vertical pressure gradient on the side of a cell that is 90 degrees to the right of the downwind direction. This upward pressure force leads to continuous development of the cell on the right side so that it appears to be propagating toward the right of the environmental winds. This phenomenon is caused by the following mechanism. When air is forced to flow around a (cylindrical) cloud obstacle, there is a hydrodynamic pressure excess on the upstream side of the cloud and

pressure deficiencies on all other sides. Due to geostrophic warm advection on a synoptic scale, there is often a veering of the environmental wind with height, creating a pressure excess at low levels and a pressure deficiency at upper levels on the right flank of the cloud.

Outflow from any downdraft area tends to keep balloons away from such areas by mass continuity. Such an effect will cause, if anything, an underestimate of the fraction of downdraft areas in the environment. In the same way, updraft areas may be overestimated because of the tendency (theoretically, at least) for balloons to drift into them. As mentioned above, there were attempts by NSSL personnel to launch balloons into updrafts. This possibility and the entraining effect of updrafts are probably acting to introduce a bias (of undeterminable extent) toward a higher percentage of updrafts sampled by balloons.

Appendix C contains a sample calculation of inward drift velocities that a balloon near a symmetrically entraining cloud would encounter. It appears that in the 14 May 1970 case, however, the inflow into updrafts was one-sided in many instances due to the relative positions of updrafts and downdrafts that existed. It is possible that the inflow velocities in this case exceeded those which would exist near a symmetrically entraining cloud. The model calculation in appendix C implies that a balloon would have to be within 1 or 2 km of a vigorous updraft when launched in order to have a chance to be entrained into the updraft. Inward velocities of the model are somewhat less than 1 m sec^{-1} for a cloud with a radius of 1 km, but these velocities are roughly proportional to the

cloud radius. Therefore, large clouds have the greatest potential for the entrainment of balloons.

Due to the uncertainty in the fraction of updrafts, the presentation of meteorological quantities below involves two versions. One of them, referred to below as version A, supposes that the balloons were sampling the atmosphere in an unbiased manner, so that the high fraction of updrafts found is valid. Version B assumes that the areal extent of the updraft regions is overestimated by the balloon sampling process and that the mean moisture and temperature properties can be identified with the environment without too much error, as is done in cumulus parameterization schemes (e.g., Yanai et. al., 1973). In the second version, the maximum updraft areal coverage is considered to be about 10%.

b. horizontal wind components

In Fig. 7a, the version A distribution of the u-component of the wind with respect to the ground is shown. In Fig. 7b, the results of version B are displayed. In this and other variables to follow, the same limited updraft representation is kept in version B. The exact number of balloons used for both versions for each of the 84 mesoscale data points is shown in Fig. 7b (A on the left, B on right).

Southwesterly wind vectors (positive u values), which represent flow into the page, are evident above and ahead of the front. The front, a shallow feature, originates at the SWS line (time = 0 min, pressure = 970 mb), and slopes upward with increasing time. It is associated with large and negative values of u. A more exact definition of the frontal position can be made using the v-component

of the wind, which is discussed below. Note that the region of strongest u-components of wind aloft is located in the proper position for there to be a wind maximum on the right flank of the cumulonimbus clouds along the convective line. No significant difference is apparent between the two versions of the u-distribution shown.

In Fig. 7a, standard deviations of u are shown, assuming that the u-values are normally distributed. The probability of a sample observation falling within one standard deviation of the population mean (assuming a normal distribution) is 0.7056. Although this assumption about the population is not necessarily true in all cases, the standard deviation of the samples of about ten (possibly unrepresentative) observations is used to indicate the variability within each sample. In this case, the highest values of the standard deviation of u, σ_u, are found in the region of active cells near +50 min and at later times near what appears to be a poorly defined section of the frontal surface. In the vicinity of the convective line, the turbulence caused by the presence of cell obstacles seems to be responsible for the high values of σ_u there. The cause of high σ_u values at +100 min and 700 mb is discussed below. There is a low variation in the u-values in front of the SWS line, where the air is relatively undisturbed.

Figure 8a shows the v-component of the wind field with respect to the ground, in the same manner that the u-component is presented. The frontal surface can be placed along the -6.7 m sec^{-1} isopleth, since that line represents zero motion with respect to the moving front.

Note a double minimum in the v-field at + 160 min. The lower minimum probably corresponds to the front, while the upper minimum is possibly caused by the convection.

A feature worth noting is the maximum speed near +50 min with a minimum on each side. It happens that the most intense radar echoes coincide with this maximum in v. This feature does not represent a geostrophic effect, since measurements show that $\partial v/\partial x$ is small, and is in fact negative at most points, inconsistent with the observed vertical shear.

The observation of larger v-components, on the average, in updrafts than in the environment is in conflict with the assumption that the horizontal momentum of cloud air is conserved as it is transported upward from cloud base. A comparison of updraft and environmental soundings for this case yields a result for the v-component of wind (using the coordinate system in Fig. 2) similar to that obtained by Davies-Jones and Henderson (1973). These authors used 33 pairs of updraft and environmental soundings from the NSSL archives, including seven such pairs from the 14 May 1970 storm. They found that the wind speed in updrafts is less than in the environment, primarily due to differences in the u-component of the wind. However, in this study, the wind speed in updrafts is larger than that in the environment, since the differences in the u-component are small. Where the v-component increases with height (as in this case for the lower troposphere), lower speeds would be expected in updrafts than in the environment, due to a positive viscosity effect. It is possible that the balloons involved in updrafts were not representative for scales of motion of the size of a cumulus cloud.

Another feature worth noting is the fluctuation in the sign of v in the vertical near -40 min, which might be due to a gravity wave that was induced by the approaching front, as suggested by Lindzen (1974).

Figure 8a shows the distribution of σ_v , the standard deviation of the v-component of the wind. Features that are apparent include a uniform behavior of winds in pre-frontal regions, followed by an increase in turbulence in the vicinity of the convective line. Surprisingly enough, the largest values of σ_v are not found near the line of severe weather, but instead they are well behind this line, at +100 min and 700 mb. A similar feature can be seen in the σ_u field. A close examination of the individual balloons that make up these averages reveals that while some balloons appear to have been in the warm air, with strong southerly components, others definitely exhibit northerly wind components and cold temperatures. The great variety of observations that make up the averages in this high σ_v area is not due to a variation of v in the x-direction, but rather to a strong gradient in y, as well non-steady-state secular changes, within the area being averaged.

c. vertical motion

From the v-component of the wind, the vertical motion can be determined by vertically integrating the equation of continuity. The explicit formulas involved are

$$\omega(y,p) = \omega_{sfc}(y) + \int_{p}^{p_{sfc}} \frac{\partial v}{\partial y} \, dp \quad , \qquad (1a)$$

and

$$w(y,p) = \omega(y,p) \,/[\zeta(p)\, g] \qquad . \qquad (1b)$$

Small contributions due to $\partial u/\partial x$ and the non-steady-state effects which influence $\partial v/\partial y$ are also included in this calculation. These effects arise from the fact that observations made at a single y-coordinate are not taken at the same clock time, creating a confusion between derivatives in space and in time. The quantity measured in this study, $\frac{\partial v}{\partial y}(x,p)$, can be expressed as

$$\frac{\partial v}{\partial y}(x,p) = \frac{\partial v}{\partial y}(x,p,t) + \frac{\partial v}{\partial t}(y,x,p)\ \frac{\partial t}{\partial y}(x,p) \qquad . \qquad (2)$$

For a steady-state system, the second term on the right is zero and the measured quantity, $\frac{\partial v}{\partial y}(x,p)$, is the same as the desired quantity, $\frac{\partial v}{\partial y}(x,p,t)$. In this case, however, $\frac{\partial v}{\partial t}(y,x,p)$ is not zero. The local time derivative is isolated by comparing v-values from five blocks of real time, each 75 min long, at each fixed y-coordinate in the vertical cross section. The $\frac{\partial t}{\partial y}(x,p)$ factor is just the conversion between time and space derived from the steady propagation of the front. A correction to the calculated values of $\frac{\partial v}{\partial y}$ is applied using (2).

Vertical motions due to derivatives in time and in the x-direction are typically of the order of 0.1 m sec^{-1}, but they are as large as 0.4 m sec^{-1} near 400 mb. The assumption that ω is zero at the ground is made because the effects of orography and of local rates of change and horizontal advections of pressure at the surface generate vertical motions of only a few cm sec^{-1}.

Figure 9a shows version A of the vertical motions computed by the kinematical method. In addition, the vertical-motion distribution obtained from net balloon ascent rates (version A) is included in the figure. There is poor agreement between the two fields. Main areas

of disagreement are caused by the large maximum in net balloon ascent rates at +50 min, and by the region of downdrafts near the SWS line in the kinematically-determined vertical-motion field. The balloon-updraft maximum coincides with the location of updraft soundings, while the kinematically-determined vertical motions are related to the mesoscale convergence and divergence distribution. The latter version is subject to the accumulation of errors in wind analyses with height in the integration process.

Figure 9b shows version B of the vertical motions computed from (1). A superimposed field of version B of the net balloon ascent rates is included. While the deletion of most updraft soundings does not change the kinematically-determined vertical-motion field much, the net balloon ascent rates are considerably altered. There is much better agreement in both position and magnitude of the updraft maximum between the two superimposed fields in Fig. 9b than in Fig. 9a. However, there is still disagreement over the intensity of the downdraft.

Another version (denoted as C) of the vertical-motion field involves the imposition of an upper boundary condition composed of net balloon ascent rates, version B. The motivation behind the use of an upper boundary condition is the fact that errors in wind analyses tend to accumulate with height during integration of the continuity equation, leading to the most uncertain values at upper levels. The method used in this study to adjust the vertical motion and divergence fields so that they match the upper boundary condition is taken from O'Brien (1970). His scheme provides for satisfying both upper and lower boundary conditions, while achieving most of the compensation at

the upper levels where the accumulations of errors produces the most doubtful result. The adjusted divergence, D', and vertical velocity, ω', can be expressed as

$$D'_k = D_k + \frac{k}{M} (\omega_K - \omega_T) / \Delta p \qquad (3)$$

and

$$\omega' = \omega - (\omega_K - \omega_T) \frac{k}{2M} (k + 1) \quad , \qquad (4)$$

where

$$M = \sum_{k=1}^{K} k = \tfrac{1}{2} K(K + 1) \quad . \qquad (5)$$

In the above equations, K is the total number of layers, while k refers to individual layers. In (3), ω_K is the imposed boundary value for ω at the top of the atmospheric column under consideration and ω_T is the computed value at the top before correction. In this case, the divergences are computed using a pressure interval of 50 mb. Figure 9c shows the vertical-velocity distribution obtained from (4). The greatest adjustments are found in the pre-frontal region, where the strength of the downdraft is considerably weakened. The updraft maximum is displaced slightly to the left of its position in Fig. 9b.

The credibility of the net balloon ascent rates is assessed by using the continuity equation to determine the v-field from the given ω-distribution. Variations in x and in time are ignored. The resulting two-dimensional stream function is calculated with the aid of the formulas

$$\omega = \frac{\partial \psi}{\partial y} \qquad (6a)$$

and

$$v = - \frac{\partial \psi}{\partial p} \quad . \qquad (6b)$$

For a boundary condition, the values of v at -40 min are used for all versions because of their high reliability (as shown by their low standard deviation). The mass flow is represented by the spacing of the streamlines in each display. These streamlines can be compared to the streamlines which are calculated from version A of the v- and ω-components of the wind, altered slightly by the effects of variation in x and in time. This latter set of streamlines is referred to below as the "observed" version. The observed trajectories approximately indicate the rate of mass flow by their spacing.

The results of the computations of v and Ψ from versions A and B of the net balloon ascent rates, and from version C of the vertical motions, are shown in Figs. 10a and 10b, 10c and 10d, and 10e and 10f, respectively.

The horizontal velocities shown in Fig. 10a are rather incredible on the left side of the figure, with speeds greater than 70 m sec^{-1} in one area. This result implies that version A of the net balloon ascent rates does not accurately represent the vertical-motion distribution. The difference in the rate and direction of mass flow between the set of streamlines resulting from the velocities in Fig. 10a and the observed version is evident in Fig. 10b.

The v-field derived from version B of the net balloon ascent rates is shown in Fig. 10c. Although it is more believable than the field shown in Fig. 10a, this distribution bears little resemblence to the observed (version A) distribution. The streamlines in Fig. 10d differ most from those observed at times later than +80 min near the 700-mb level, but this difference is not as great as it is in Fig. 10b.

The closest representation to observed conditions is displayed in Figs. 10e and 10f, which represent the version C streamlines. The average deviation of these computed horizontal velocities from the observed ones is about 5 m sec^{-1} in regions away from the right edge of the figure. In this case, the "observed" velocities are accepted instead of the ones shown in Fig. 10e because the error involved in the calculation of net balloon rates is probably greater than that due to vertical integrations of horizontal wind divergence, even at the 400-mb level. Errors due to icing effects, which can amount to several m sec^{-1} in severe cases for net balloon ascent rates, are generally confined to high levels (above 500 mb) and to times after +100 min. Therefore, an upper boundary condition is not used for such times. Instead, version A is used. The general pattern shown in Figs. 10e and 10f closely resembles the observed one and it is used throughout the rest of this paper in computing transports of thermodynamic quantities, as an alternative version.

The greatest unsolved mystery encountered in this paper so far is the disagreement in the strength of the downdraft above the SWS line between the kinematically-determined vertical velocities and the net balloon ascent rates. The amount of horizontal divergence occurring in this region depends upon the validity of the maximum in the v-field near +50 min. It can be seen from Figs. 8a, 8b, and 9b that even without the majority of updraft soundings, which generally have higher than average horizontal velocities, the intense downdraft still exists. The net balloon ascent rates are probably in error by no more than 1 m sec^{-1}. This error can arise from incorrect values for the still air ascent rate and to precipitation and icing. Such

errors should be minimized in the downdraft region above the SWS line because of the relative uniformity of the measurements and the lack of precipitation or icing. Of the twelve balloons that rose in this region, there are only two that passed through (thin) layers with relative humidities greater than 95%. This information indicates that the balloons were generally not successfully entrained into updrafts, a result which discounts the possibility of a biased view of the vertical-motion field. In one of the following sections, the balloon-measured values of θ_e are examined to further assess the tendency for balloons with above-average vertical velocities to be associated with high θ_e values, which are frequently associated with updrafts at high levels.

d. equivalent-potential temperature

The field of equivalent-potential temperature (version A) is shown in Fig. 11a. Also shown is the standard deviation field of θ_e. Note the large area of potential instability above 800 mb, especially in regions ahead of and near the convective line. In version B (Fig. 11b), the area near +60 min has smaller values of θ_e than version A, and thus it has a larger amount of potential instability in that region. A pre-frontal warm, moist tongue of air at low levels is evident along with a cold mid-tropospheric layer. The area in the cold air near +160 min has a double minimum of θ_e, a structure similar to that of the v-component of the wind in that region (see Fig. 8a).

The standard deviation field of θ_e has maxima in two places where they may be expected. One area is in the region of the most fully developed convection, and the other is located where the frontal

surface is rather ambiguous (at times later than +80 min, and pressures between 900 and 700 mb). As in displays of standard deviation for other variables, there are minima at the left and especially at the right portions of the figure.

In Fig. 11b, the observed trajectories are superimposed upon the θ_e distribution in order to get a qualitative idea of the rate of change of θ_e following the mean motion. It is evident that the mean mesoscale air flow is not moist-adiabatic ahead of and at the line of convective cells, but the trajectories are nearly parallel to the isopleths of θ_e in the area behind the convective line. The rates of change of equivalent-potential temperature following the motion are quantitatively examined below.

e. potential temperature

Figure 12a shows the version A distribution of potential temperature, θ, with the standard deviation field superimposed. The θ field is rather flat and featureless aloft, but the contrasts of temperature across the front are evident near the surface. The standard deviation of potential temperature has a pronounced maximum in the middle and upper troposphere at the location of the convective line. There is a suggestion of a maximum in the region where the front is not clearly defined, as discussed above. As before, minima are present at the right and left edges of the figure.

In Fig. 12b, the version B representation of the θ field is pictured with superimposed trajectories. The potential temperature values at upper levels in this figure are slightly lower than those at the same levels in Fig. 12a. As a result, the thermodynamic stability

of version A is greater than that of version B. A corresponding observation can be made for the case of θ_e. A qualitative notion of the rate of change of θ along the mesoscale flow can be obtained by examining Fig. 12b. Changes of θ along the mean motion occur where there is appreciable upward or downward motion, since the isentropes are remarkably close to being horizontal.

f. mixing ratio

The presentation of the mixing ratio (q) fields is analagous to that of θ and θ_e. Figure 13a displays version A of the q distribution, plus the standard deviation field. The "ridge" of q values corresponds to the high humidity region of the convective line. The standard deviation values are similar in most respects to those discussed for other quantities. As pressure decreases, there is, of course, a limit to the maximum value of q and also its standard deviation.

As one might expect, the values of mixing ratio at upper levels are higher in Fig. 13a than in Fig. 13b, because of the deletion of the moist updraft soundings in the latter figure. The change of q following the streamlines in Fig. 13b shows an area of evaporation in the descent region and one of condensation in the area of ascent.

g. relative humidity

The field of relative humidity is shown in Figs. 14a and 14b. The presentation is like that of previous variables. There is a dry region in the upper right corner of both versions of the distribution. This area is separated from the region of greater than 90% relative humidity by a steep gradient. The maximum intensity of rainfall

(shown in Fig. 15a) is near +85 min, so that the region of maximum relative humidity is in the updraft area ahead of most of the rain. The standard deviation field has its highest value in the large gradient region at upper levels, where developing clouds are interacting with a dry environment. Since the relative humidity values are generally between 70 and 90 per cent in the area to the left of the high gradient region, there is no region of high standard deviation in the lower left portion of the diagram where large variations are evident for other variables.

In Fig. 14b, the flow along streamlines shows a large increase in the relative humidity in the descent region, an observation contrary to normal experience (e.g., chinook winds). The increase in relative humidity is made possible by the large increase in q following the motion (Fig. 13b). This curious increase in the moisture of the descending air parcels is one of the objects of investigation of this study.

5. Mesoscale moisture and temperature budgets

a. conceptual discussion

The total rate of change of any quantity Q can be written as

$$\dot{\bar{Q}} = \frac{\partial \bar{Q}}{\partial t} + \frac{\partial}{\partial x}(\bar{u}\bar{Q}) + \frac{\partial}{\partial y}(\bar{v}\bar{Q}) + \frac{\partial}{\partial p}(\bar{\omega}\bar{Q}) + \frac{\partial}{\partial x}(\overline{u'Q'}) + \frac{\partial}{\partial y}(\overline{v'Q'}) + \frac{\partial}{\partial p}(\overline{\omega'Q'}). \quad (7)$$

A region where $\dot{\bar{Q}}$ is positive will be referred to as a "true source." The quantity $\dot{\bar{Q}}$ can be divided into two parts,

$$\dot{\bar{Q}}^* = \frac{\partial \bar{Q}}{\partial t} + \frac{\partial}{\partial x}(\bar{u}\bar{Q}) + \frac{\partial}{\partial y}(\bar{v}\bar{Q}) + \frac{\partial}{\partial p}(\bar{\omega}\bar{Q}) \quad (8a)$$

and

$$\dot{\bar{Q}}^V = \frac{\partial}{\partial x}(\overline{u'Q'}) + \frac{\partial}{\partial y}(\overline{v'Q'}) + \frac{\partial}{\partial p}(\overline{\omega'Q'}) \quad , \quad (8b)$$

where primed quantities are deviations from the mean (overbarred quantities). Areas of positive values of $\dot{\bar{Q}}^*$ are called "apparent sources." If $\dot{\bar{Q}}$ is zero, then $\dot{\bar{Q}}^* = -\dot{\bar{Q}}^V$. This relationship suggests the term "virtual source" to be used for an area in which $\dot{\bar{Q}}^V$ is negative.

In the following sections, $\dot{\bar{Q}}^*$ is computed for mixing ratio, potential temperature, and equivalent-potential temperature. In addition, virtual sources and sinks of θ_e are examined.

b. mixing ratio

Three versions of $\dot{\bar{q}}^*$ have been computed. Version A uses all updraft soundings for evaluating means of u, v, ω, and q. The second distribution (version B) uses the limited updraft counterparts of the means used for version A. Another possibility, version C, is formulated by using everything in version B except for ω, which is instead composed of version C of the vertical-motion field.

Figure 15b shows version C of the $\bar{q}^*$ field. The apparent source of q in the downdraft area is much smaller than in the corresponding area in Fig. 15a, because of the decreased intensity of the downdraft in version C. The rate of condensation is slightly decreased from that found in the other two versions. The configuration of apparent sources and sinks of q is generally similar among the three versions, with some differences in the intensities of the apparent sources and sinks. In the computation of $\bar{q}^*$ and other quantities to follow, it is found that the first two terms on the right of (8a) are about an order of magnitude smaller than each of the remaining terms.

The bottom portion of Fig. 15a is a rainfall-rate curve obtained from rain-gauge data at the 44 surface stations. It appears that the peak of the condensation due to the mean motion occurs about 15 minutes before the rainfall-rate peak occurs. This allows time for rain droplets to grow by condensation, collision, and coalescence, and to fall to the ground.

c. potential temperature

The results of the computation of $\bar{\theta}^*$ are shown in Fig. 16. Again, three versions have been calculated, similar to those for $\bar{q}^*$. For versions A and B, the rate of cooling in the downdraft region is as high as 0.5 deg C per minute. Similar rates of warming are found in the updraft region.

These rates of warming and cooling are very large, but they are in effect for a limited period of time. Reference to Fig. 8a will show that the speed of an air parcel relative to the moving front is, on the average, at least 10 m sec^{-1} above the frontal surface. Since

the distance in the y-direction considered by this study is limited to 80 km, an air parcel entering the vertical cross section on the right side will traverse the entire distance in slightly over two hours. The net change of the properties of the air parcel is generally small, but large changes do occur within the cross section.

In Fig. 16b, the effects of a weak downdraft and an updraft that is slightly weaker than that used in Fig. 16a are evident. The apparent sink is very weak and the apparent source has a lower maximum value compared to the same features in Fig. 16a. In addition, the center of the apparent source in Fig. 16b is displaced to the left of the one in Fig. 16a, since the updraft maximum is similarly displaced.

d. equivalent-potential temperature

Figures 17a and 17b display the distribution of $\overline{\theta}_e^*$ in a manner like that of the two previous figures. The values of $\overline{\theta}_e^*$ are computed in a manner different from that used for $\overline{\theta}^*$ and $\overline{q}^*$, however. First of all, the approximation

$$\theta_e = \theta \exp\left(\frac{Lq}{C_p T}\right) \approx \theta\left(1 + \frac{Lq}{C_p T}\right) \approx \theta + \frac{Lq\theta}{C_p T} \qquad (9)$$

is made. Then, an approximate $\overline{\theta}_e^*$ is calculated using

$$\overline{\theta}_e^* = \overline{\theta}^* + \frac{L}{C_p}\overline{q}^* \qquad (10)$$

This approximate value is adjusted by calculating the version A distribution of $\frac{\partial}{\partial y}(\bar{v}\,\bar{\theta}_e) + \frac{\partial}{\partial p}(\bar{\omega}\,\bar{\theta}_e)$ and comparing this quantity to $\frac{\partial}{\partial y}(\bar{v}\,\bar{\theta}) + \frac{\partial}{\partial p}(\bar{\omega}\,\bar{\theta}) + \frac{L}{C_p}\left[\frac{\partial}{\partial y}(\bar{v}\,\bar{q}) + \frac{\partial}{\partial p}(\bar{\omega}\,\bar{q})\right]$. The typical difference involved is rather small, about 0.01 deg C min^{-1}, which

is about one tenth of $\overline{\dot{\theta}_e^*}$. This difference is used to correct the values derived from (10). The method used here ignores time-consuming corrections for $\frac{\partial \theta_e}{\partial t}$ and $\frac{\partial}{\partial x}(\bar{u}\bar{\theta}_e)$. In addition, the same corrections are assumed to be valid for version B.

Noteworthy features in Fig. 17a include an apparent sink in the upper right corner, below which a pronounced apparent source is evident. Behind the SWS line, the apparent sink region is confined to the lower troposphere in the region of ascent.

In Fig. 17b, the intensity of the apparent sink in the upper right corner is minimal compared to that in versions A and B, due to the difference in downdraft magnitudes. Another area of disagreement is located near +100 min at about 500 mb, where a moderately intense apparent source is present in Fig. 17b, with lesser apparent sources at the same place in Fig. 17a. In general, the gross character of $\overline{\dot{\theta}_e^*}$ does not differ much between versions A and B, but these two versions differ somewhat from version C.

Changes in the value of θ_e of an air parcel can occur due to conduction, radiation, and friction at the boundaries, and also by melting and freezing within the parcel. The latent heat of fusion can produce heating at high levels where freezing occurs and cooling at somewhat lower levels where there is melting. This pattern of heating and cooling does seem to coincide qualitatively with the pattern of $\overline{\dot{\theta}_e^*}$ between +40 min and +100 min, so the latent heat of fusion might be responsible for part of the $\overline{\dot{\theta}_e^*}$ behavior. Except for melting and freezing, and the effects of unresolvable eddies of scales smaller than the cumulus cloud scale, the rate of change of

equivalent-potential temperature following the total motion should be zero when virtual sources and sinks are taken into account. Radiation effects, which amount to only about one or two degrees per day, can be ignored here.

Primed quantities, used in calculating the distribution of virtual sources and sinks, are derived from the groups of about ten balloon measurements which are averaged together and attributed to centroid positions for purposes of analysis. One problem that arises from this procedure involves the values of ω, which must be calculated from individual balloon ascent rates, instead of from the kinematically-determined vertical motions. The fields of $\bar{\omega}$ for these two versions do not match, as an inspection of Fig. 9a will surely show. Fortunately, this difficulty can be overcome by the following analysis.

Let σ denote the fraction of the total area under consideration that is occupied by cloud updrafts. Suppose that cloud and environmental values of any two quantities, A and B, are known. Then,

$$\overline{A'B'} = \sigma(A_c - \bar{A})(B_c - \bar{B}) + (1 - \sigma)(A_e - \bar{A})(B_e - \bar{B}) \quad , (11)$$

and $\bar{A}$ (or $\bar{B}$) can be expressed as

$$\bar{A} = \sigma A_c + (1 - \sigma) A_e \quad , (12)$$

so that it is possible to express $\overline{A'B'}$ by

$$\overline{A'B'} = \sigma(1 - \sigma)(A_c - A_e)(B_c - B_e) \quad , (13)$$

where subscripts c and e refer to cloud and environmental values, respectively. For fixed values of A_c, A_e, B_c, and B_e, it is possible to maximize $\overline{A'B'}$ by choosing σ to be 0.5, a rather high value in the real atmosphere. The "observed" values of $\overline{\omega' \theta_e'}$ are computed by using information from individual rawinsondes, instead of from the explicit use of (13). However (13) can be used to point out the

dependence of $\overline{\omega'\theta_e'}$ upon the value of σ. The values of $\overline{\omega'\theta_e'}$ computed from version A can be changed to version B simply by altering σ, since the updraft coverage is the distinction between the two versions. The magnitude of $\overline{\omega'\theta_e'}$ is especially sensitive to the value of σ in the 0.0 to 0.3 range, which applies to most of the atmosphere. There is little dependence upon the value of σ in the 0.3 to 0.7 range.

The horizontal divergence of eddy fluxes of θ_e, which is small compared to the vertical divergence, is computed using data from groups of about ten balloons in order to define means and the deviations from the means in each group. The x-component of the flux divergence is assumed to be negligibly small. The y-component results are shown in Fig. 18. A rather large virtual sink is present at +10 min and 500 mb. Otherwise, the field lacks regions of pronounced virtual sources and sinks.

In Fig. 19, the $\overline{\omega'\theta_e'}$ correlations are shown. It is interesting to focus attention upon the downdraft region above the SWS, where the kinematically-determined vertical velocities and the net balloon ascent rates are in disagreement. On the left side of the downdraft area (+20 min), there is indeed a large negative correlation between ω and θ_e. The center of the downdraft (+10 min) is in a region where there is a large gradient in the correlation field, and there is virtually no correlation earlier than -10 min at upper levels. A negative correlation between ω and θ_e implies that higher than average values of vertical velocity occur in warm cloud areas, and that downdrafts can be associated with cold regions. A high negative correlation indicates the amount of convection, which creates a potential for balloons to be entrained into cloud updrafts.

In Fig. 20, the distribution of $\frac{\partial}{\partial p}(\overline{\omega'\theta_e'})$ is shown. A comparison with Fig. 18 shows that $\bar{\dot{\theta}}_e^v$ is approximately represented by the term $\frac{\partial}{\partial p}(\overline{\omega'\theta_e'})$. It is possible to evaluate $\bar{\dot{\theta}}_e$ by adding the divergences of mean and eddy fluxes, $\bar{\dot{\theta}}_e^*$ and $\bar{\dot{\theta}}_e^v$. This is done here by comparing the patterns of Figs. 17 and 20, since the horizontal eddy flux divergences can be safely ignored, for the most part. There is generally good agreement between the apparent sink in Fig. 17a and the virtual sink in Fig. 20. A little shifting of patterns brings about a general cancellation between the virtual source in the upper right corner of Fig. 20 and the apparent source in the same vicinity in Fig. 17a. The apparent sink in the upper right corner of Fig. 17a has no counterpart in Fig. 20, although the virtual sink in Fig. 18, which represents $\frac{\partial}{\partial y}(\overline{v'\theta_e'})$, would partially compensate if it were shifted slightly to the right. Where the streamlines closely parallel the isopleths of θ_e in Fig. 11b, $\bar{\dot{\theta}}_e$ turns out to be nearly zero.

6. Model simulation of convection

A slightly modified version of the one-dimensional, steady-state, entraining cloud model of Squires and Turner (1962) is used to examine the behavior of model cumulus clouds associated with the 14 May 1970 cold front. Calculations of model clouds are carried out at intervals of 10 min along the time axis (or 4 km along the y-axis). Cloud-top heights computed by the model are compared to radar-derived heights, where available.

The version of the cloud model used in this study was developed by Phillips (1973). It uses four basic variables: mass flux, vertical velocity, concentration of water (in all three phases), and entropy. Squires and Turner used virtual temperature instead of entropy. The model assumptions include the following:

1) The updraft is in a steady state, is axisymmetric, and is vertical.
2) The environment is thermodynamically homogeneous and hydrostatic at each level.
3) There is no horizontal pressure gradient between the cloud and its environment.
4) Except for radial velocity, all variables have top-hat profiles.
5) The radius of the cloud is allowed to vary with height, and there is no rotational velocity component.
6) The proportion of ice to total condensed water varies linearly from 0 at -15 deg C to 1 at -40 deg C.
7) Condensate resides at the same level where it is formed.

In reality, updrafts are usually tilted somewhat, as they are in this case according to the evidence accumulated so far. Also, precipitation does fall out of clouds, although probably not back through the lower levels of the updraft. In spite of these omissions, the model's results can be used to formulate first-order approximations of cloud-top heights and vertical motions.

The cloud radius and updraft speed at the cloud base level are arbitrary. Four sets of base conditions are used in this study. Past experience has shown that combinations that compare well with observations are 1 and 2 m sec^{-1} for vertical motions and 1 and 2 km for base radius.

Figure 21 shows cloud-top heights computed by the model with four sets of base conditions. The model's cloud-top level is defined to be the level at which the vertical velocity becomes zero. The radar RHI display at 1940 CST is also shown in the figure for comparison with the model's results. The relative positions of the updrafts represented by the model and the falling rain corresponding to the radar echoes demonstrate the tendency of the updrafts to form well ahead of the heavy rainfalls at the ground, as expected.

In general, the maximum cloud-top heights computed by the model compare favorably with those derived from radar observations. It is also true that model updraft velocities agree well with the net balloon ascent rates of updraft soundings. Ahead of the SWS line, modest base conditions (i.e., a 1 m sec^{-1} base updraft and a 1 km base radius) seem appropriate, since mesoscale vertical motions are slight. Where the convection reaches its peak, the combination of a 2 m sec^{-1} base updraft and a 2 km base radius gives good results.

It is evident from Fig. 21 that the thermodynamic potential of the environment to "grow" clouds with constant base conditions does not change much from -40 min to +50 min. However, the existence of clouds as tall as those computed by the model ahead of the SWS line cannot definitely be confirmed by direct ground-based observations, and there are very few radar echoes in that region. It is possible that towering cumulus clouds did exist just in front of the SWS line, and that they were obscured by a low-level stratus layer. Rapid evaporation of such clouds, if they existed, would account for the high evaporation in that region (see Fig. 13), and also for the fact that few radar echoes existed there.

The area in front of the SWS line is more potentially unstable than the area in the vicinity of the convective line ($\frac{\partial \theta_e}{\partial z}$ is more negative). However, the pre-frontal environment is drier at upper levels. The fact that the clouds actually grew to great heights at post-frontal times is probably due to more favorable base conditions (a larger cloud radius and a bigger updraft).

7. Conclusions

The use of data from a dense rawinsonde network, an array of surface stations, and radar has made it possible to present a detailed analysis of a cold front in two dimensions. The data compositing using the assumptions of a steady state and of negligible variations along the frontal axis has increased the resolution of the system to the extent that the effects of convective elements can be taken into account. Non-steady-state effects and derivatives in the x-direction have been evaluated where thought to be important.

It is quite possible that cumulus activity was responsible for the cooling and moistening of the air in the downdraft above the SWS line. The lack of radar echoes indicates that any clouds in the area were evaporating before they could reach the precipitating stage. Although the cloud model grows tall clouds for a large distance in the y-direction without much variation, radar observations show a large difference between cloud activity above the SWS line and 20 to 40 km behind the line. This observation suggests that clouds near the observed convective line had a larger horizontal extent and/or vertical velocity than those above the SWS line, accounting for differences in the vertical mass flux and the effects of evaporation.

The mesoscale updraft pictured in Fig. 9 appears to be triggered by frontal lift at low levels and sustained by latent heat release at higher levels. The large amount of condensation shown in Fig. 13b in the uplift region suggests the role of latent heat release. Evaporation and cooling seem to be responsible for the descent region above the SWS line, except for a region in the upper right corner of the y-p plane. It is in this same corner that an apparent sink of θ_e

occurs, with no corresponding virtual sink. Therefore, the strong downdraft in the upper right corner is suspect.

The size of the apparent sources and sinks of θ_e indicates that the mean mesoscale flow does not conserve θ_e. This result is probably not due to poor data, since virtual sources and sinks qualitatively match the corresponding apparent features in most places.

An important question raised in this study concerns the possible tendency of balloons to drift into updrafts and out of downdrafts. In future studies involving a mesoscale rawinsonde network in a convective area, this sampling bias must be taken into account.

Accurate values of two important quantities remain hard to obtain even with the density of the data available for this study: vertical motion and the areal coverage of cumulus clouds. These two variables must be known accurately in order to measure vertical eddy transports. Doppler radar data, which has become available in the NSSL network since 14 May 1970, can be used to measure vertical velocities as well as horizontal winds with good resolution. Raindrops are used as scatterers in precipitation areas, while metallic chaff is released into the surrounding environment. The extent and location of cumulus clouds can be observed by aircraft as well as by satellites with high resolution photography equipment.

A coordinated effort of all of the above mentioned observational schemes is needed to resolve motions down to the cumulus scale so that cloud-environment interactions can be more fully understood. For a three-dimensional representation that can resolve convective activity, a network somewhat denser than the one used here is needed.

ACKNOWLEDGEMENTS

I am grateful to professor Frederick Sanders for introducing me to the 14 May 1970 case and for his guidance and helpful suggestions throughout the course of this study. Thanks is due to David I. Katz, who pursued some special problems, such as the net balloon ascent rate determination and the non-steady-state effects in the calculation of the vertical motions. I appreciate the work of David Katz and Robert Norton during the early stages when the data was being reduced to a workable form, and I thank Isabelle Kole for drafting the figures. Finally, I wish to acknowledge the groundwork laid by Jack Meneely in his study of this case, and to thank the NSSL staff for providing the necessary data.

APPENDIX A

Desirable statistical qualities of an estimator of a population mean include accuracy (it is unbiased), efficiency (it has a small variance about the true mean), and consistency (its variance gets smaller as the number of observations is increased). In the following discussion, based upon Wonnacott and Wonnacott (1972), it is assumed that the populations being considered are not necessarily normally distributed. The Central Limit Theorem cannot be applied with total confidence to samples consisting of only ten observations, as in this study. Therefore, the samples may not be normally distributed.

Two possible estimators of the population mean that are derived from samples are the mean and the median of the sample. Unfortunately, the sample mean can be adversely affected by a single wildly deviant observation, which can pull the estimate of the population mean considerably off target. Although the median is relatively unaffected by one wild observation, it uses only one observation for its estimate of the population mean. A compromise choice uses some, but not all, of the observations, and it is called the Best Easy Systematic (BES) estimator. It is calculated by arranging the observations in numerical order, trimming off a quarter of the values from each end, and then averaging just the two end and the two middle values of those remaining. The explicit formulas are

$$BES = 1/4 \left[x_{(\frac{n}{4})^+} + x_{(\frac{n}{2})} + x_{(\frac{n}{2}+1)} + x_{(\frac{3n}{4}+1)^-} \right] \qquad (A1)$$

for even n (the sample size), and

$$BES = 1/4 \left[x_{(\frac{n}{4})^+} + x_{(\frac{n+1}{2})} + x_{(\frac{n+1}{2})} + x_{(\frac{3n}{4}+1)^-} \right] \qquad (A2)$$

for odd n. In the formulas, each addend's subscript is an integer indicating rank, and the signs following the subscripts indicate the direction of rounding, if necessary. The efficiency of the BES estimator has been shown to be about 80% as good as that of the very best estimator available, assuming that the shape of the population were known. In other words, if the population were normally distributed, then the arithmetic mean (the best possible estimator) of a large sample would have a slightly smaller dispersion about the true mean than would the BES estimator. Both are unbiased, so that their values are centered about the true mean. However, if the population distribution is not known, or if the sample is not large, then the BES estimator is the best one to use. In this study, its most attractive asset is the ability to deal with extreme measurements without explicitly including or excluding them.

APPENDIX B

In a steady-state ascent of a spherical balloon, the drag (D) and free lift (L) in mass units can be related by

$$D = L\,g \quad , \tag{B1}$$

where D can be written as

$$D = \frac{\rho w^2}{2} \frac{\pi d^2}{4} C_d \quad . \tag{B2}$$

In (B2), ρ is air density, w is vertical velocity, d is sphere diameter, and C_d is the drag coefficient. Dimensional analysis shows (British Air Ministry Meteorological Office, 1961) that

$$C_d = C\,Re^n \quad , \tag{B3}$$

where

$$Re = \frac{w \rho d}{\mu} \tag{B4}$$

is Reynold's number, μ is the coefficient of viscosity, and C and n are dimensionless numbers to be found by experiment.

It is enlightening to examine the role of the Reynold's number in determining the behavior of the drag upon the balloon. This number is the ratio of fluid inertial forces to viscous forces. At low Re values, viscous forces in the boundary layer near the surface of a sphere dominate over the externally-driven inertial forces, and smooth flow results. As Re increases, the viscous forces become less able to damp inertial oscillations in the boundary layer. At a critical value of Re, the laminar flow that exists at low Re values gives way to turbulent flow as the oscillations break down into eddies. At this and higher values of Re, the air in the boundary layer can no longer negotiate the curvature of the sphere that it is flowing around, and turbulent separation occurs with an accompanying wake downwind.

The following discussion of the variation of drag with Reynold's number is based upon a paper by MacCready and Jex (1964). Figure 22 shows the effects of the Reynold's number upon sphere flow patterns, including locations of separation and wake configurations. At low Reynold's numbers (between 10^3 and 10^4), the separation occurs on the front part of the sphere, but the wake is closed and stable. The subcritical regime of Re values, between 10^4 and 2×10^5, features a thinner boundary layer with a rather unsteady wake that trails off in an oscillating pattern. The drag coefficient is high and fairly constant as a function of Re. In the critical regime of Re values (between 2×10^5 and 4×10^5), the separation becomes turbulent. The location of the separation of flow is at the back of the sphere while the boundary layer remains attached nearly all of the way around the sphere. The reduced size and greater stability of the resulting wake causes a sharp drop in the drag coefficient as Re is increased throughout the critical region. For Re values from 4×10^5 to 10^8 (the supercritical regime), the place of flow separation moves slightly toward the front of the sphere. The drag coefficient is increased somewhat over the critical regime values due to a larger separated region and to the increased frictional drag of the turbulent boundary layer upon external flow.

Another influence upon the flow pattern around a balloon is sphere roughness. Although the balloons used in rawinsonde ascents are smooth, it has been found that fine-grain turbulence has the same effect as sphere roughness upon the C_d versus Re relationship. No direct confirmation of turbulence aloft on the scale of a few cm is available for the 14 May 1970 storm, but the presence of numerous

convective cells along with possible gravity waves in the NSSL network at the time seems able to have created a situation that was conducive to small-scale eddies. The effect of the fine-grain turbulence (or roughness) is to cause the transition from laminar to turbulent flow to occur at lower values of Re than it otherwise would.

Yet another influence upon the drag is the tendency for a spherical balloon, which is lighter than air, to undergo significant lateral movement. A larger amount of fluid is affected than for the case of a heavy sphere, thus producing a larger drag.

All of the effects mentioned above create a complicated C_d versus Re relationship. A tentative curve derived for the case at hand from the results of MacCready and Jex is shown in Fig. 23.

It is necessary to estimate the range of Reynold's numbers that applies to the ascending rawinsonde balloon, so that the variation of drag with height can be determined from Fig. 23. It will be shown below that the knowledge of C and n, referred to in (83), is sufficient to determine the variations of balloon ascent rate with height.

At the ground, w is about 6 m sec^{-1} and d is about 2 m, so Re can be determined at ground level since ρ and μ are also known. The resulting value of Re is about 7.5×10^5. The change of Re with height is mostly a function of the air density, so there is a monotonic decrease in Re with height. At 400 mb, w is approximately 7 m sec^{-1}, a value taken from experiments (mentioned below), d is still about 2 m ~~sec^{-1}~~, and the values of ρ and μ are known. These numbers produce an Re value of about 4.1×10^5. From Fig. 23, it can be determined that the values of C and n that apply for the Reynold's

numbers between 4.1×10^5 and 7.5×10^5 are 1.15×10^{-3} for C and 0.40 for n. This region of Re values describes a transition from supercritical values at the ground to the upper critical regime at 400 mb, resulting in a slight decrease in the drag with height. The determination of C and n does not depend greatly upon the exact upper and lower values of Re (especially the value at the ground, in this case), since the Re versus C_d curve does not fluctuate much for supercritical Re values. This is fortunate, since some estimate of w, which is the unknown quantity for which a solution is sought, is needed to establish the range of Re values that the balloon experiences.

The total lift of the balloon, L + M (free lift plus the mass of the load and the balloon), can be written as

$$L + M = \pi d^3 \rho (1 - r)/ 6 \quad , \qquad (85)$$

where r is the density ratio of helium to air at the same pressure and temperature.

Since L, M, d, ρ, C, n, and μ are measureable, w as a function of pressure can be found from (81) through (85). The result is

$$w = \frac{b \mu^{(1-2/m)} L^{(1/m)}}{\rho^{(2/3 - 1/m)} (L+M)^{1/3}} \quad , \qquad (86)$$

where

$$b = \frac{(8g)^{1/m} (1 - r)^{1/3}}{6^{1/3} \pi^{(1/m - 1/3)} C^{1/m}} \qquad (87)$$

and $m = n + 2$. If n is zero, then C_d remains constant as Re varies, so that (86) effectively becomes

$$w = w_o \left(\frac{\rho_o}{\rho}\right)^{1/6} \quad , \qquad (88)$$

where the subscript refers to ground values. For the case being

considered here, the relationship is

$$w = w_o \left(\frac{\rho_o}{\rho}\right)^{0.249} \quad , \qquad (89)$$

which provides for an increase in w from 6.0 m sec^{-1} at the ground to 7.1 m sec^{-1} at 400 mb. A comparison of this result with that of pre-frontal balloon measurements of w and with experimental values derived from the results presented by MacCready (1965) are shown in Fig. 24. The adopted curve of still-air ascent rates for this study is also shown. In actual practice, this curve is shifted to the right or left for w_o values that are different from 6.0 m sec^{-1}.

APPENDIX C

To arrive at an idealized notion of inward velocities due to entrainment of the environment into cumulus clouds, reference is made to Ogura (1963). A cylindrical coordinate system includes a model cloud and the surrounding environment within a few cloud radii.

In this treatment, pressure is used as the vertical coordinate. The equation of continuity in a cylindrical geometry with no rotational wind component is given by

$$\frac{1}{r}\frac{\partial}{\partial r}(r\,u) + \frac{\partial \omega}{\partial p} = 0 \quad , \qquad (C1)$$

where u is the radial velocity. In Ogura's model, as in the Squires-Turner cloud model results that are computed for this case, the variation of w at the cloud core with height between cloud base and the level of the updraft maximum can be expressed approximately by $\frac{\partial w_o}{\partial z} = A$, a constant, where the subscript refers to a variable at the cloud core. Assuming that time rates of change of p and w are essentially due to advections in the vertical, then ω is approximately $w\frac{\partial p}{\partial z}$ and dw is given by $\frac{\partial w}{\partial p}\,dp$. It follows that

$$\frac{\partial \omega}{\partial p} \approx \frac{\partial w}{\partial z} = A \quad . \qquad (C2)$$

After Ogura, a Gaussian distribution for ω in the radial direction is assumed:

$$\omega(r,p) = \omega(p)\ \exp\left[-\left(\frac{r}{a}\right)^2\right] \quad , \qquad (C3)$$

where a is the cloud radius, which is assumed to be constant as height varies. Equations (C1), (C2), and (C3) can be combined to yield

$$\frac{du}{dr} + \frac{u}{r} = -A\ \exp\left[-\left(\frac{r}{a}\right)^2\right] \quad , \qquad (C4)$$

with u(r = 0) equal to zero. The solution of this first order, linear, ordinary differential equation is

$$u = u_c \frac{a}{r}\left\{\exp\left[-\left(\frac{r}{a}\right)^2\right] - 1\right\} \quad , \qquad (C5)$$

where $u_o = Aa/2$. Note that in this particular case, u is not a function of height below the level of the updraft maximum.

As an example, consider a cloud having an updraft maximum of 15 m sec^{-1} at a height of 5 km above cloud base, so that A is 3.0×10^{-3} sec^{-1}. Such a cloud is similar to model clouds computed by the Squires-Turner one-dimensional cloud model for this case. Suppose further that the cloud radius does not vary much with height, so that a constant value may be adopted without too much error. For this example, cloud radii of 1, 2, and 3 km are used. The value of u_o is proportional to the value of a, the cloud radius.

It is now possible to calculate the inward velocity as a function of distance from the cloud core. The time that a balloon would take to reach the edge of a cloud (after which it would be considered to be located in an "updraft") can be computed as a function of initial distance from the center, r_o, by

$$\text{time} = \frac{1}{u_o a} \int_a^{r_o > a} \frac{r \, dr}{1 - \exp\left[-\left(\frac{r}{a}\right)^2\right]} \quad . \qquad (C6)$$

Figure 25a shows the inward velocities experienced by balloons as a function of radius, and Fig. 25b displays the time required by a balloon to reach the cloud's edge as a function of distance from the cloud's edge. As the radius of the cloud increases, the increase in u_o has the effect of decreasing the time required to reach the cloud's edge. A balloon rising through still air takes about 18

minutes to reach the 400-mb level, which is about 5 km above cloud base for this case, and slightly above the level of updraft maxima that were calculated by the Squires-Turner cloud model. As a general rule, the time of arrival of a balloon at the cloud's edge is inversely proportional at the cloud's radius for times less than 20 minutes. In order for a balloon to be identified as being in an updraft, it would probably have to reach the cloud's edge in 10 minutes or less. That limits the distance that the balloon could be away from the cloud's edge at the time of launch to about 0.5 km for a 1000 m cloud radius, 1.1 km for a 2000 m cloud radius, and 1.7 km for a 3000 m radius. Once the balloon rises above the level of the maximum updraft, it begins to encounter outward radial velocities unless it is at the cloud core.

This example is quite idealized, but it gives an idea of the general magnitude of inward velocities encountered by a balloon which may be near a symmetric, cylindrical, entraining cloud. The asymmetry of updrafts and downdrafts and large horizontal velocities observed in the vicinity of the convective line in the 14 May 1970 case are signs that perhaps larger inward velocities than those computed here may have existed.

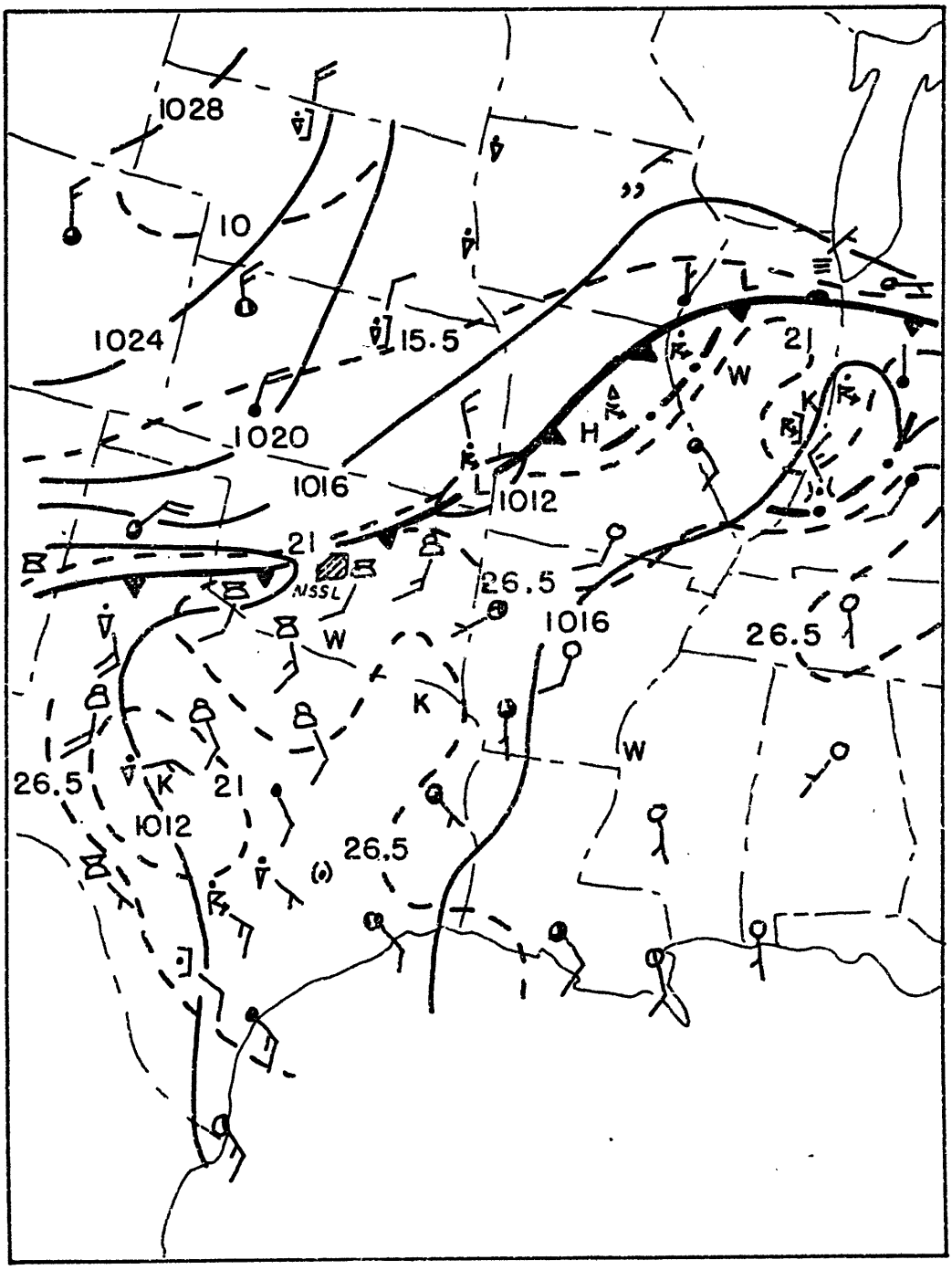

Fig. 1a. Surface analysis at 1800 CST, 14 May 1970

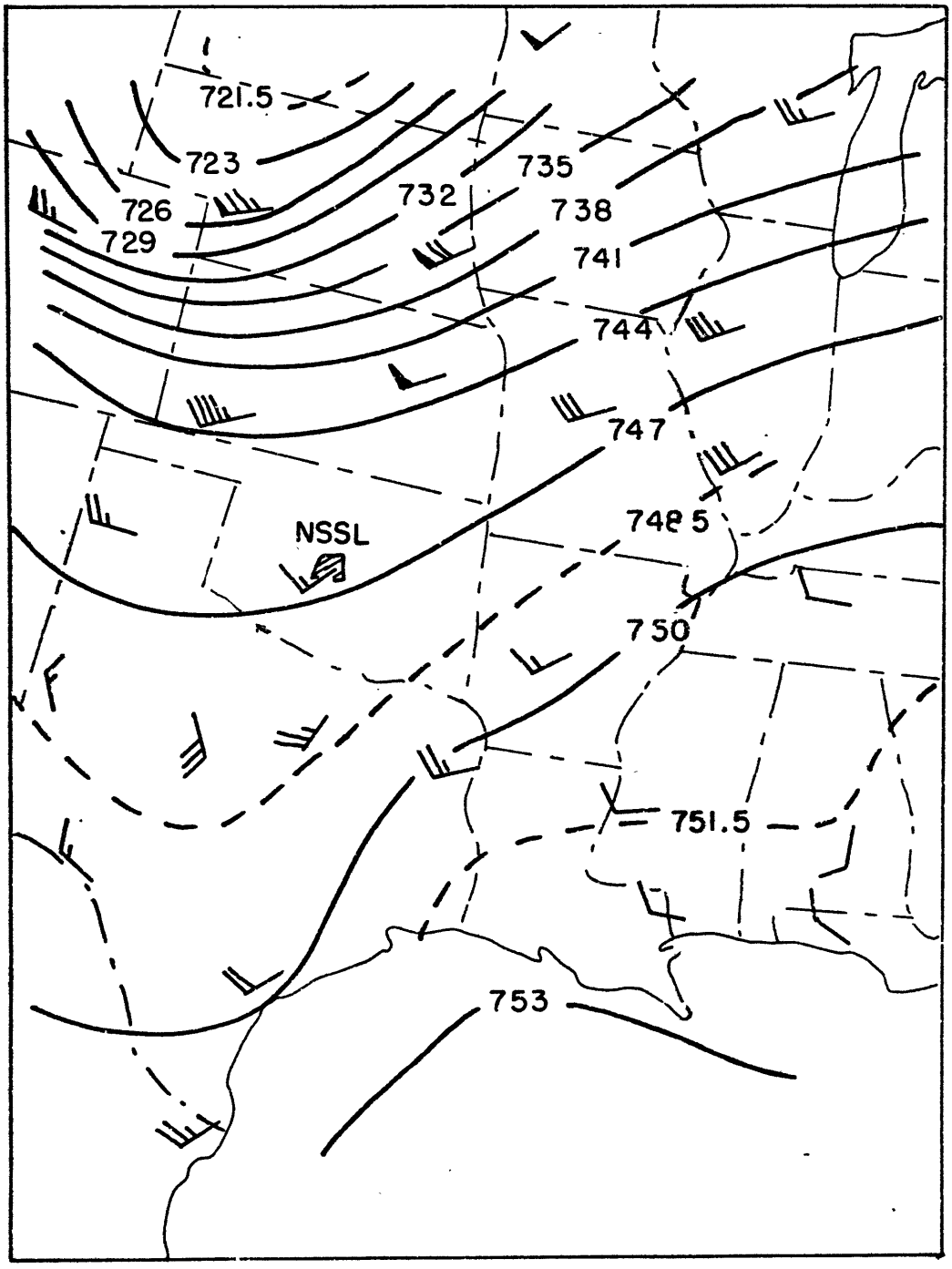

Fig. 1b. The 400-mb analysis at 1800 CST, 14 May 1970.

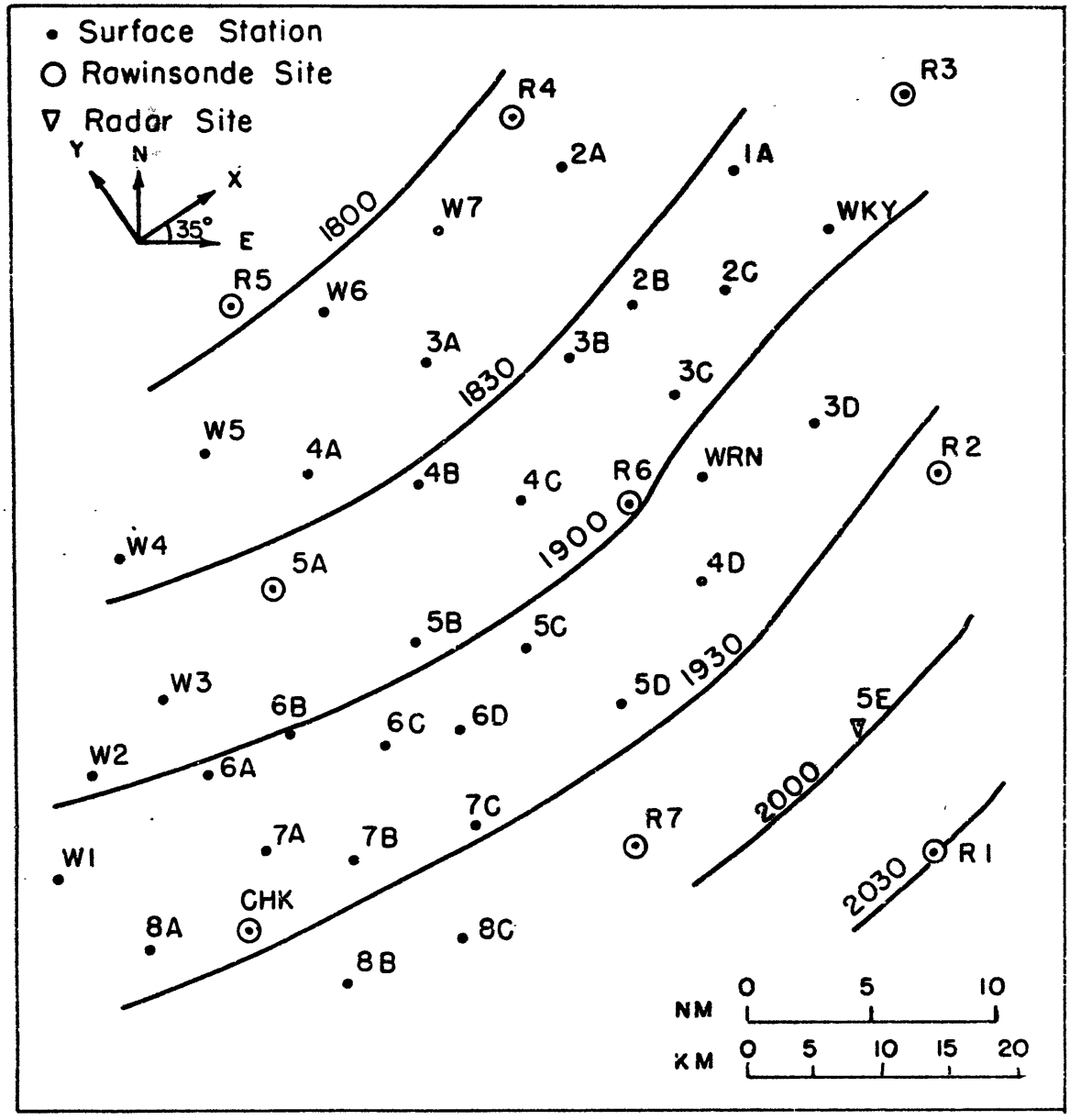

Fig. 2. The 1970 NSSL mesonetwork and isochrones of surface wind shift. The x and y axes are rotated so the x-axis is parallel to the mean isochrone configuration.

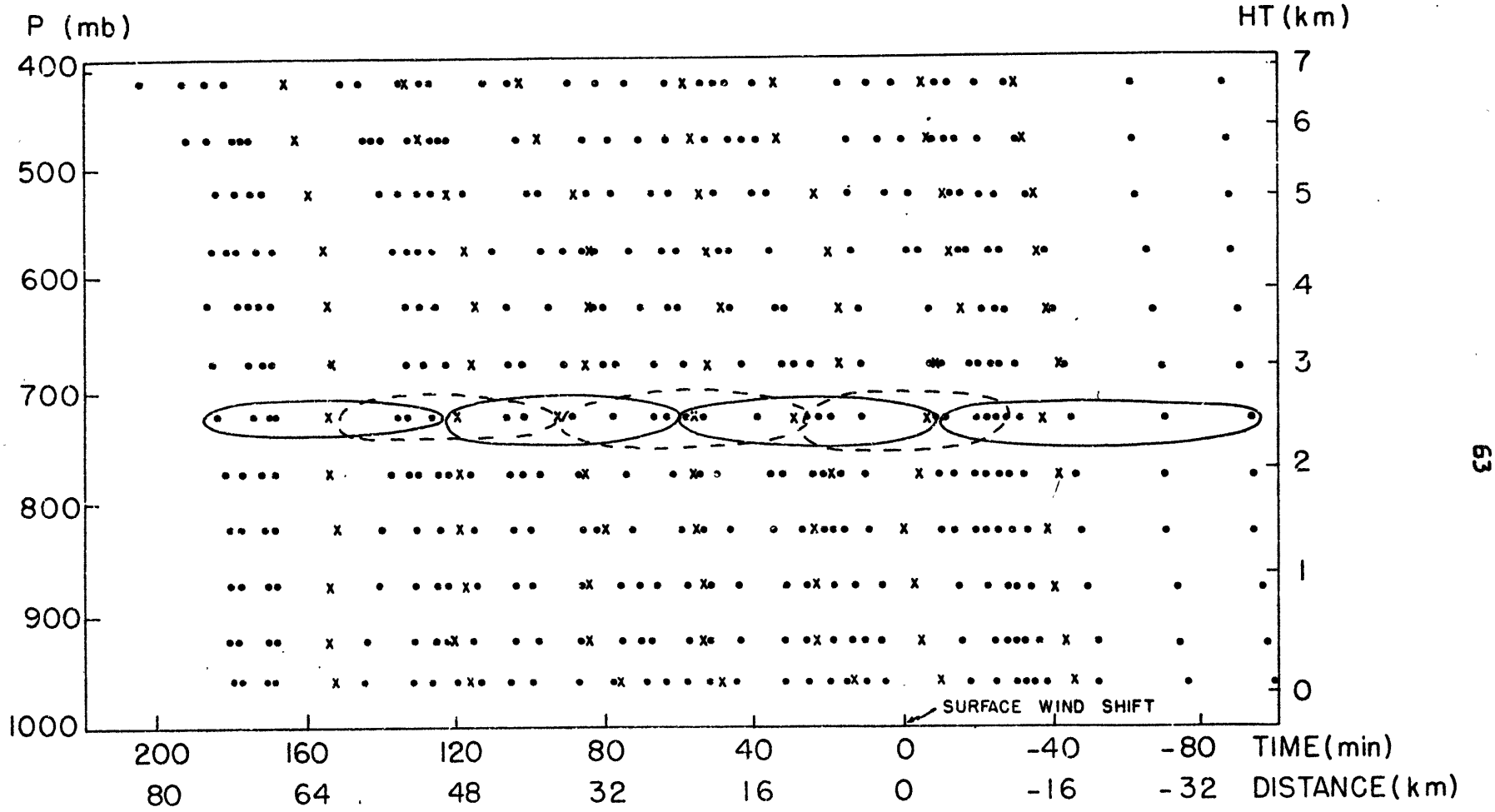

Fig. 3. A y-p cross section moving with the front, showing the positions of balloons at 50-mb intervals (dots). An example of the horizontal averaging scheme is shown at 725 mb. The X's locate the centroids of the averaged balloon groups.

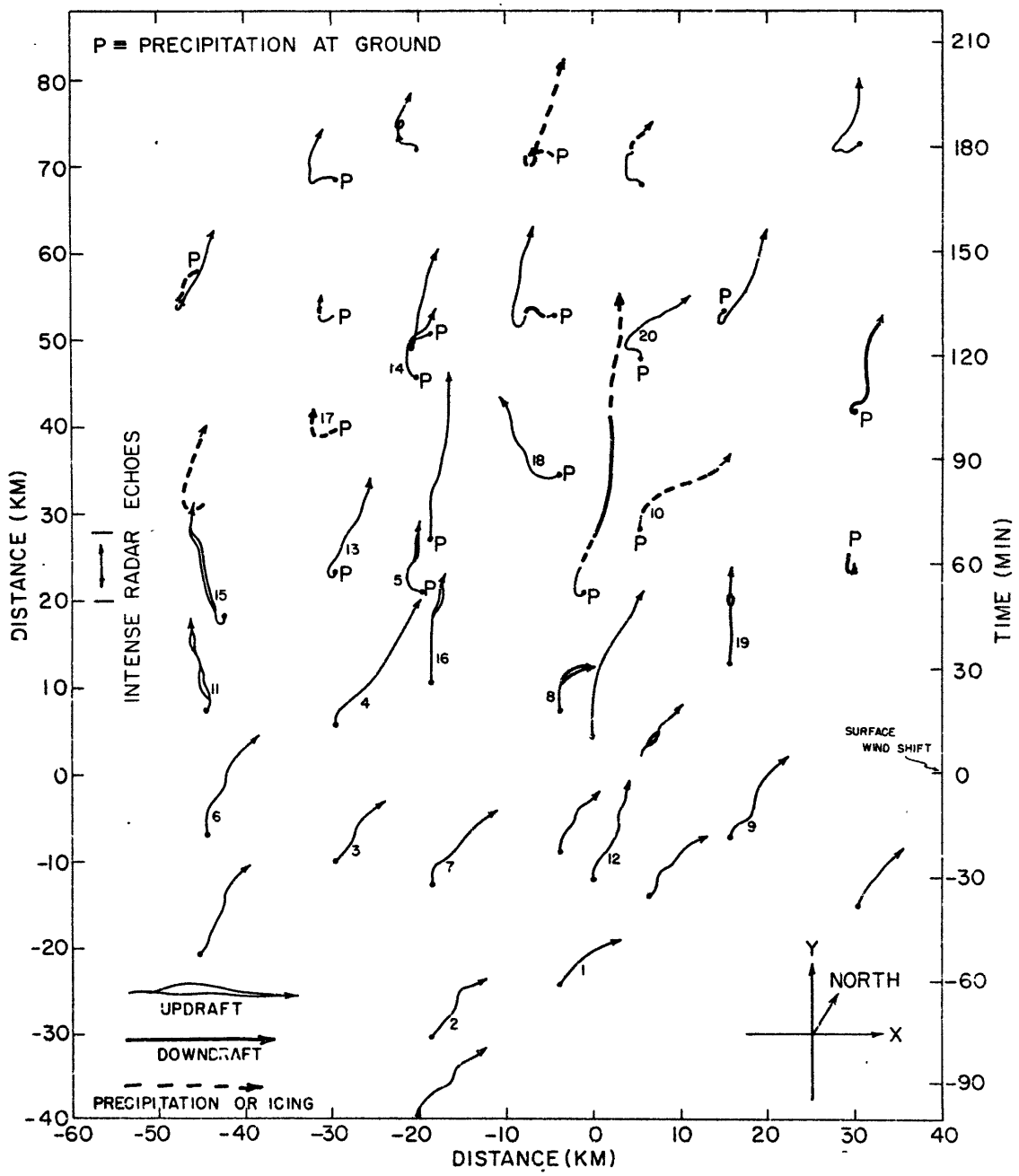

Fig. 4. An x-y map moving with the front, showing the horizontal movement of each balloon. Balloons that were caught in updrafts, downdrafts, or precipitation areas are identified. Numbers next to some balloons mark those that appear in Fig. 5.

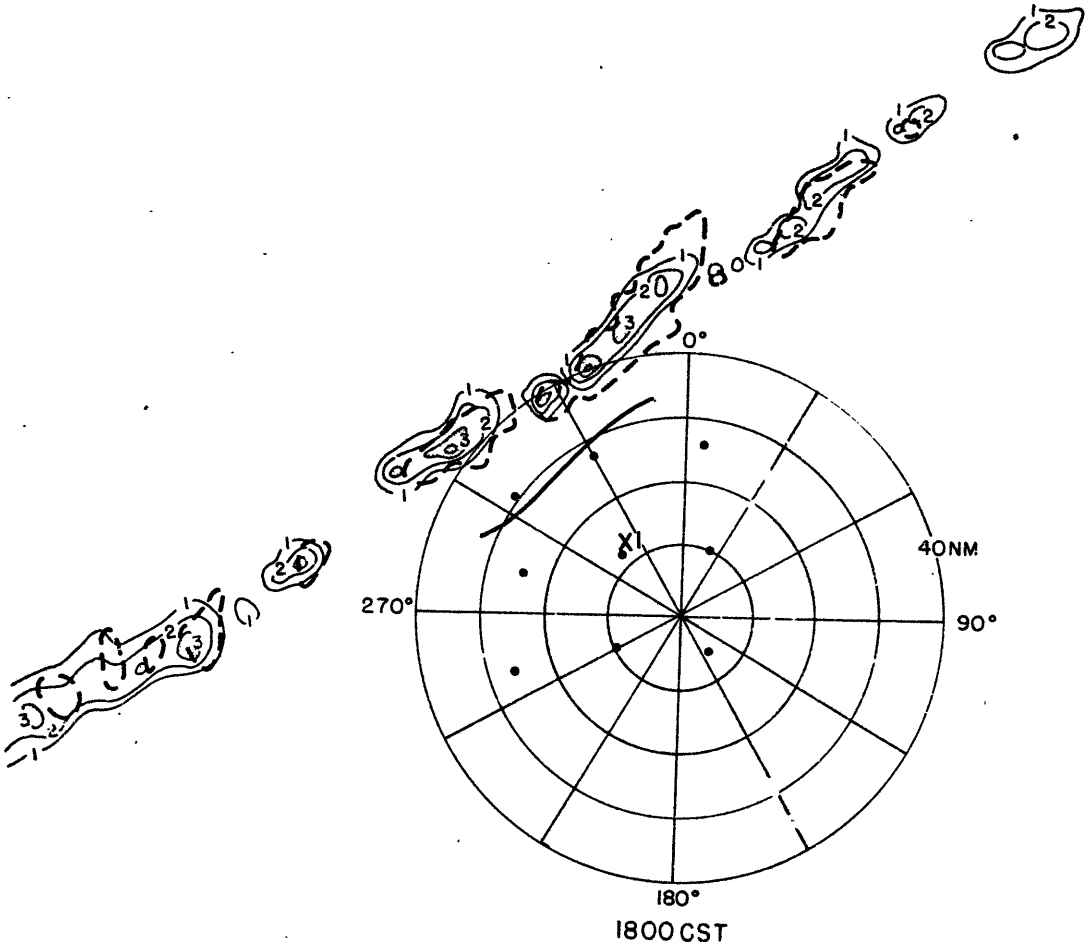

Fig. 5a. Radar PPI presentations at half-hour intervals in the vicinity of the NSSL network on 14 May 1970. Labelled thin solid lines represent values of log Z_e, the radar reflectivity factor, at 0° elevation. The dashed line is the log Z_e = 1 threshold contour at the anvil level (from 3° to 6° elevation). The heavy solid line shows the position of the SWS. Heavy dots indicate the locations of rawinsonde stations. The X's with a number next to each are the positions of balloons that were in the air at the time that the figure represents. See Fig. 4 to identify each balloon with areas of updrafts, downdrafts, and precipitation.

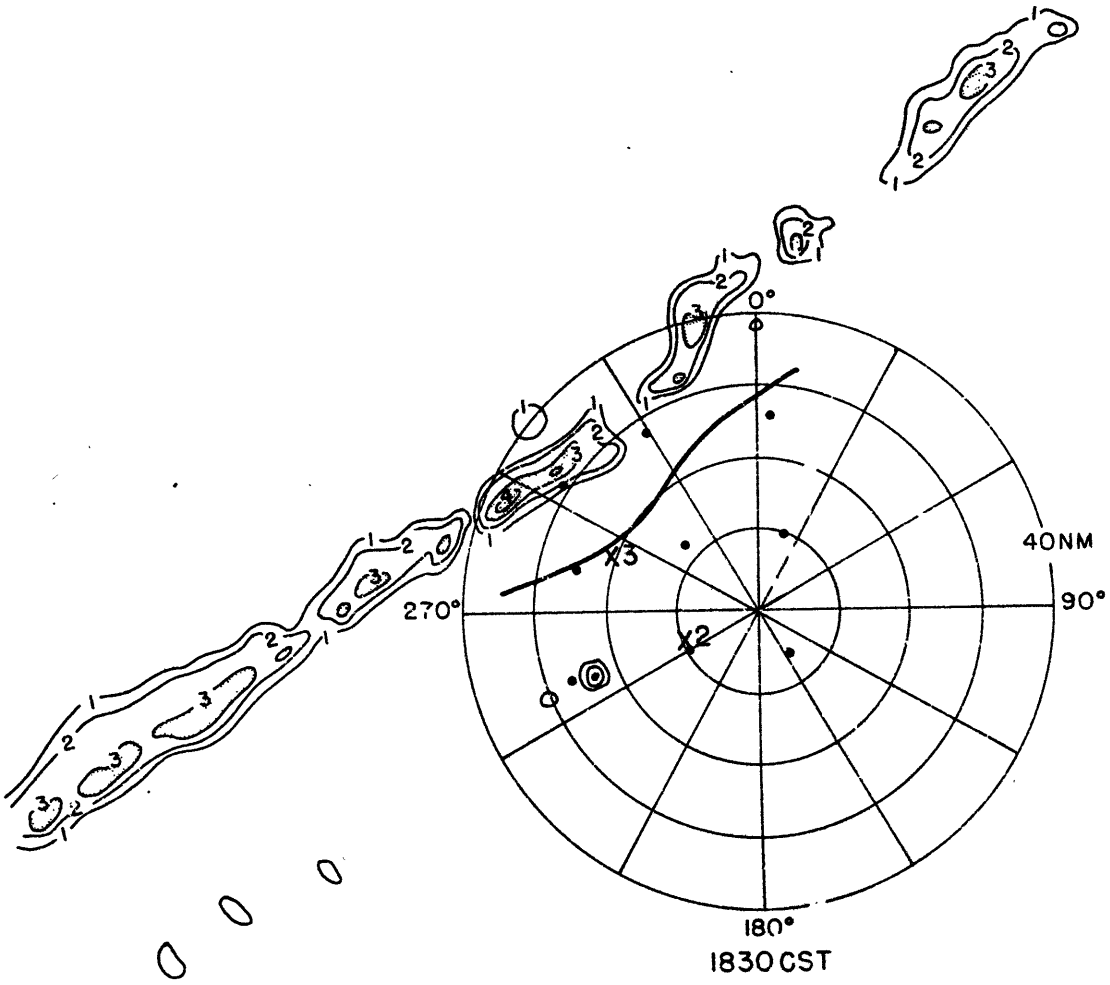

Fig. 5b. Same as Fig. 5a.

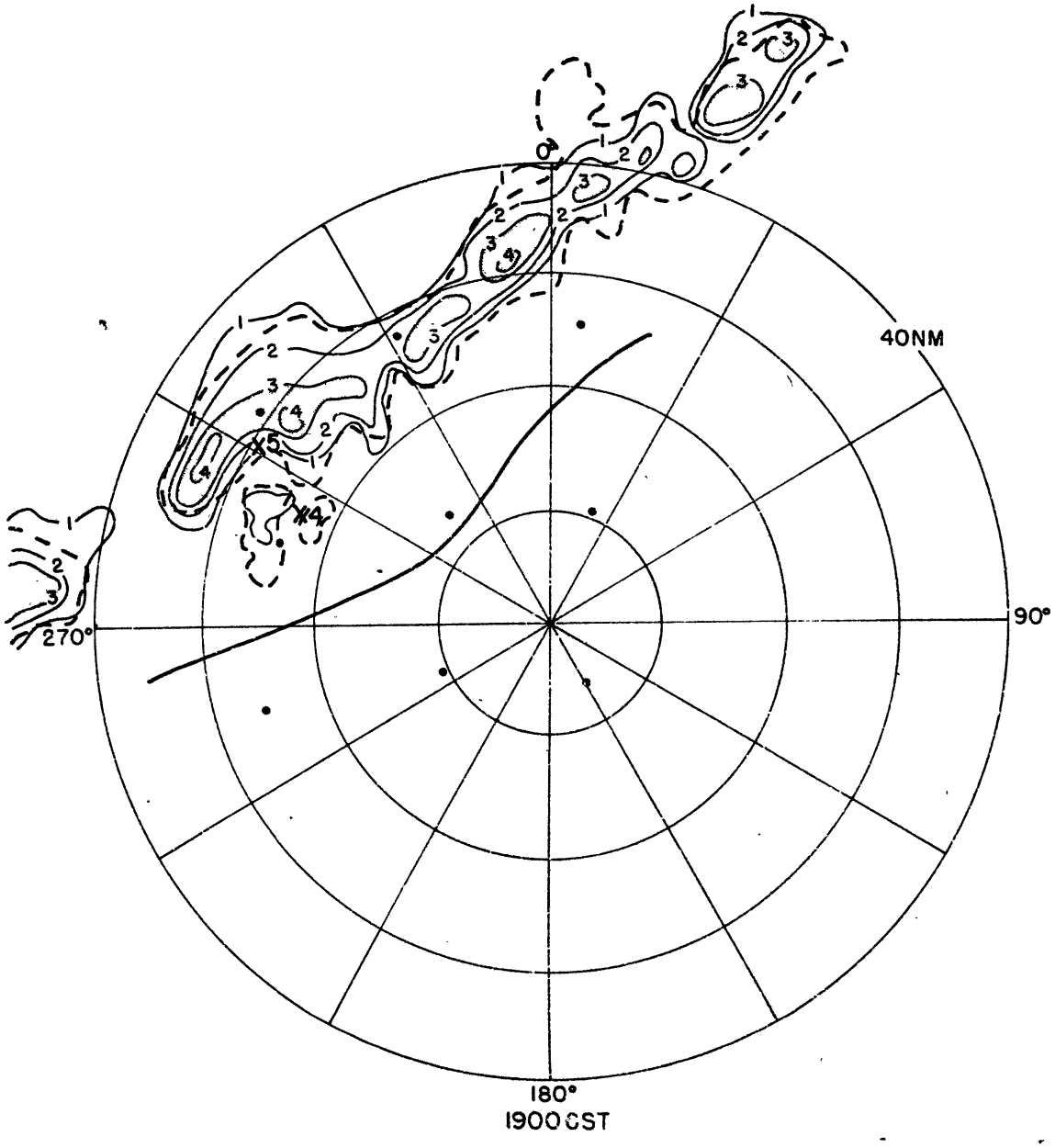

Fig. 5c. Same as Fig. 5a

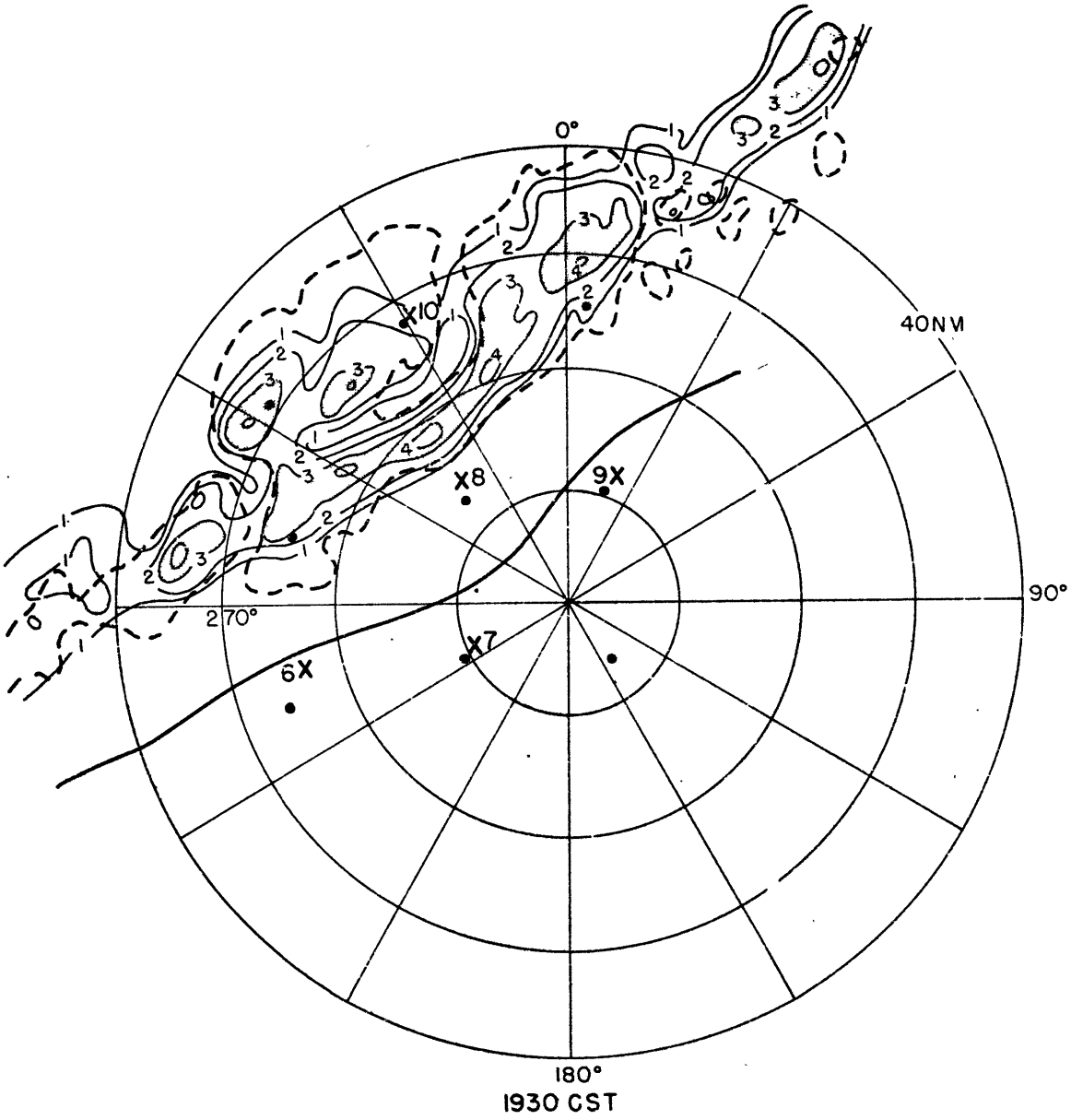

Fig. 5d. Same as Fig. 5a.

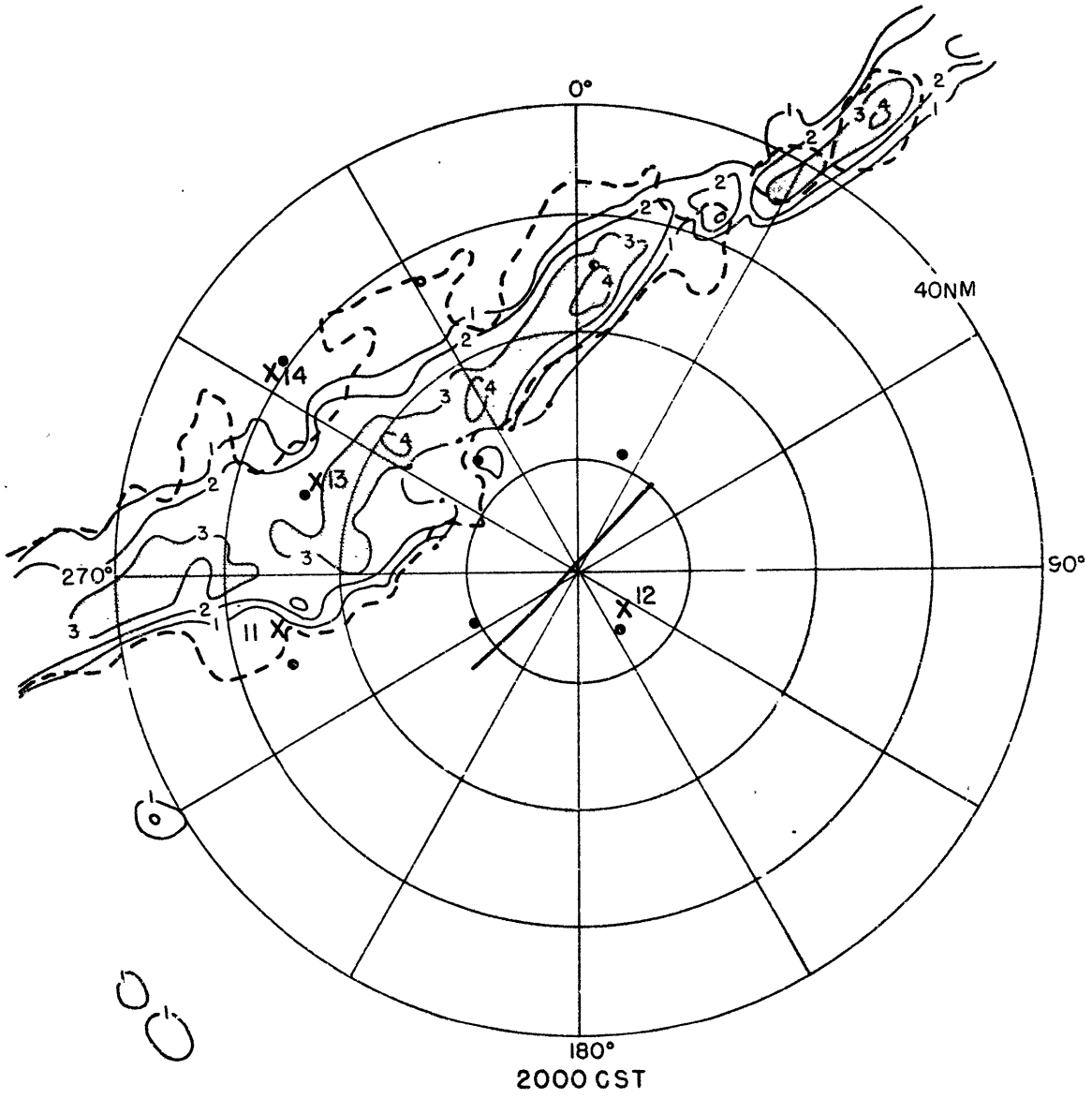

Fig. 5e. Same as Fig. 5a.

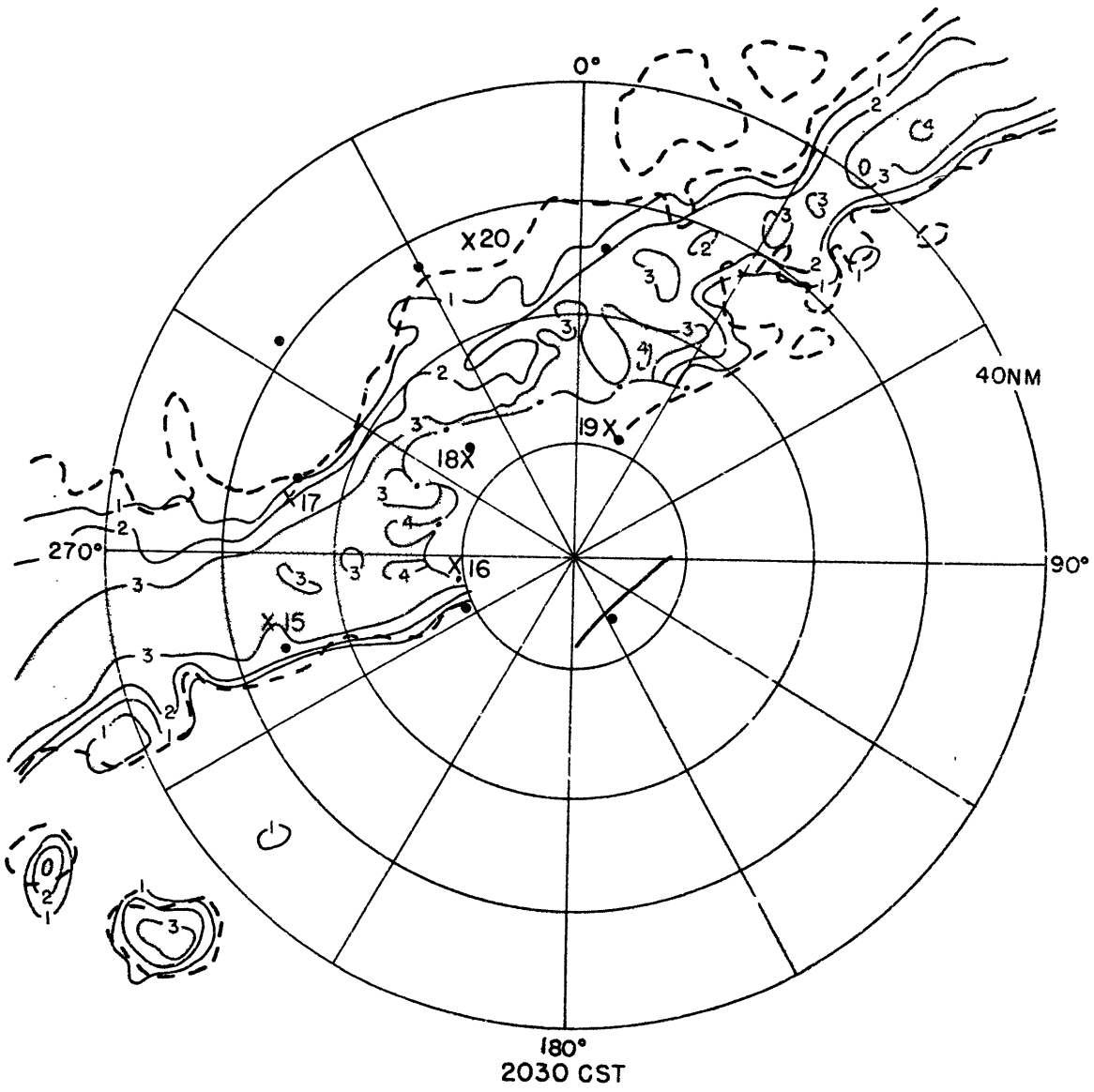

Fig. 5f. Same as Fig. 5a.

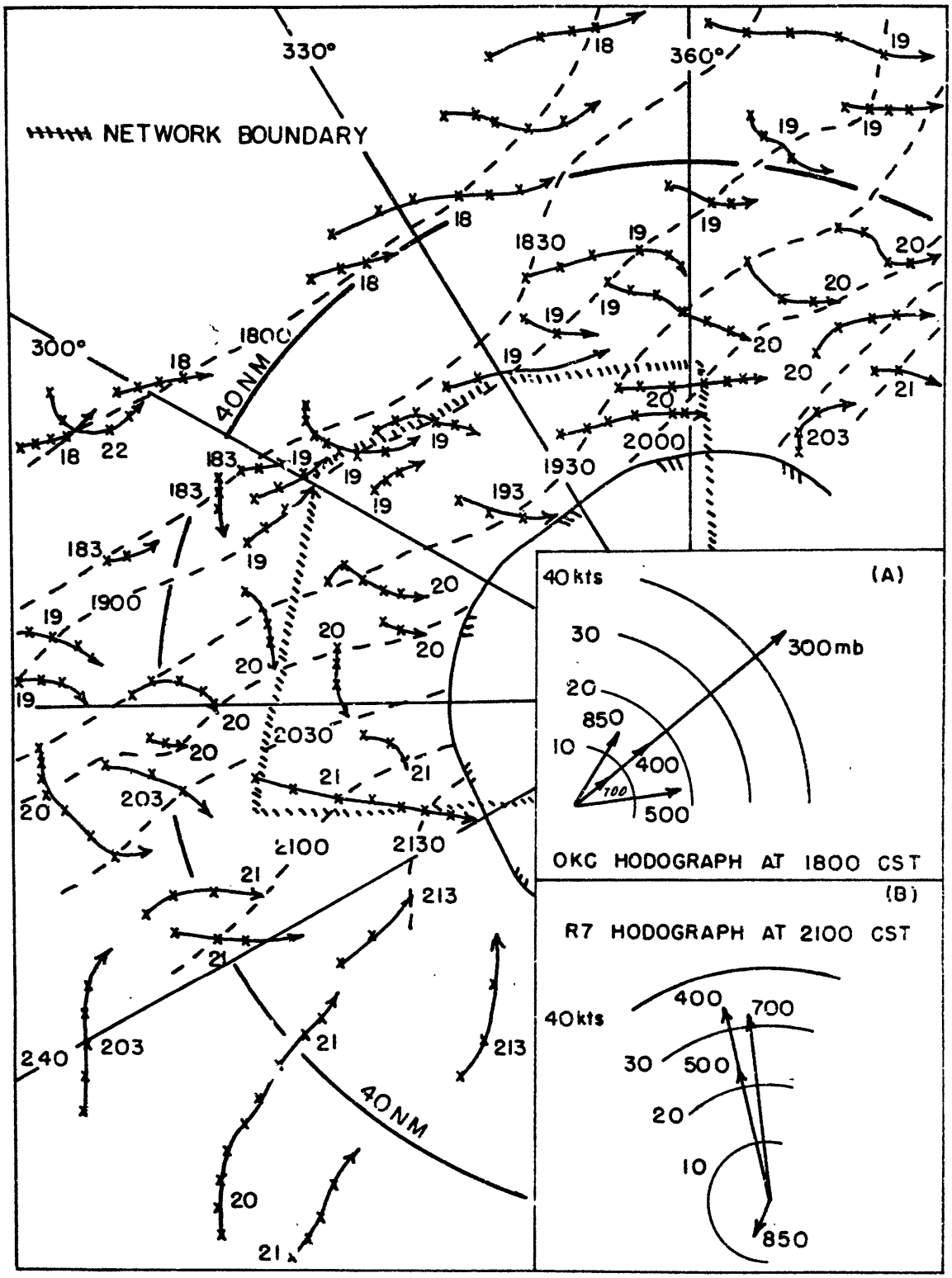

Fig. 6. Tracks of storm cells from 1730 to 2220 CST and wind hodographs at 1800 CST and 2100 CST.

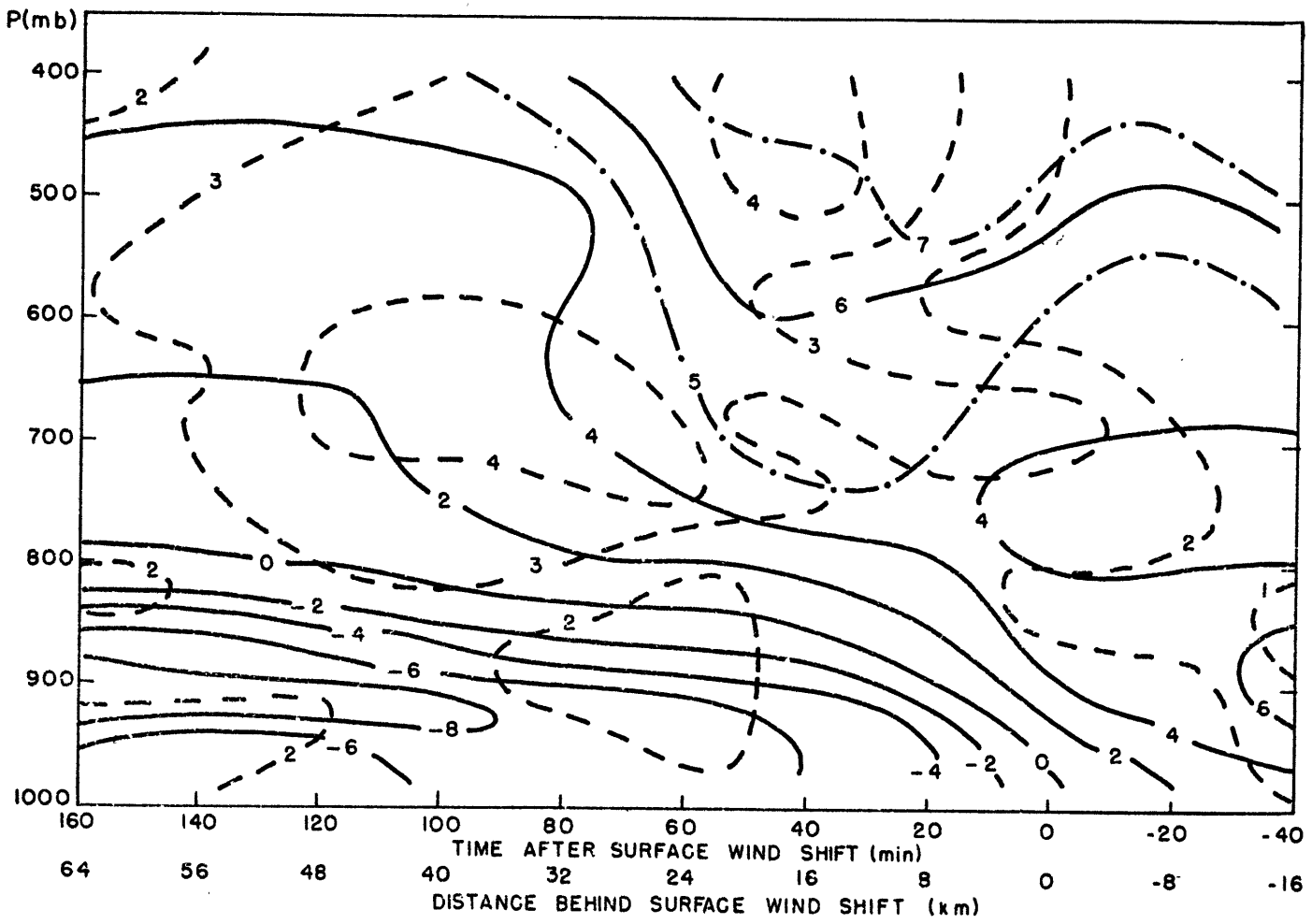

Fig. 7a. Solid lines are version-A values of the u-component of the wind (m sec^{-1}), positive into the page, in a vertical cross section moving with the front. Dashed lines are standard deviation values of u in m sec^{-1}, using samples of about 10 observations each.

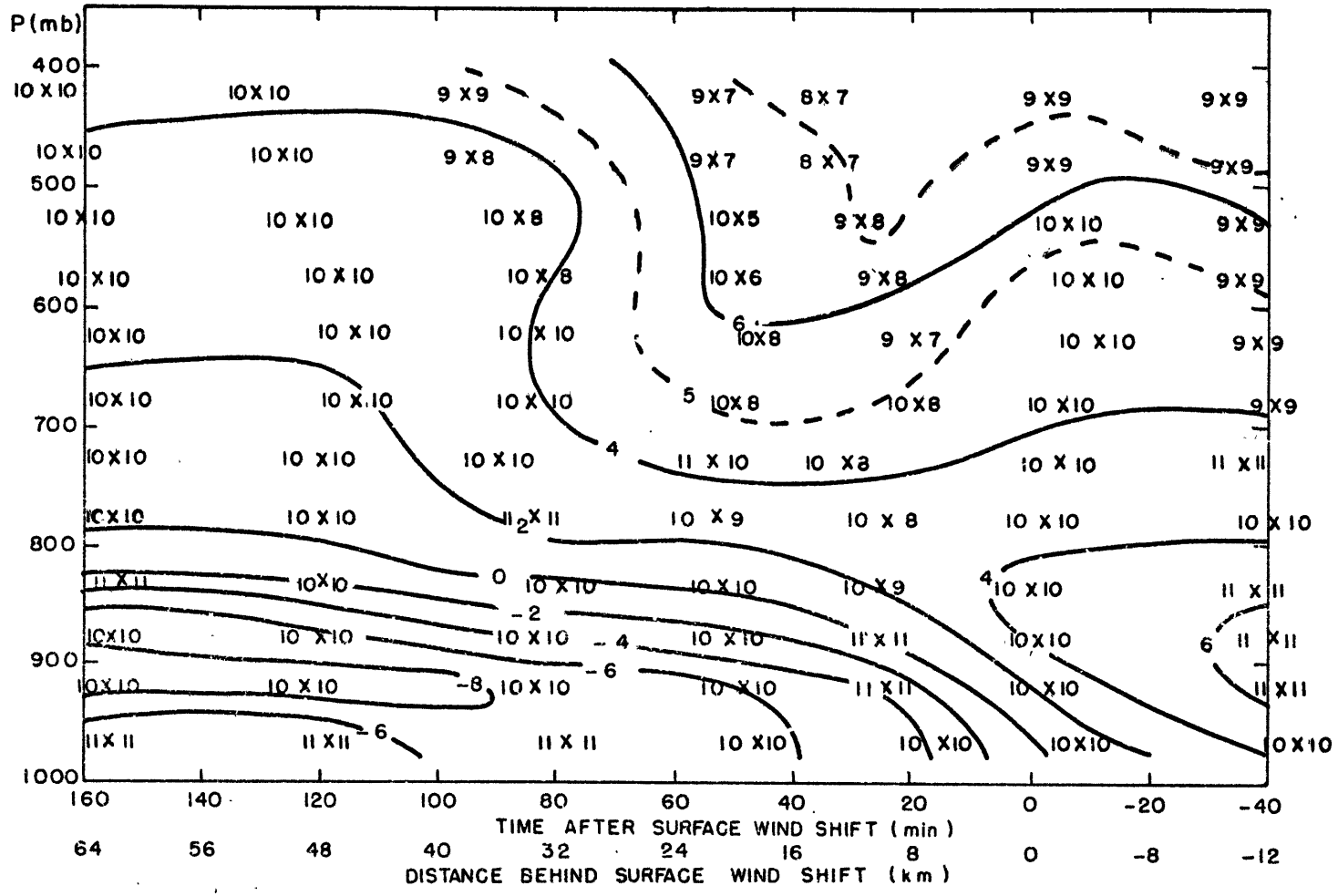

Fig. 7b. Same as Fig. 7a, but for version B.

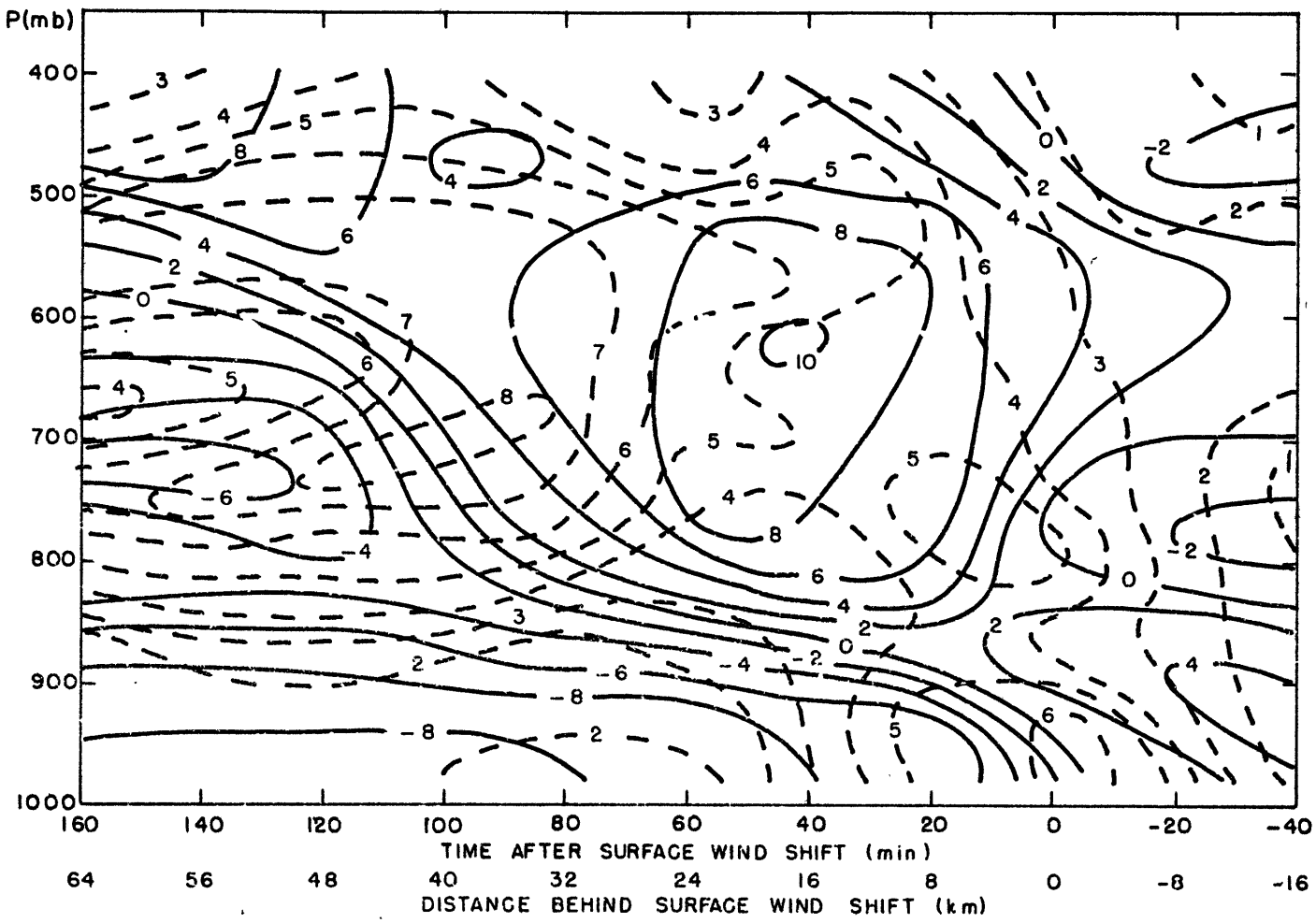

Fig. 8a. Same as Fig. 7, but showing values of the v-component of the wind in m sec^{-1}, positive for air moving toward the left.

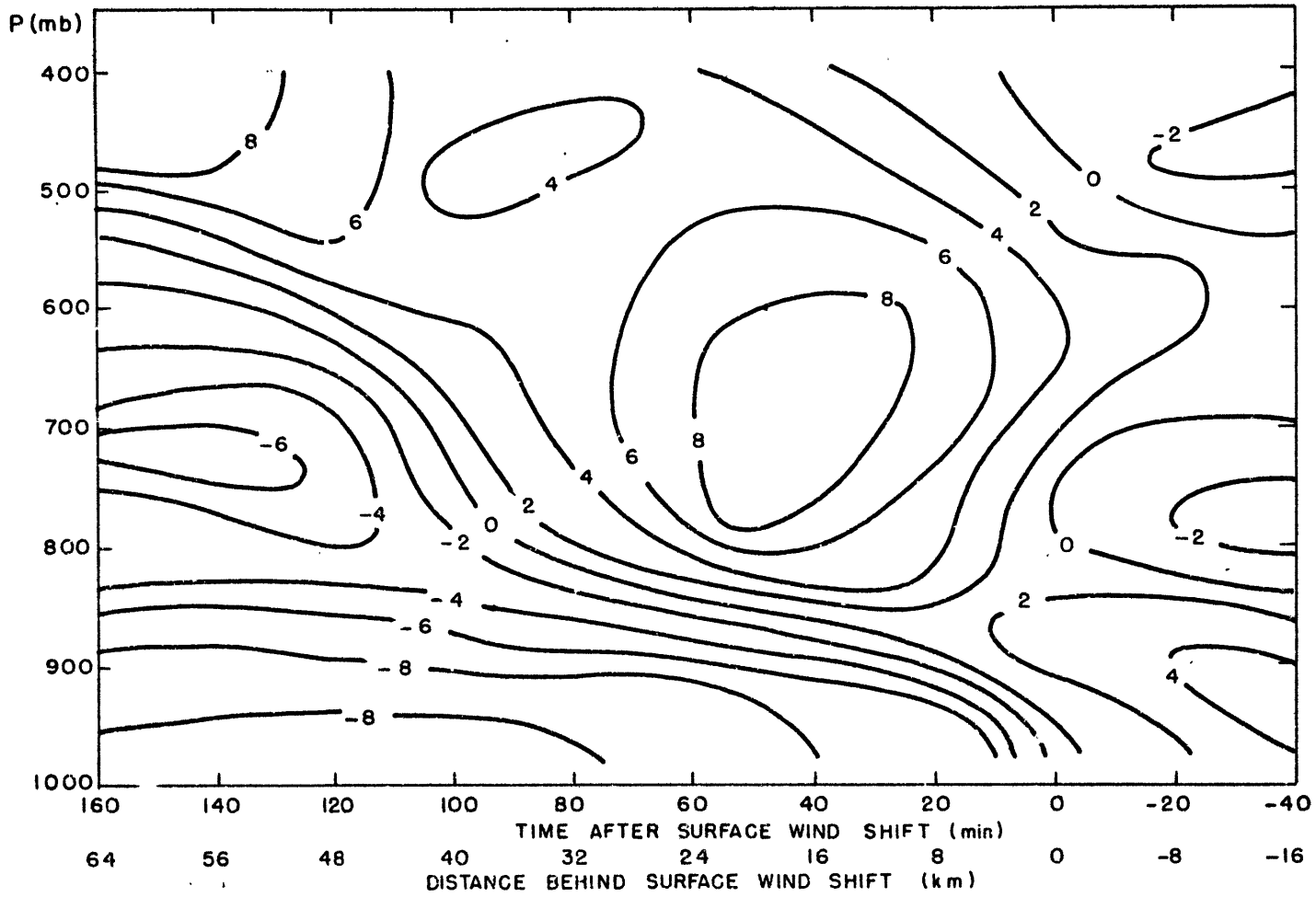

Fig. 8b. Same as Fig. 8a , but for version B.

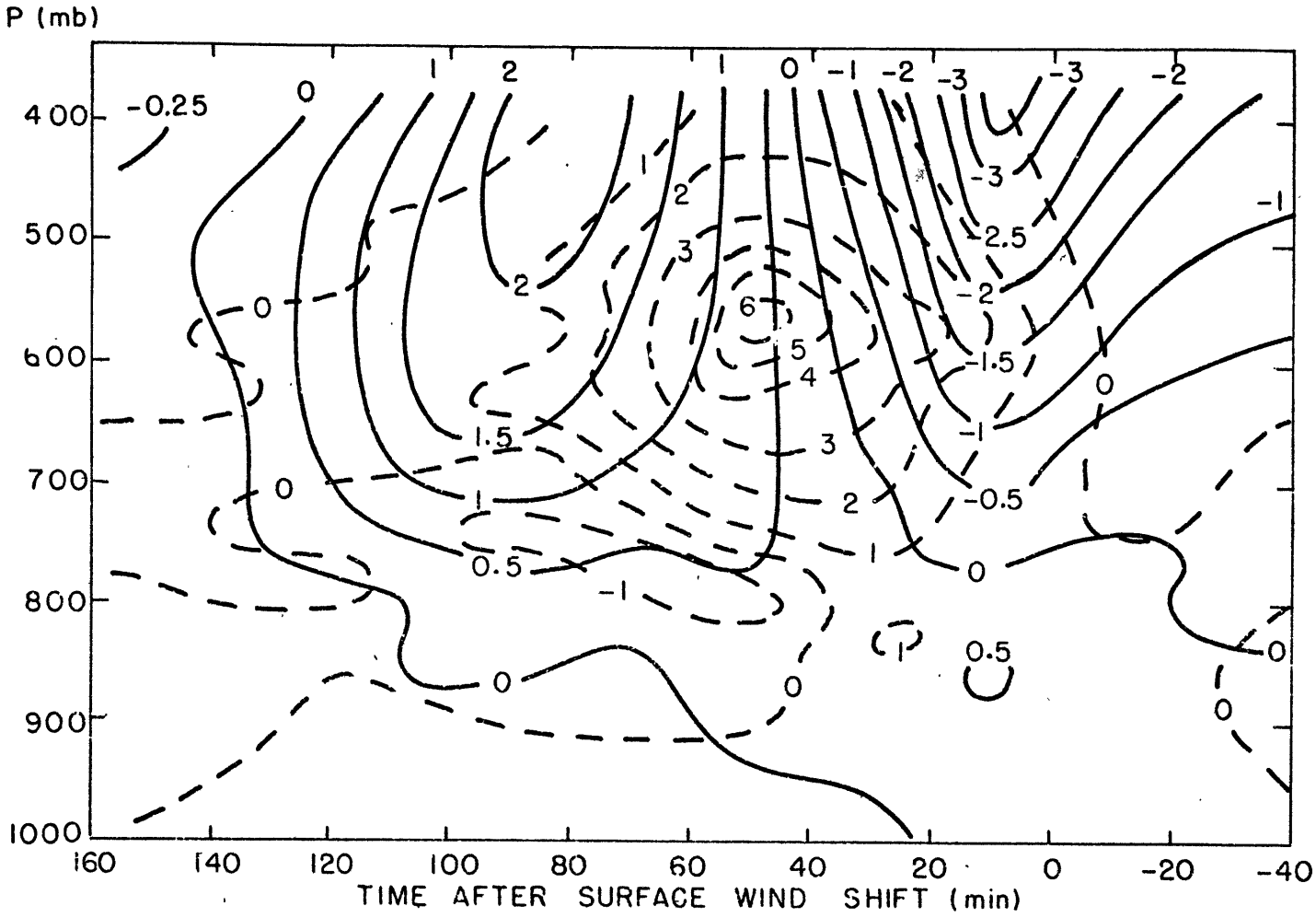

Fig. 9a. A vertical cross section of version-A values of kinematically-determined vertical motions (solid) and net balloon ascent rates (dashed), in m sec^{-1}.

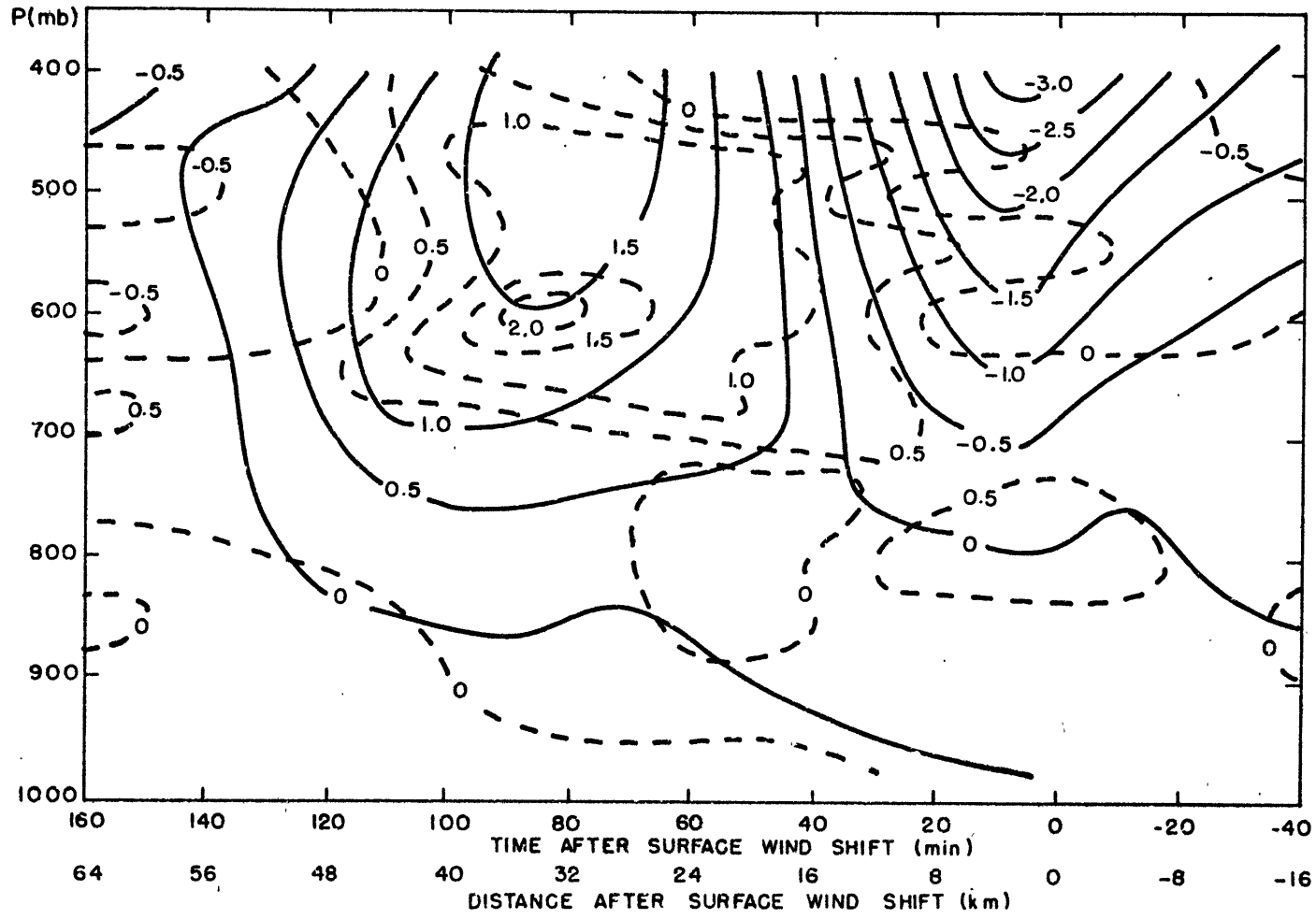

Fig. 9b. Same as 9a, but for version B.

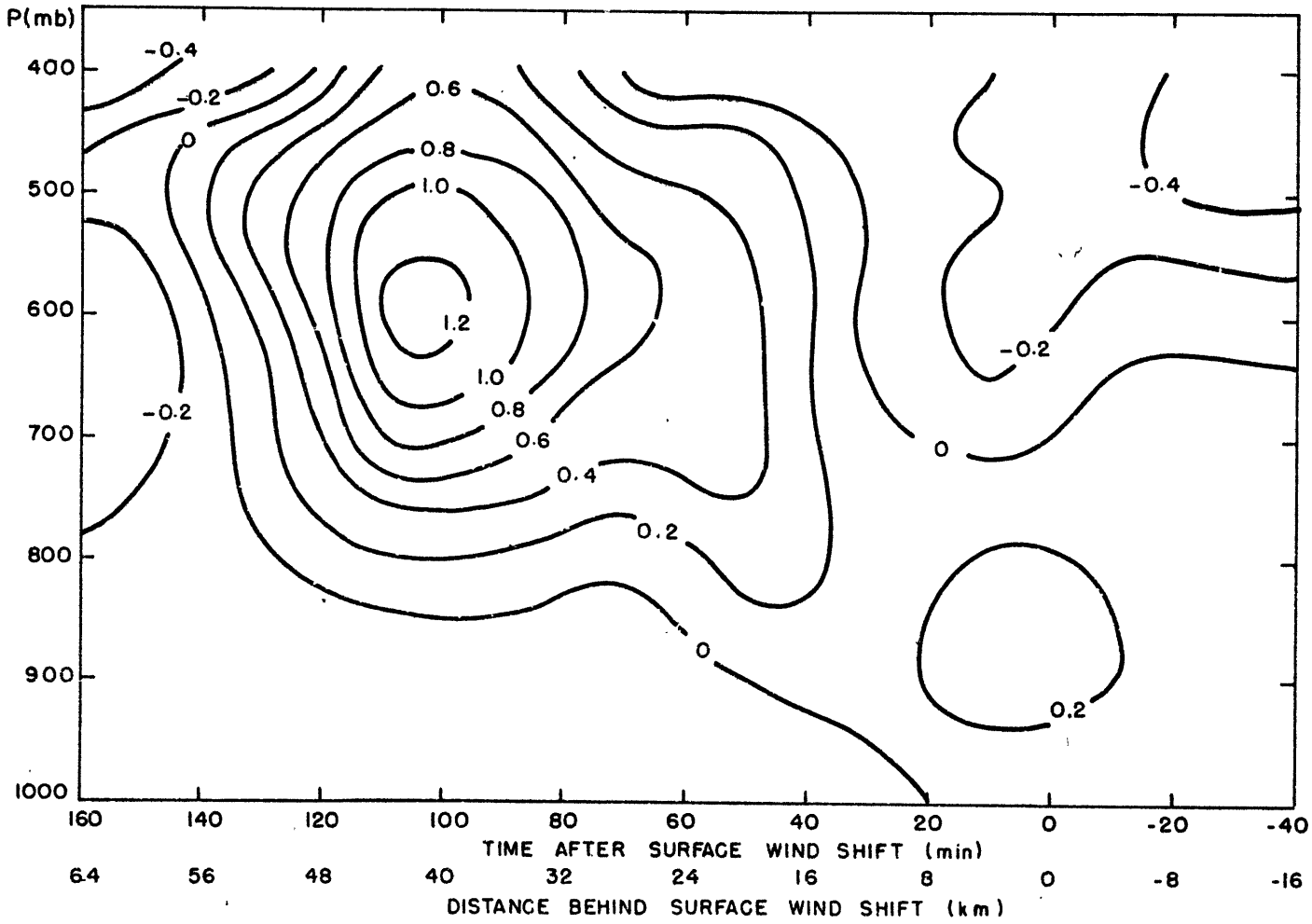

Fig. 9c. Kinematically-determined vertical motions , version C.

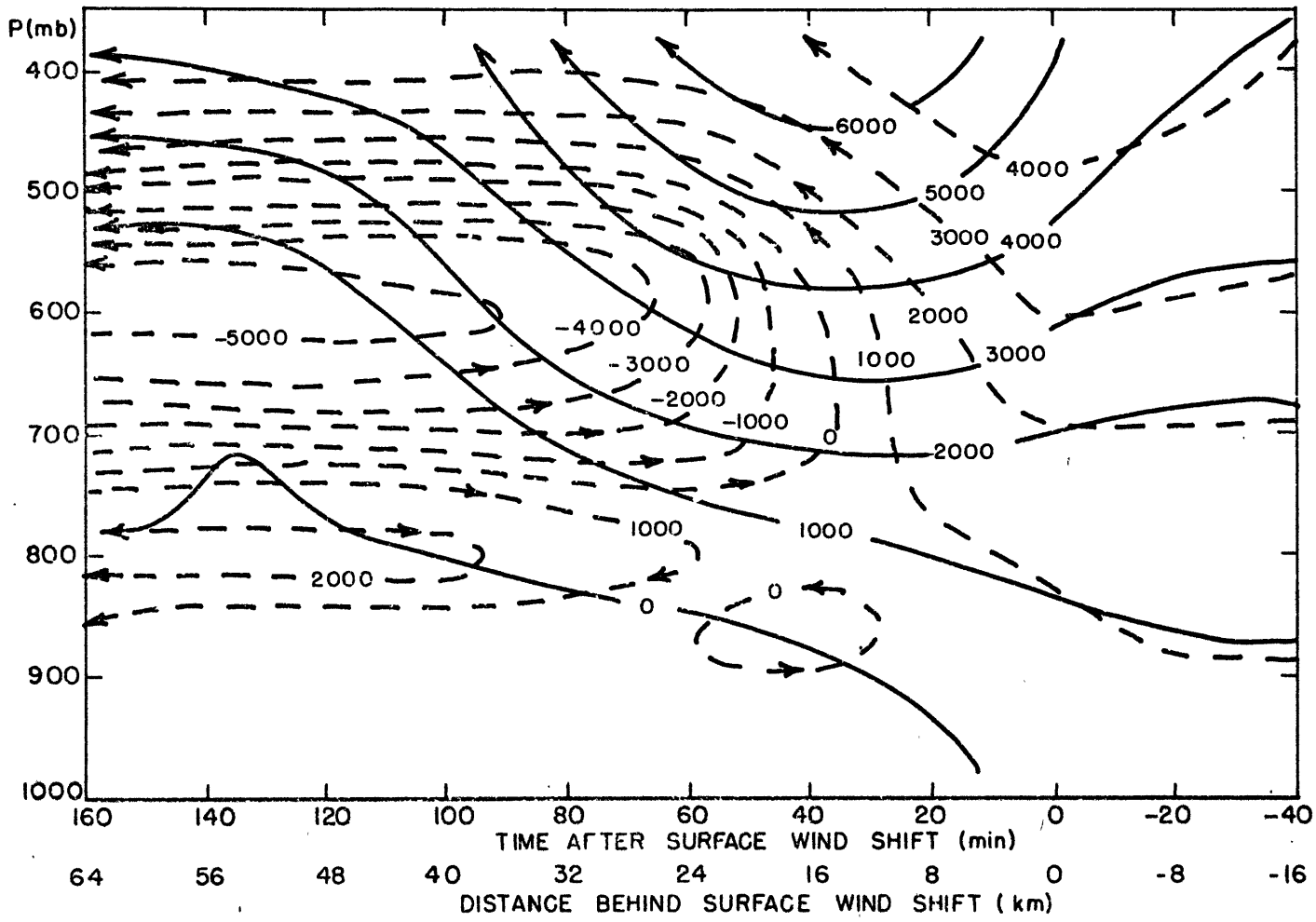

Fig. 10. The v-field, determined by continuity from net balloon ascent rates in Fig. 9a. The observed v-field at -40 min is used as a boundary condition.

caption should be on next page

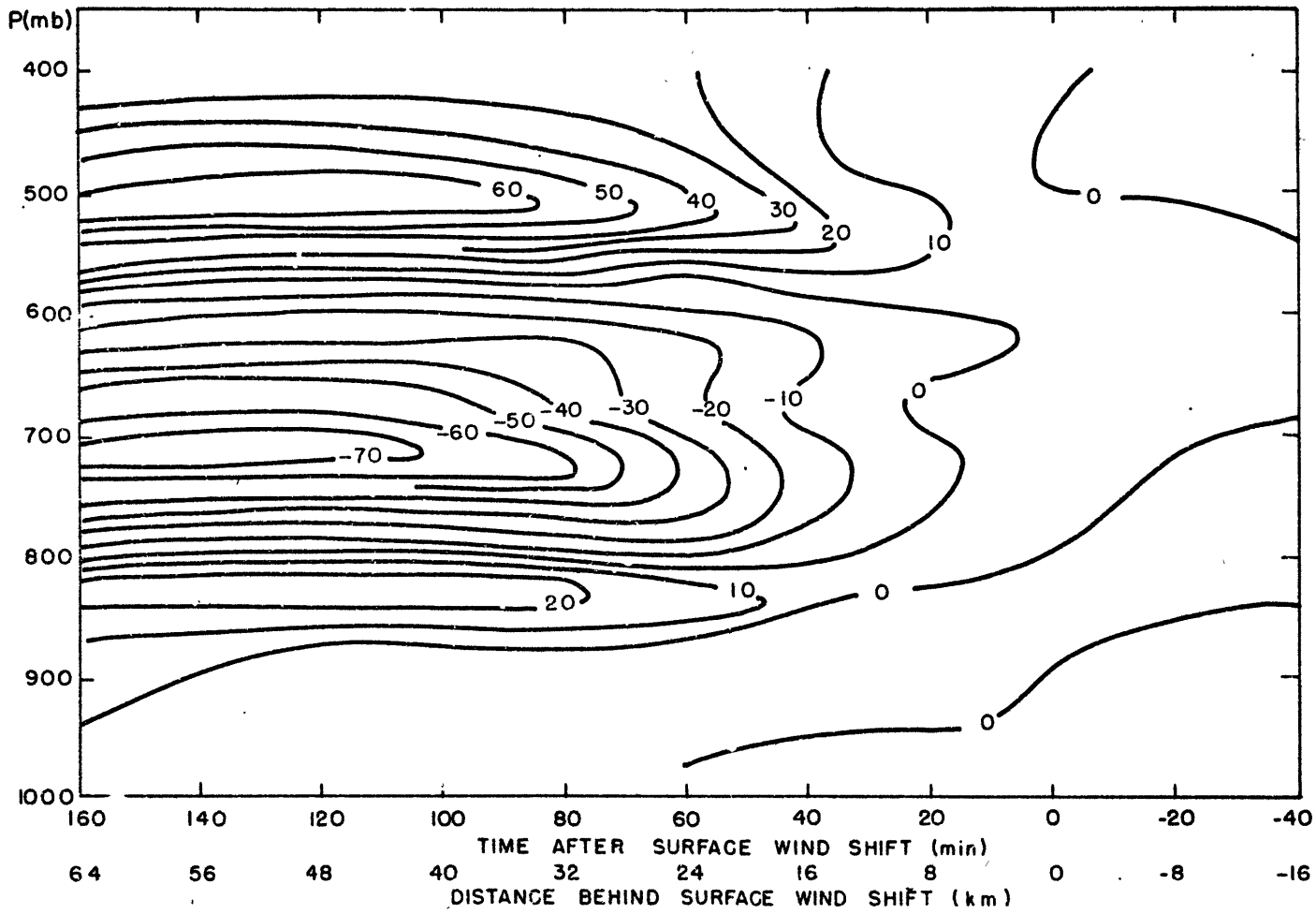

Fig. 10b. Solid lines are two-dimensional streamlines derived from the v-field in Fig. 10a, using equation 6b. The observed ψ field is shown by dashed lines.

caption should be on preceding page.

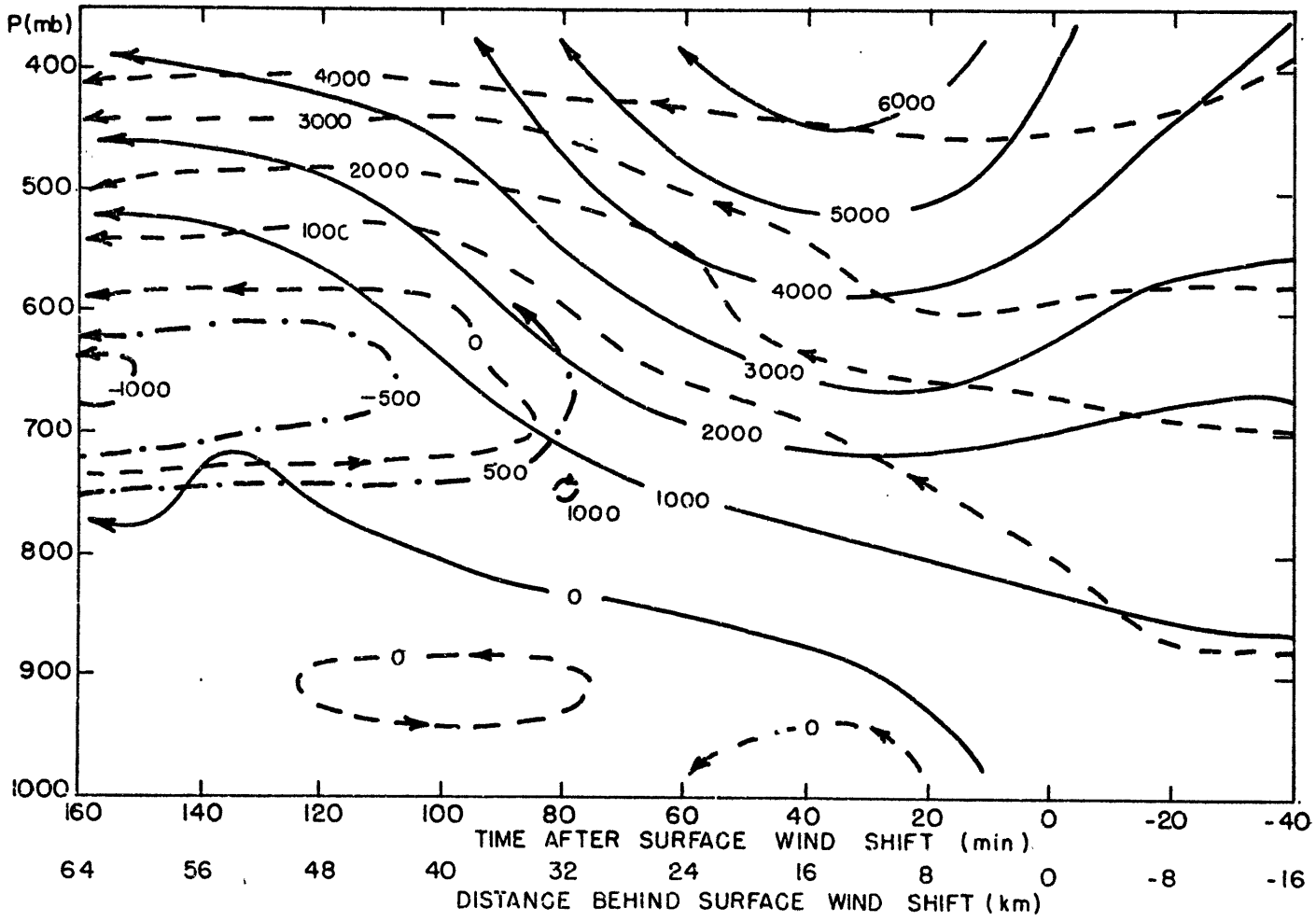

Figs. 10c and 10d. The same as Figs. 10a and 10b, but using net balloon ascent rates from Fig. 9b.

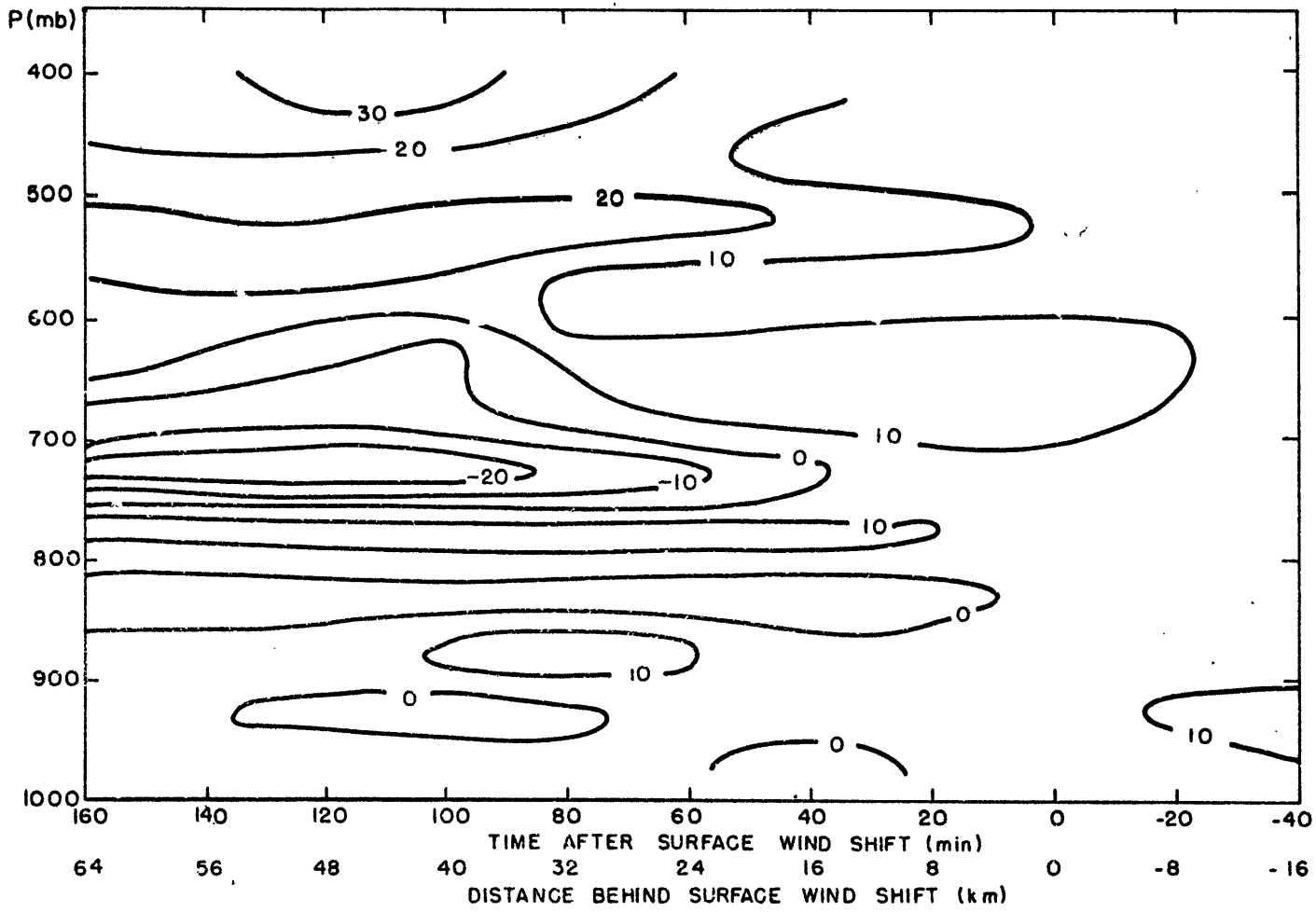
P(mb)
400
500
600
700
800
900
1000
30
20
20
10
10
0
-20
-10
10
0
10
0
10
0
160
140
120
100
80
60
40
20
0
-20
-40
TIME AFTER SURFACE WIND SHIFT (min)
64
56
48
40
32
24
16
8
0
-8
-16
DISTANCE BEHIND SURFACE WIND SHIFT (km)

Fig. 10d.

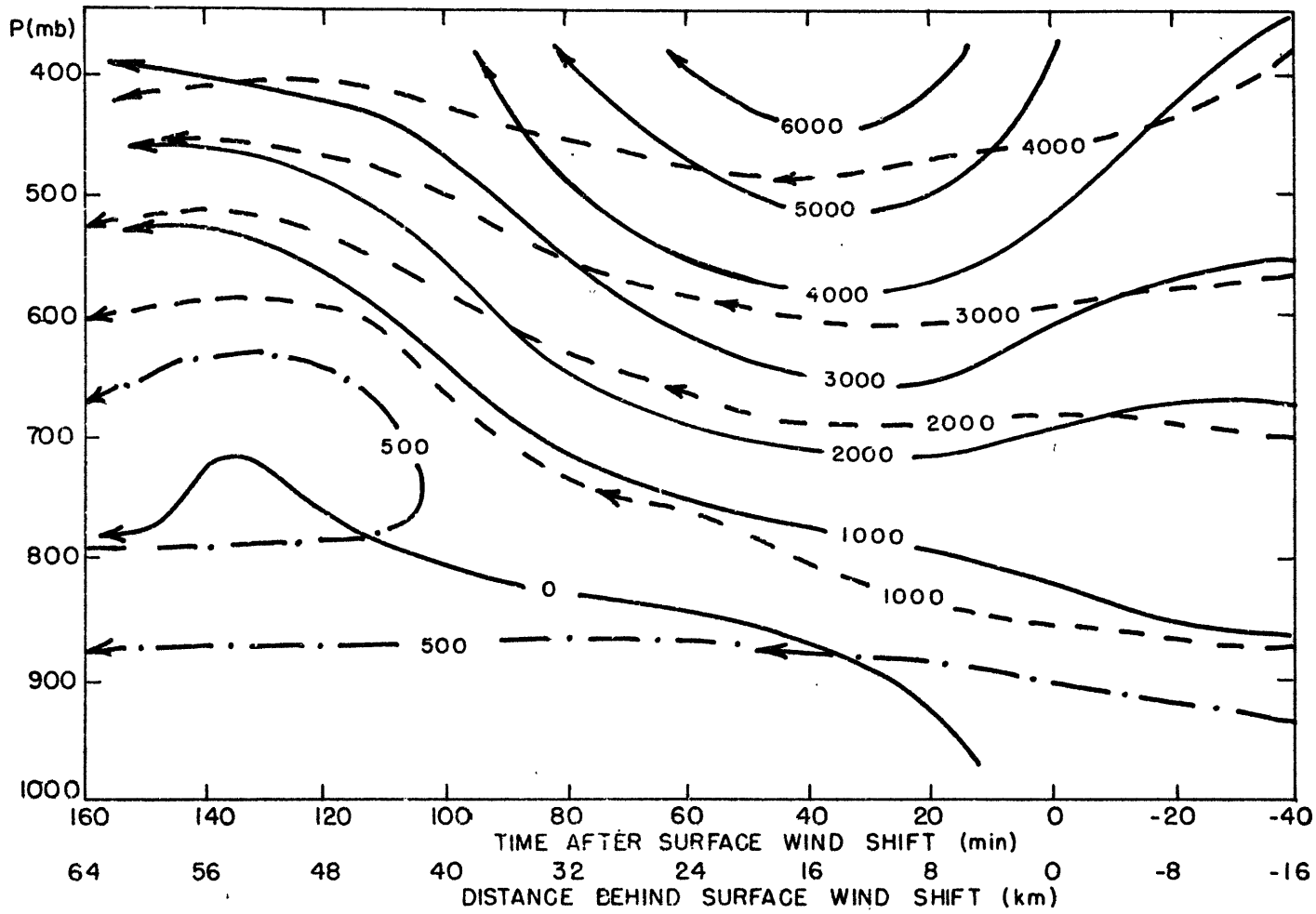

Figs. 10e and 10f. The same as Figs. 10a and 10b, but using the vertical-motion field from Fig. 9c.

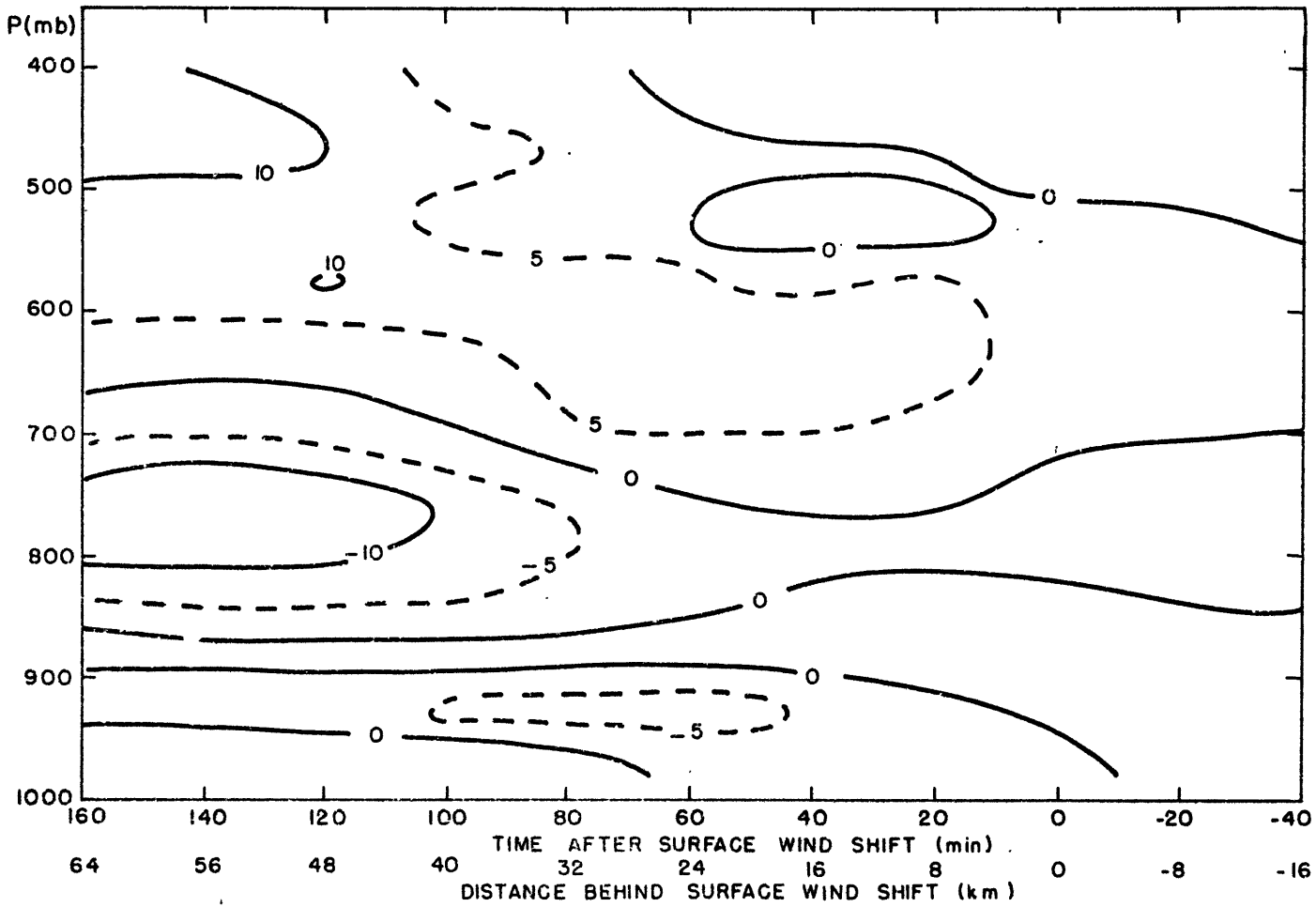
P(mb)
400
500
600
700
800
900
1000
10
10
5
0
0
5
0
-10
-5
0
0
-5
160
140
120
100
80
60
40
20
0
-20
-40
TIME AFTER SURFACE WIND SHIFT (min)
64
56
48
40
32
24
16
8
0
-8
-16
DISTANCE BEHIND SURFACE WIND SHIFT (km)

Fig. 10f.

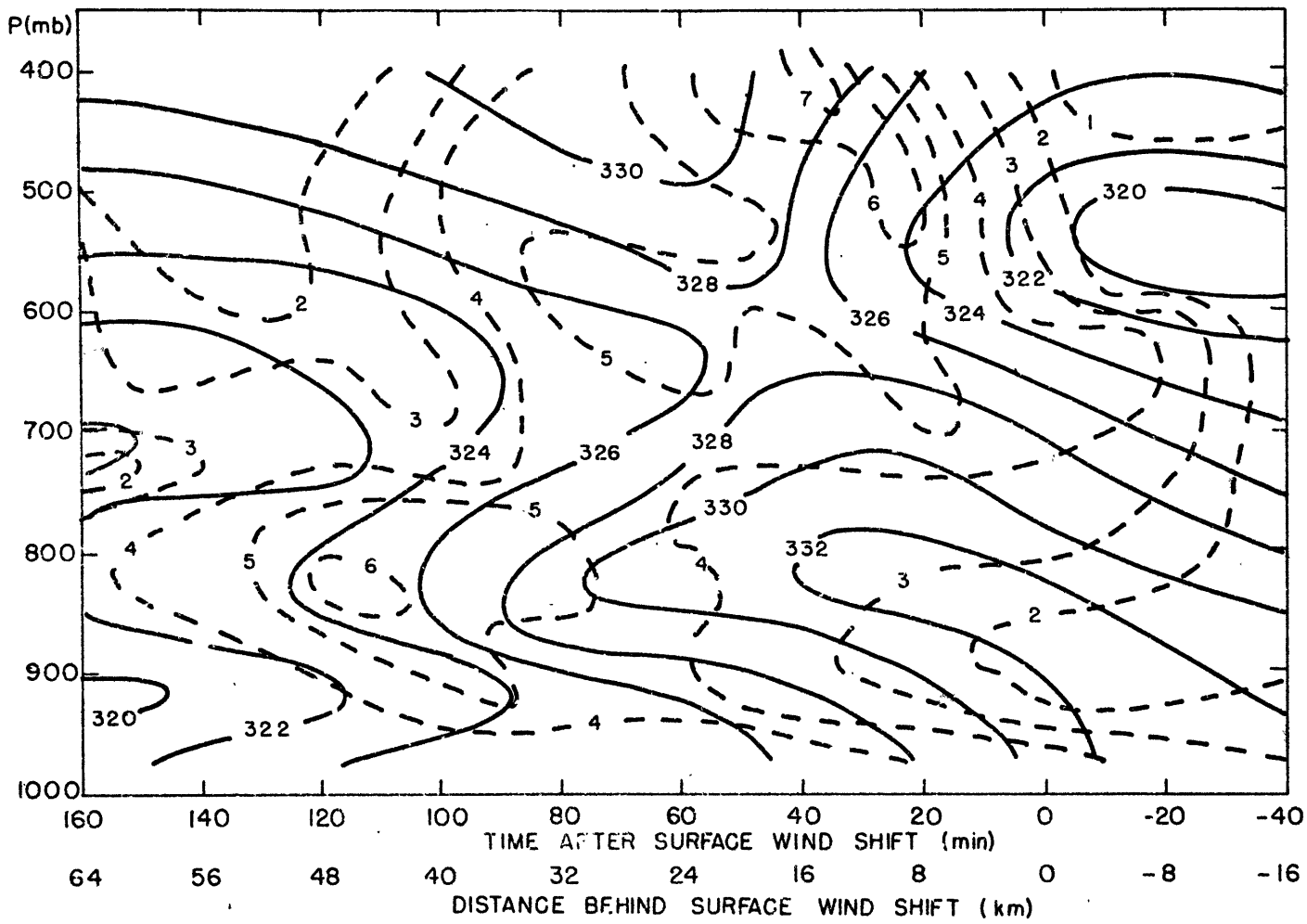

Fig. 11a. Solid lines are equivalent-potential temperature values(°K), version A. Standard deviation values (°K) are shown by dashed lines.

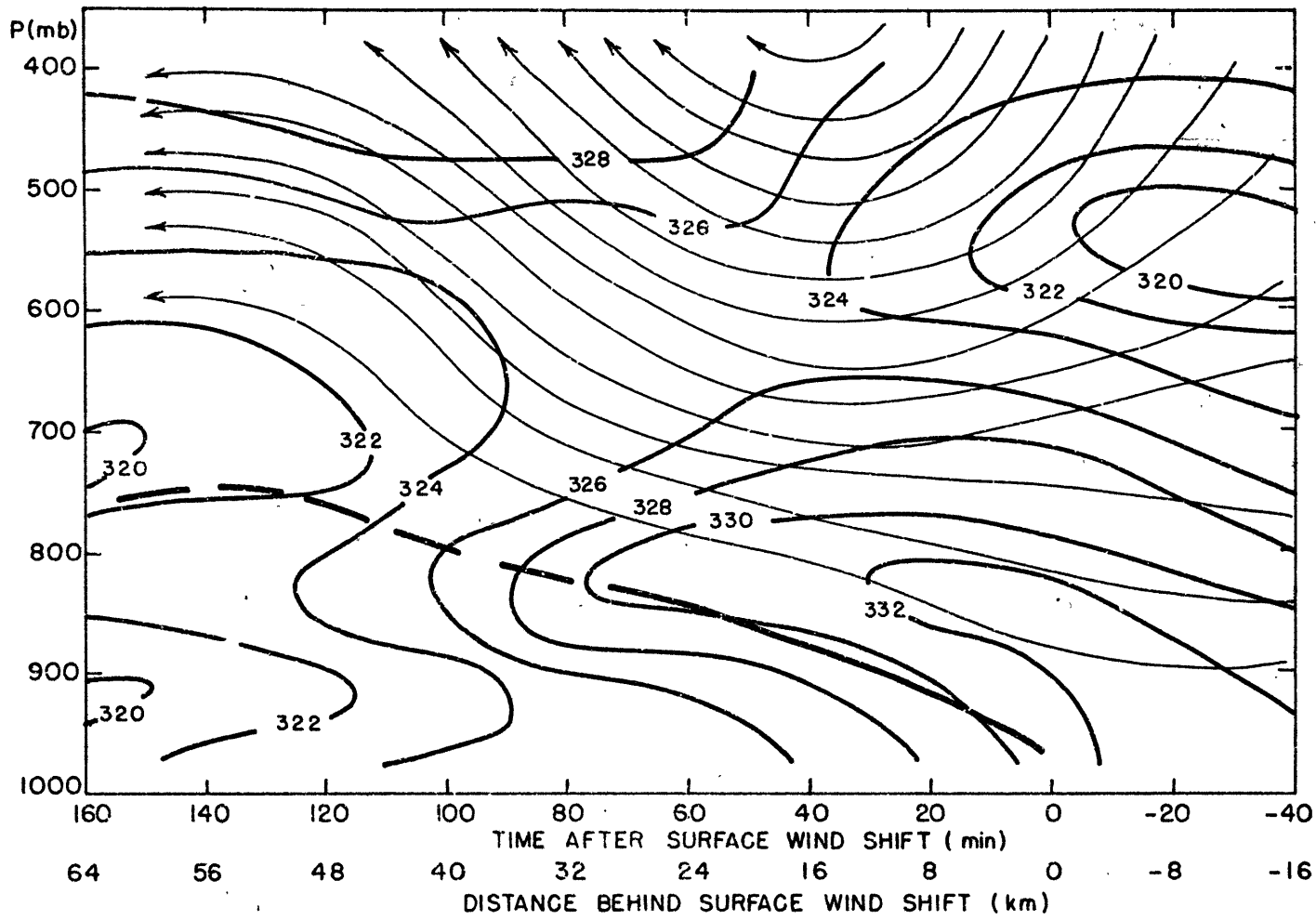

Fig. 11b. Solid lines are equivalent-potential temperature values, version B. Dashed lines are observed trajectories.

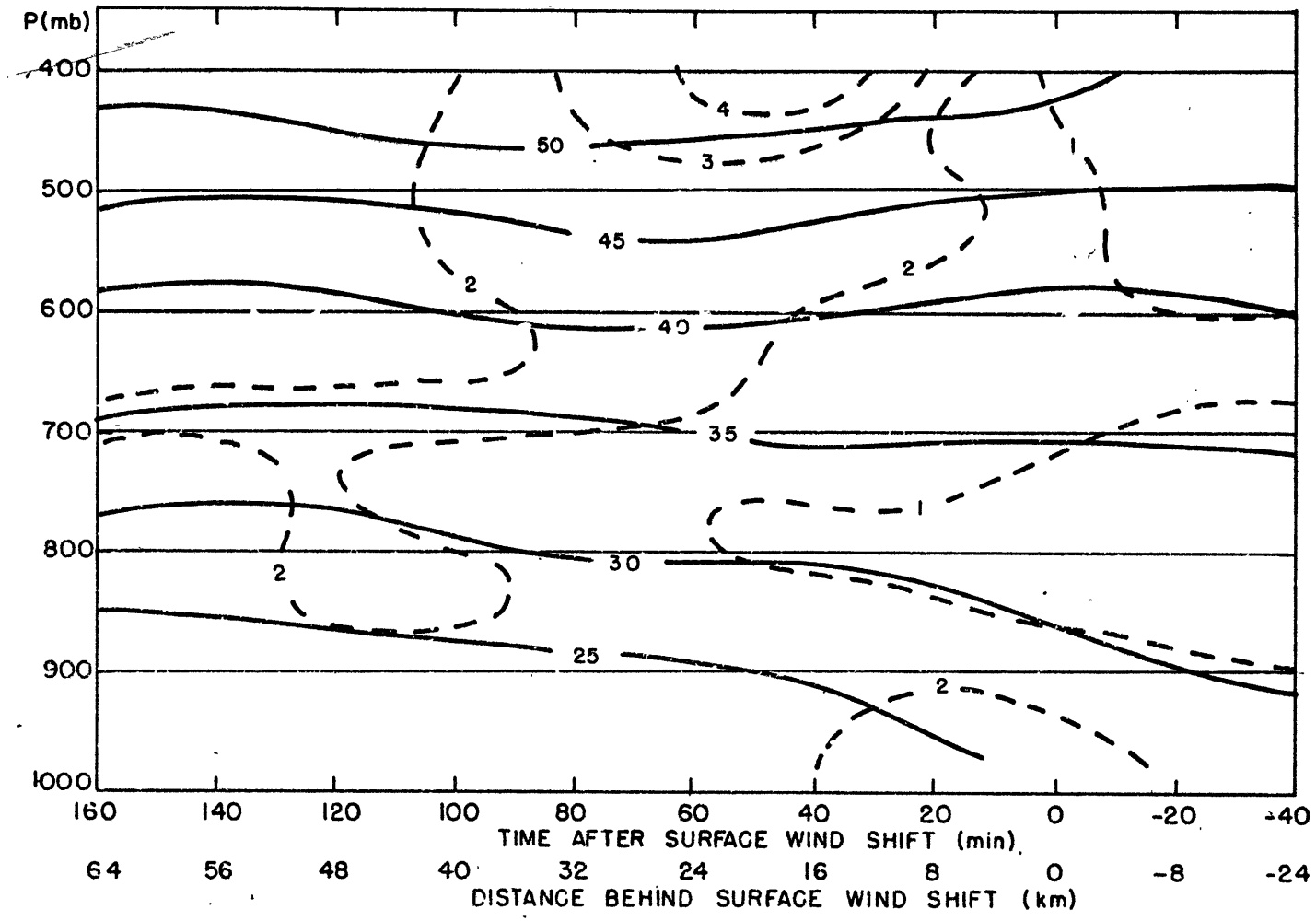

Figs. 12a and 12b. The same as Fig. 11, but for potential temperature (°C).

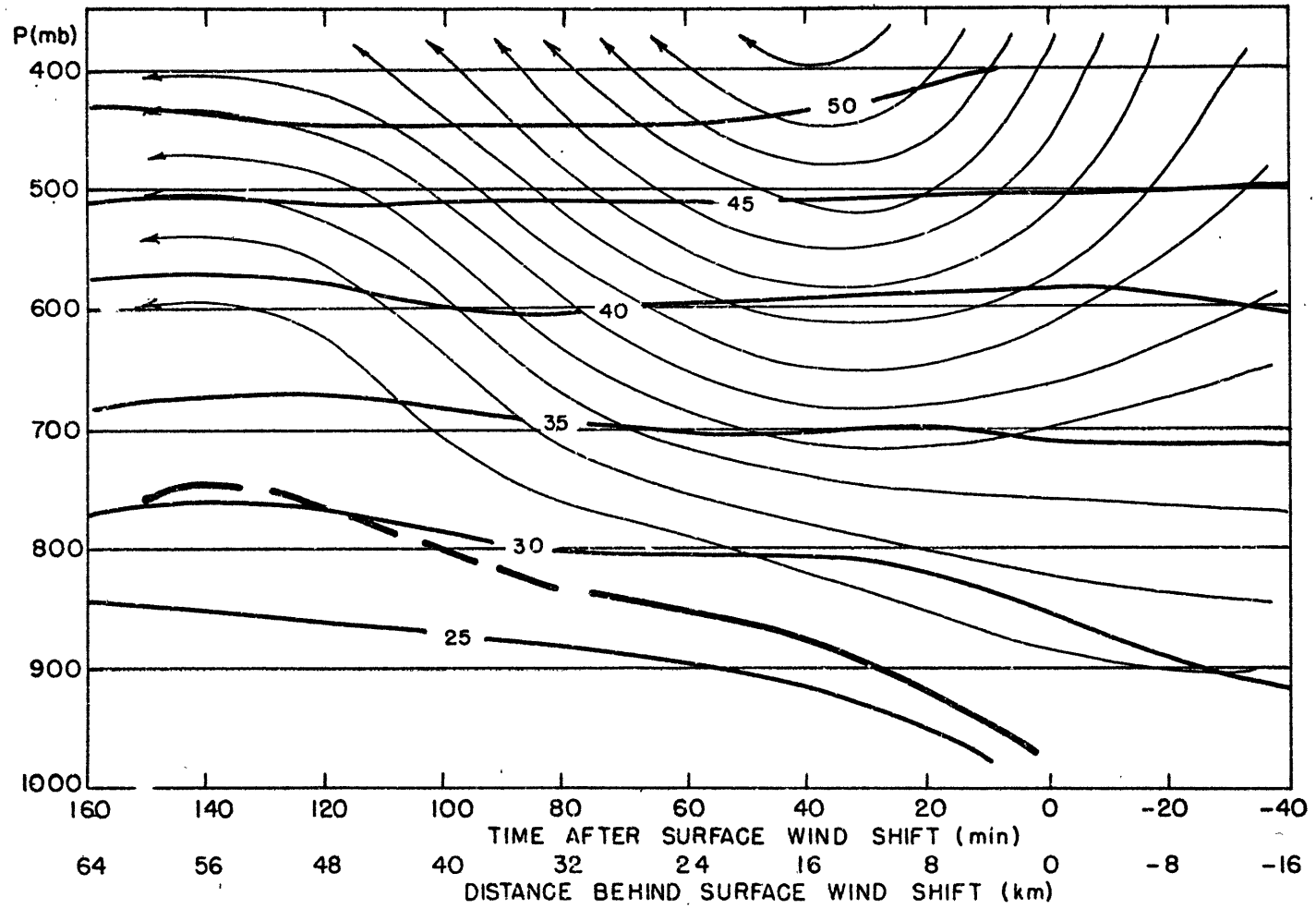
P(mb)
400
500
600
700
800
900
1000
50
45
40
35
30
25
160
140
120
100
80
60
40
20
0
-20
-40
TIME AFTER SURFACE WIND SHIFT (min)
64
56
48
40
32
24
16
8
0
-8
-16
DISTANCE BEHIND SURFACE WIND SHIFT (km)

Fig. 12b.

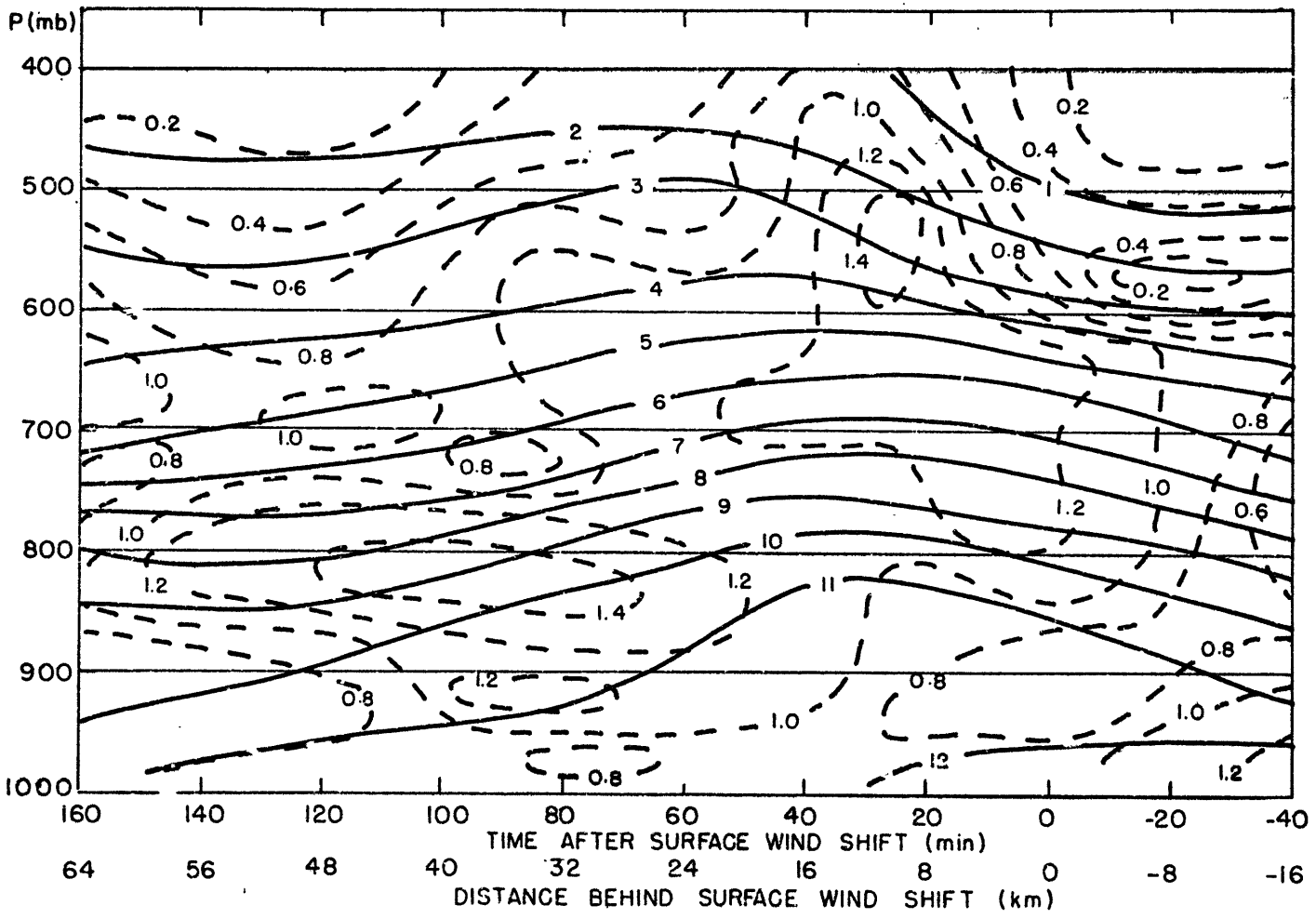

Figs. 13a and 13b. The same as Fig. 11, but for mixing ratio (gm kg^{-1}).

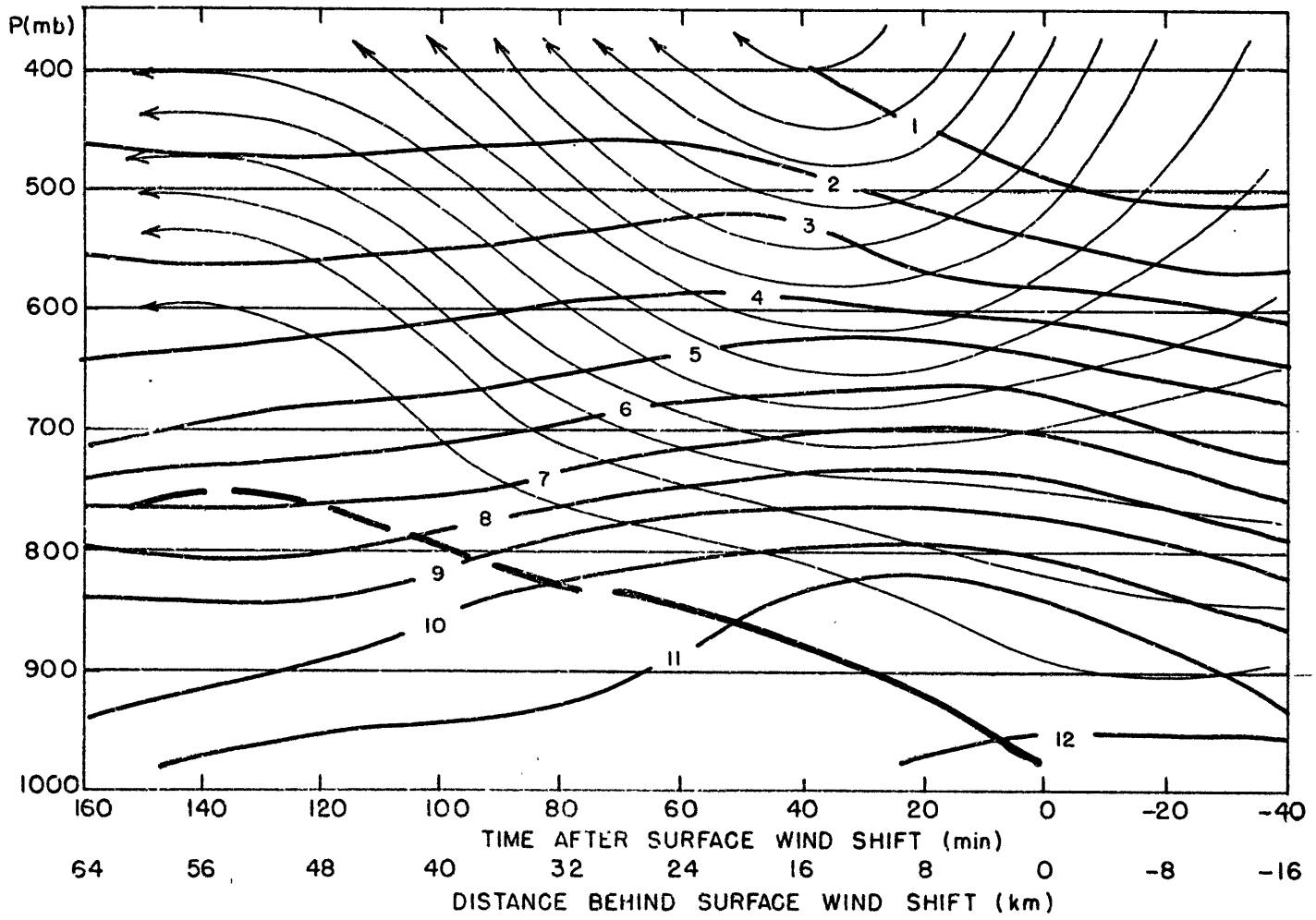
P(mb)
400
500
600
700
800
900
1000
1
2
3
4
5
6
7
8
9
10
11
12
160
140
120
100
80
60
40
20
0
-20
-40
TIME AFTER SURFACE WIND SHIFT (min)
64
56
48
40
32
24
16
8
0
-8
-16
DISTANCE BEHIND SURFACE WIND SHIFT (km)

Fig. 13b.

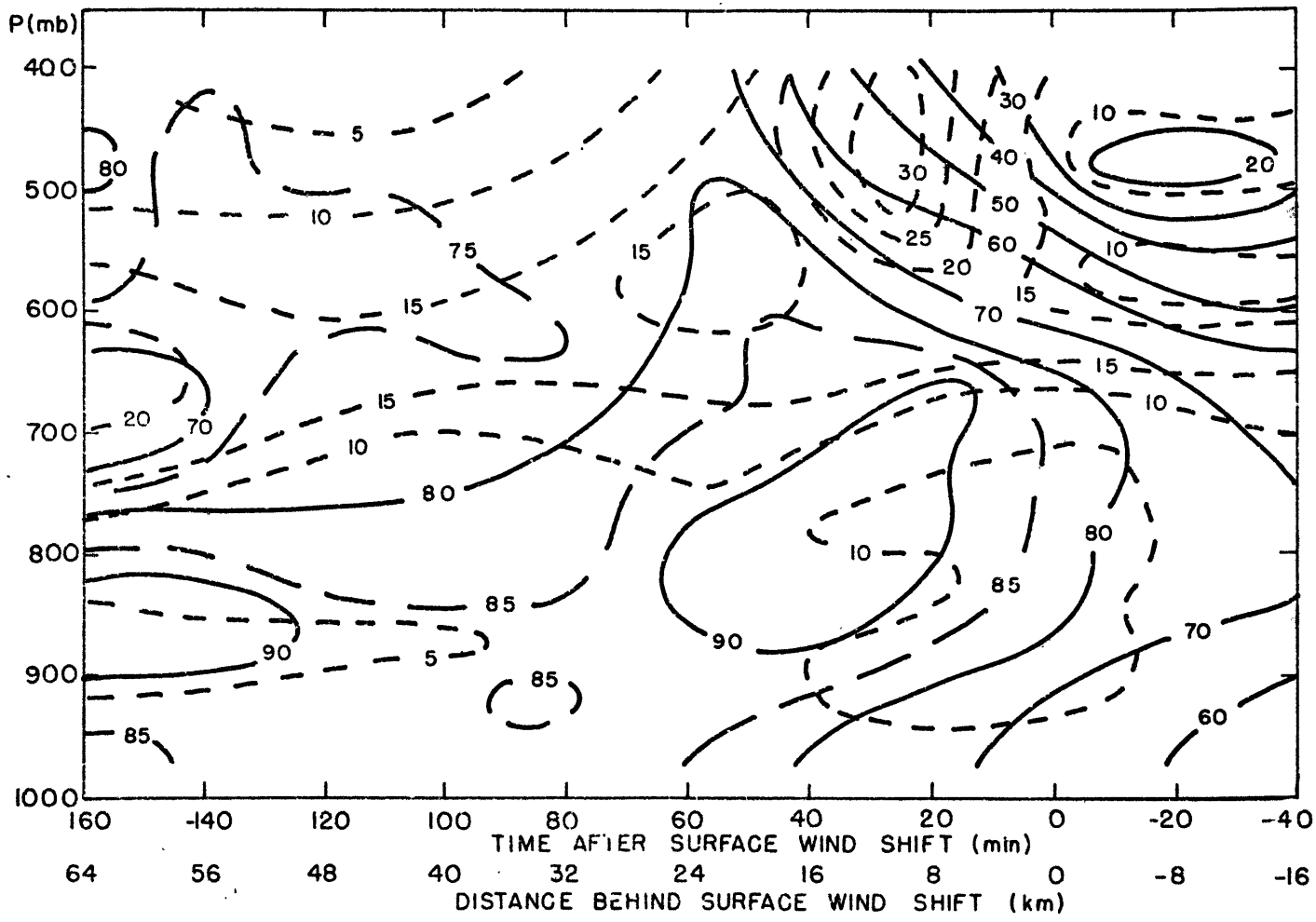

Figs. 14a and 14b. The same as in Fig 11, but for relative humidity (%).

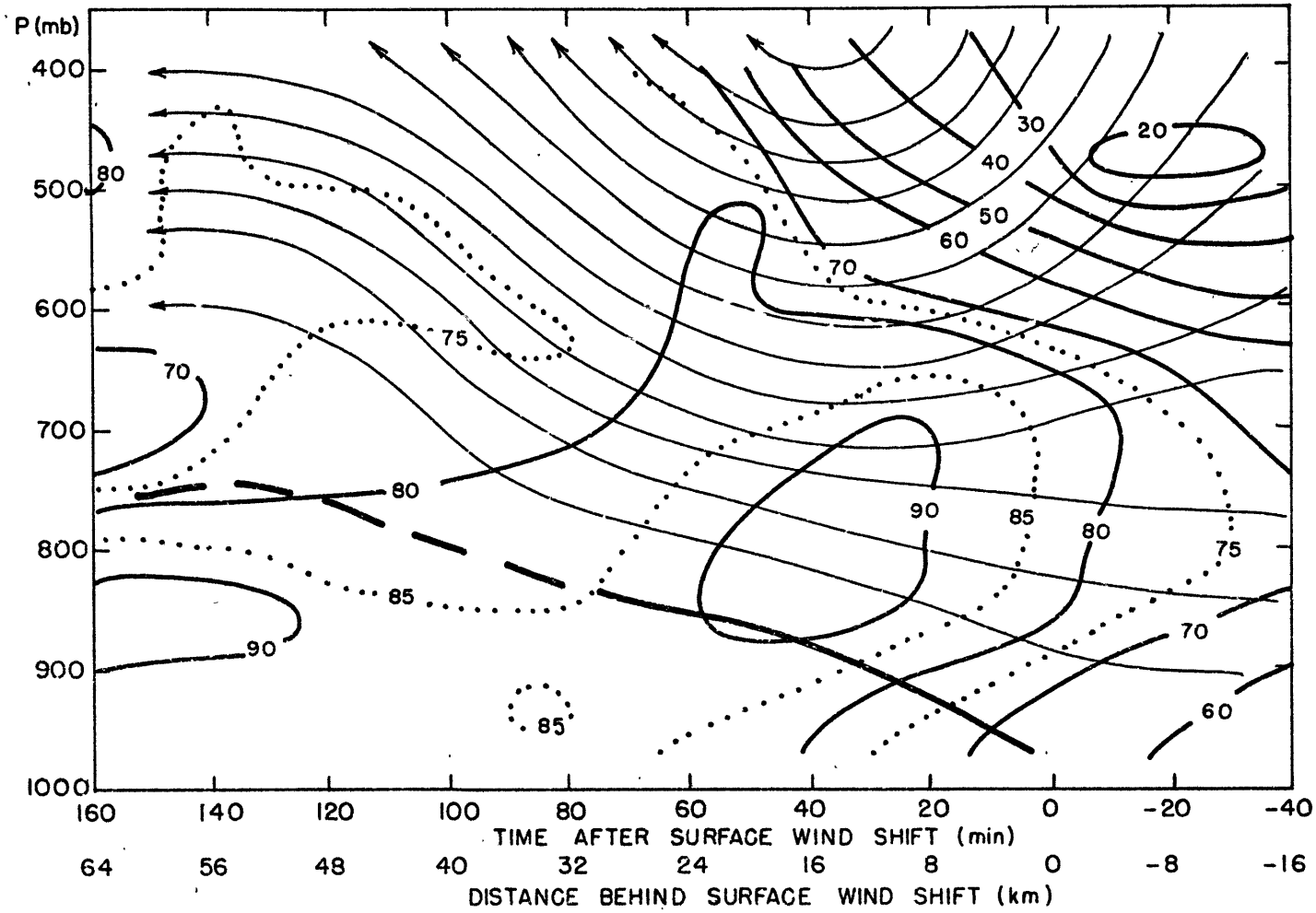
P (mb)
400
500
600
700
800
900
1000
80
70
75
80
85
90
85
30
40
50
60
70
20
90
85
80
75
70
60
160
140
120
100
80
60
40
20
0
-20
-40
TIME AFTER SURFACE WIND SHIFT (min)
64
56
48
40
32
24
16
8
0
-8
-16
DISTANCE BEHIND SURFACE WIND SHIFT (km)

Fig. 14b.

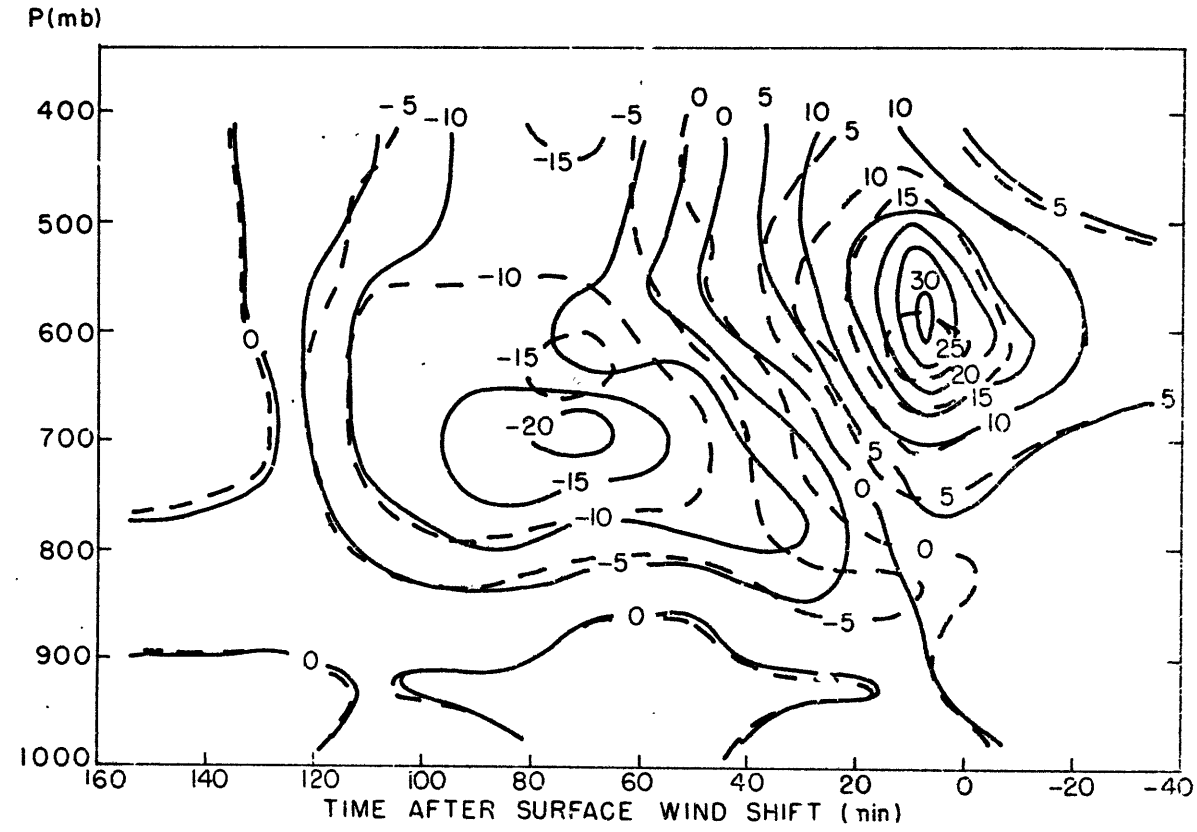

Fig. 15a. In the top half, solid lines are values of

$$\frac{\partial \bar{q}}{\partial t} + \frac{\partial}{\partial x}(\bar{u}\bar{q}) + \frac{\partial}{\partial y}(\bar{v}\bar{q}) + \frac{\partial}{\partial p}(\overline{\omega q}),$$

version A, in gm kg^{-1}/min^{-1} x 10^{-2}. Dashed lines represent version B. In the bottom half, the surface rainfall rate is shown in cm hr^{-1}.

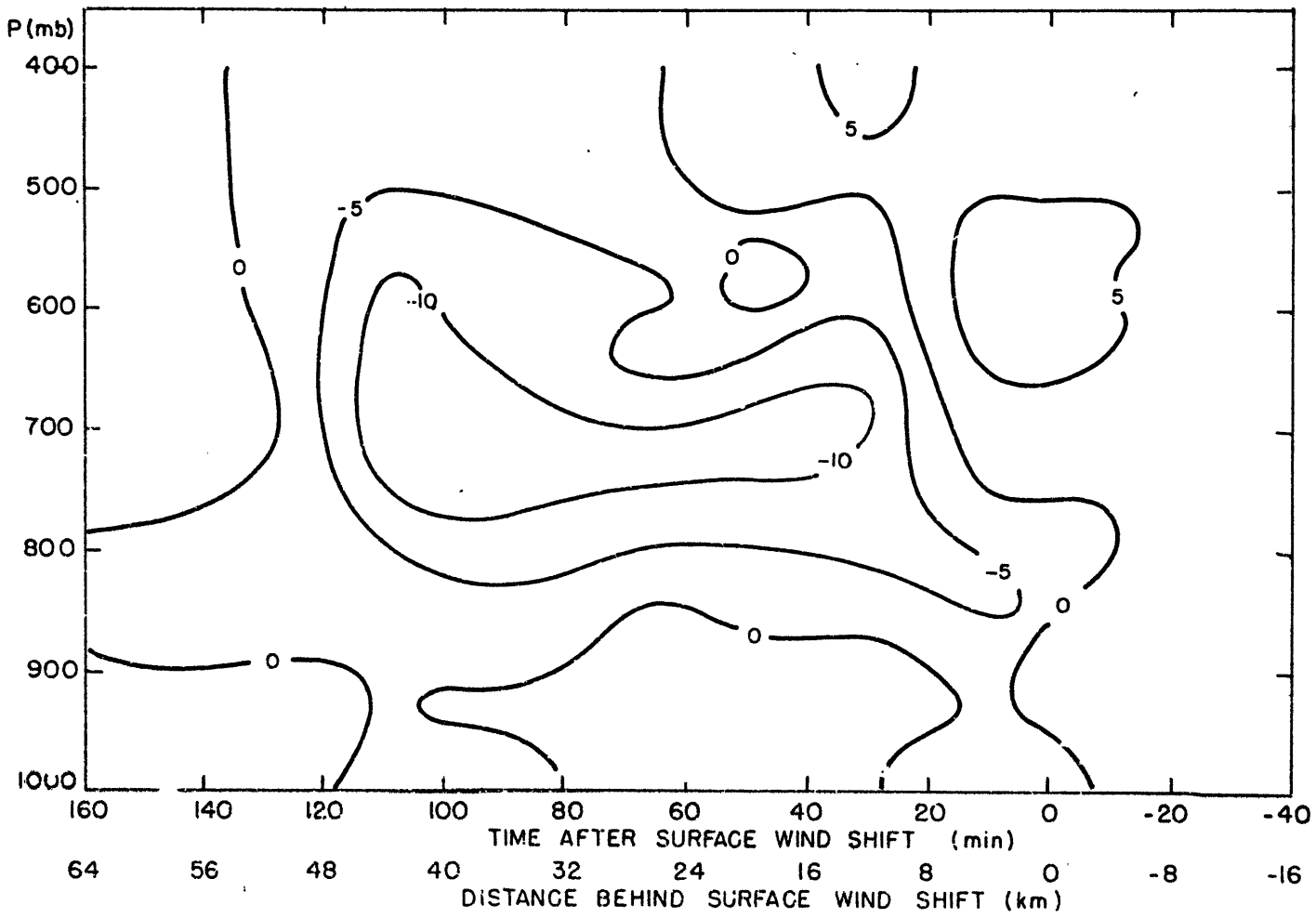

Fig. 15b. Similar to the dashed version of Fig. 15a (top half), but vertical-motion values from Fig. 9c instead of from 9b.

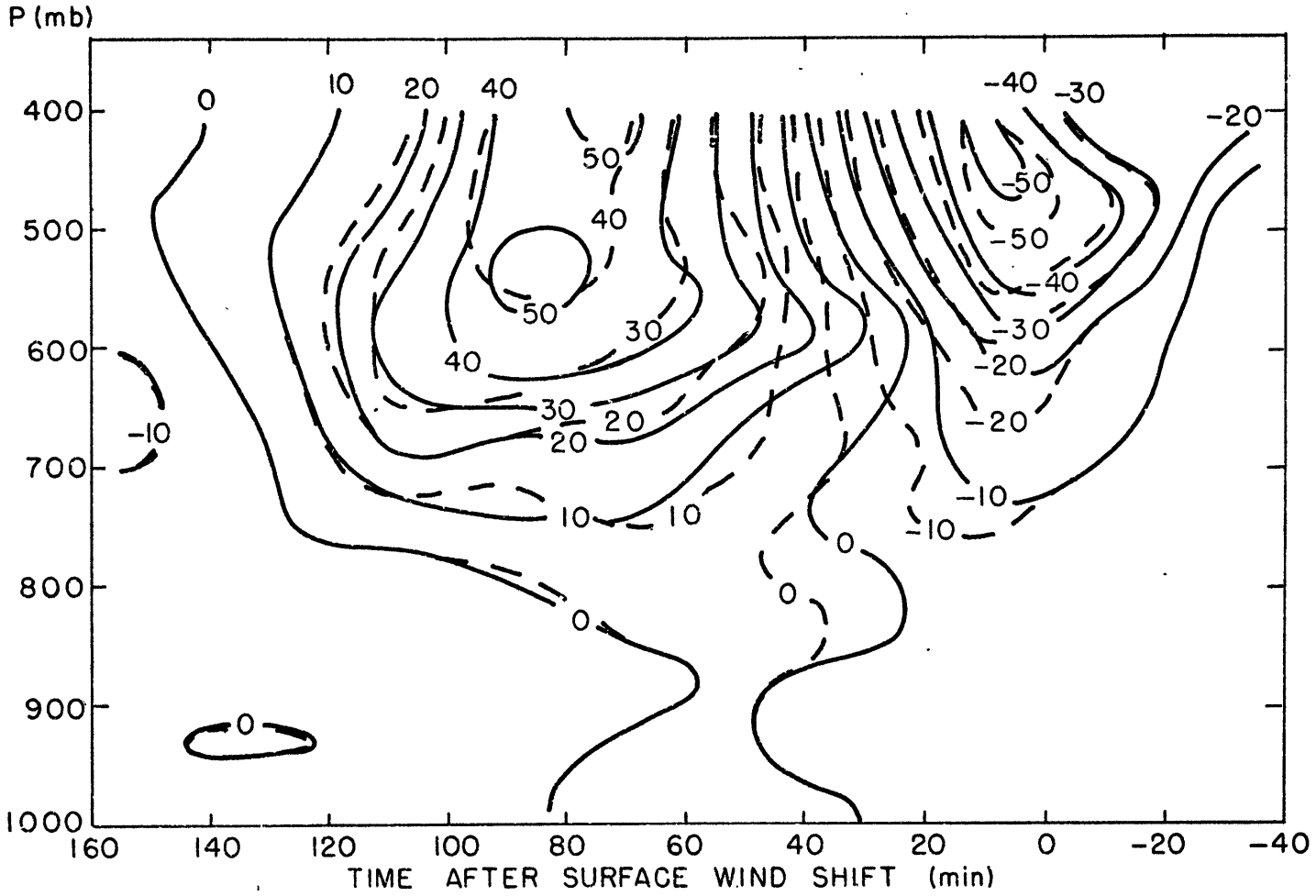

Fig. 16a. Similar to Fig. 15a, but for $\frac{\partial \bar{\theta}}{\partial t} + \frac{\partial}{\partial x}(\bar{u}\bar{\theta}) + \frac{\partial}{\partial y}(\bar{v}\bar{\theta}) + \frac{\partial}{\partial p}(\bar{\omega}\bar{\theta})$, in units of $^{o}C\ min^{-1} \times 10^{-2}$.

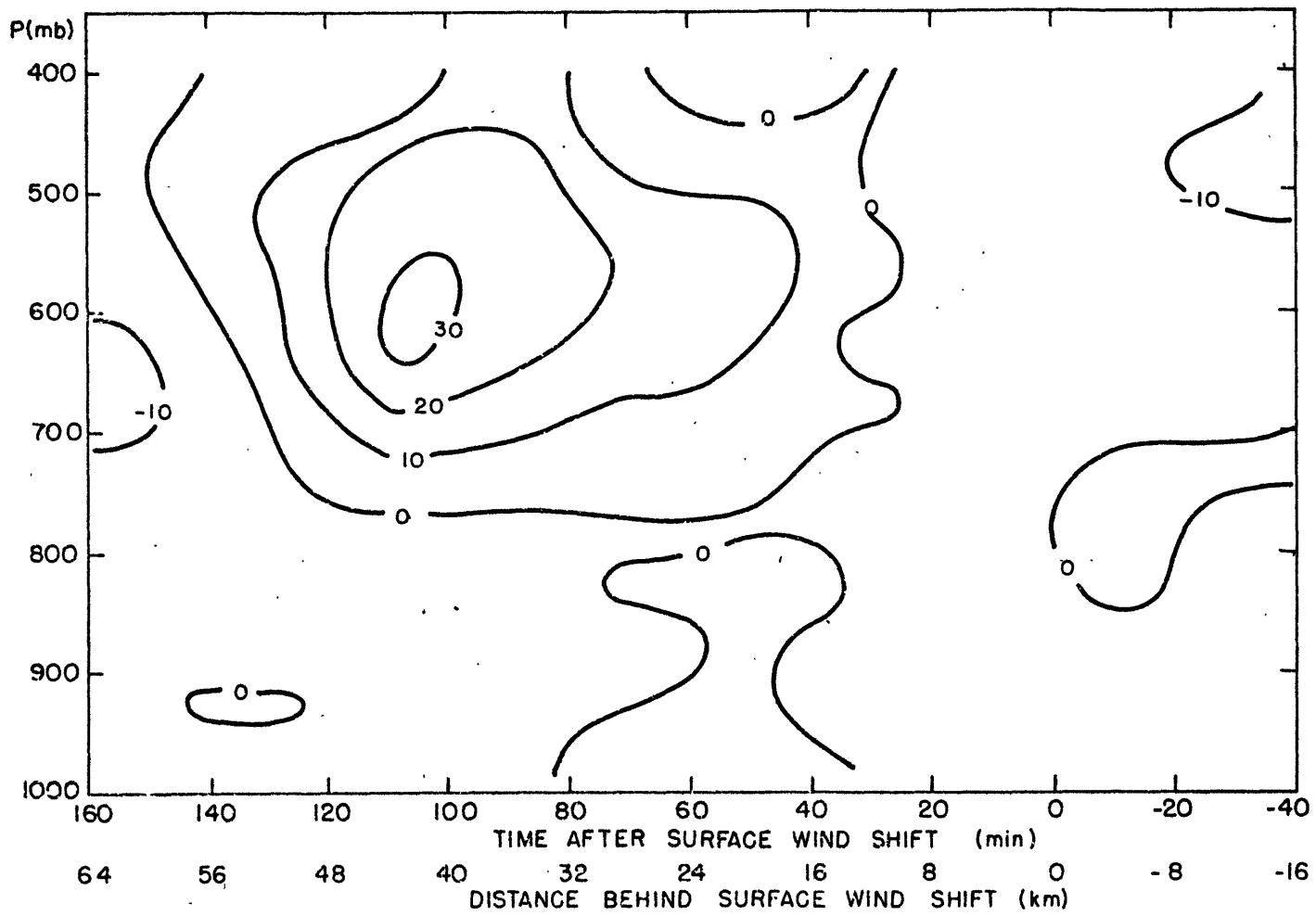

Fig. 16b. Same as Fig. 16a, but for version C.

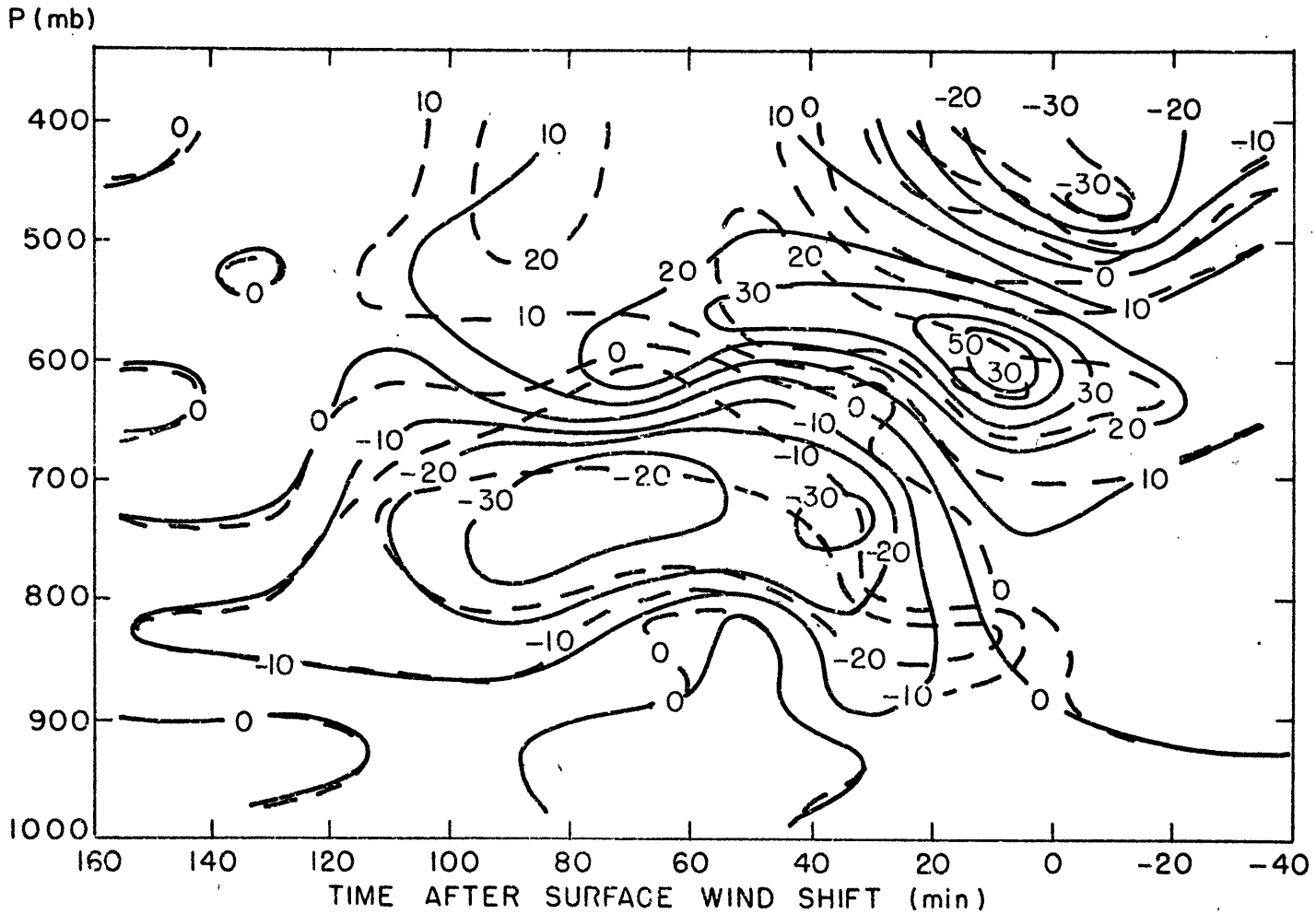

Fig. 17a. Similar to Fig. 15a, but for $\frac{\partial \bar{\theta}_e}{\partial t} + \frac{\partial}{\partial x}(\bar{u}\bar{\theta}_e) + \frac{\partial}{\partial y}(\bar{v}\bar{\theta}_e) + \frac{\partial}{\partial p}(\bar{\omega}\bar{\theta}_e)$, in units of $^{o}C\ min^{-1} \times 10^{-2}$.

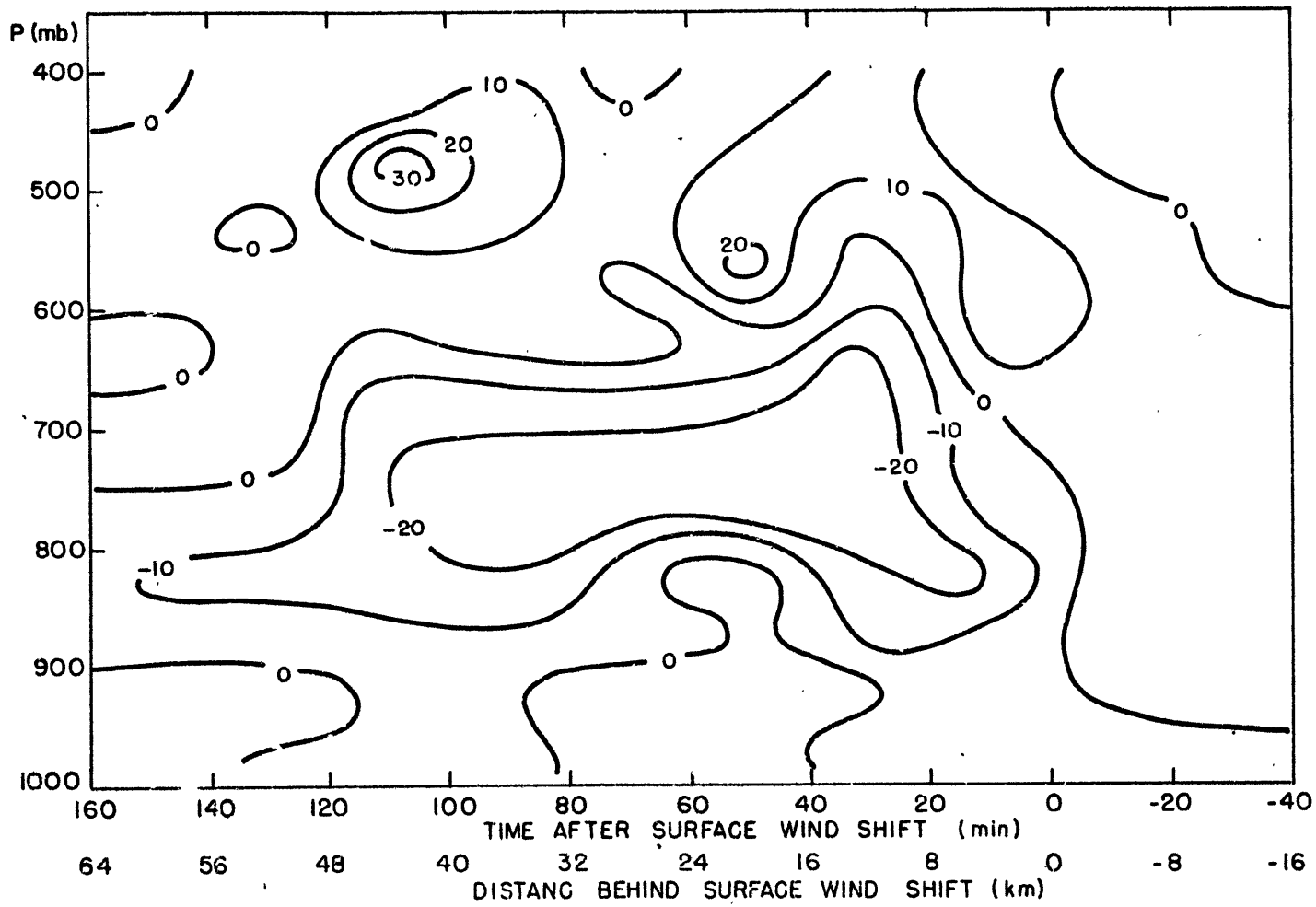

Fig. 17b. Same as Fig. 17a, but for version C.

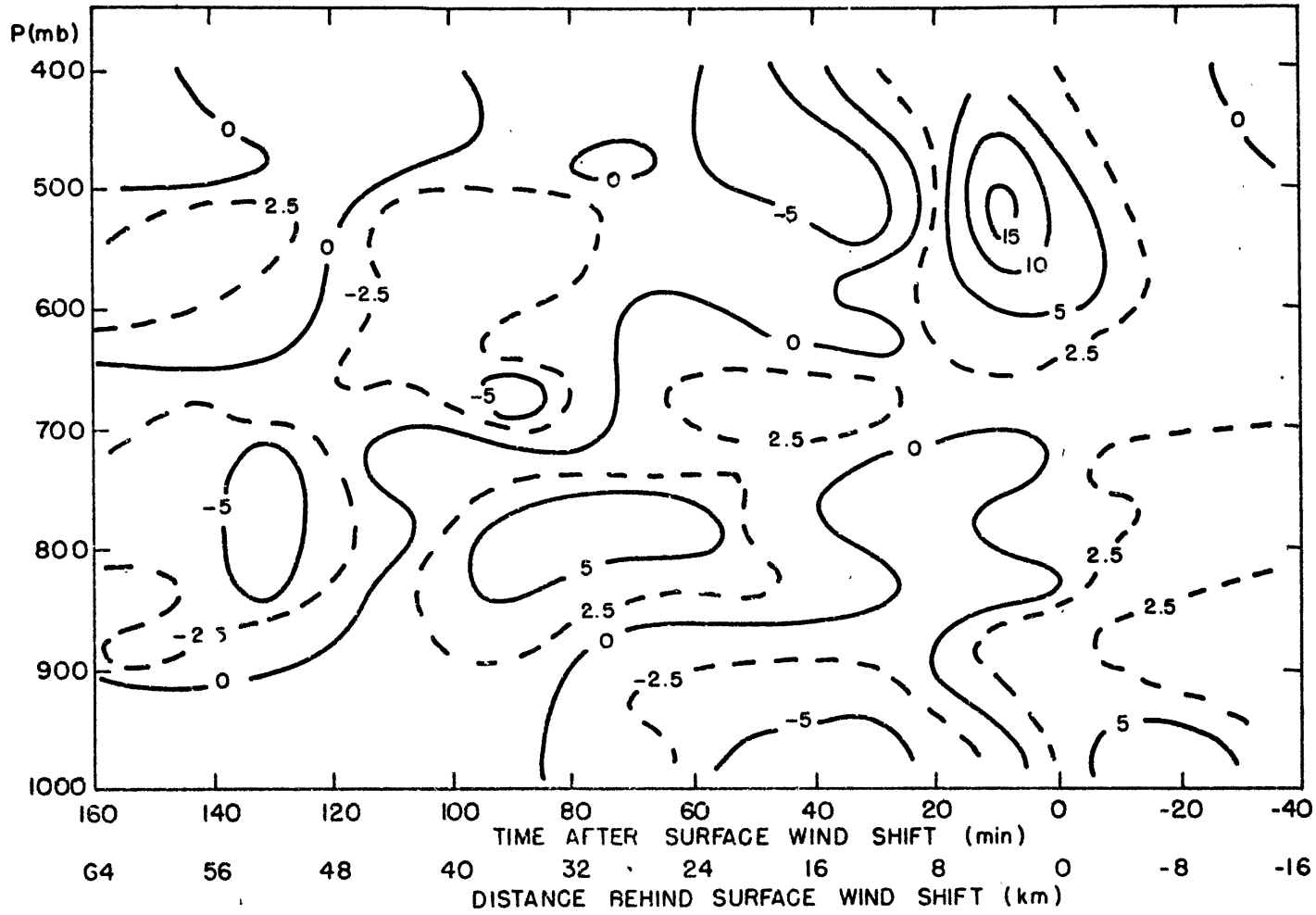

Fig. 18. Values of $\partial/\partial y(\overline{\theta_e' v'})$, in °C min^{-1} x 10^{-2}, determined from groups of about 10 observations each.

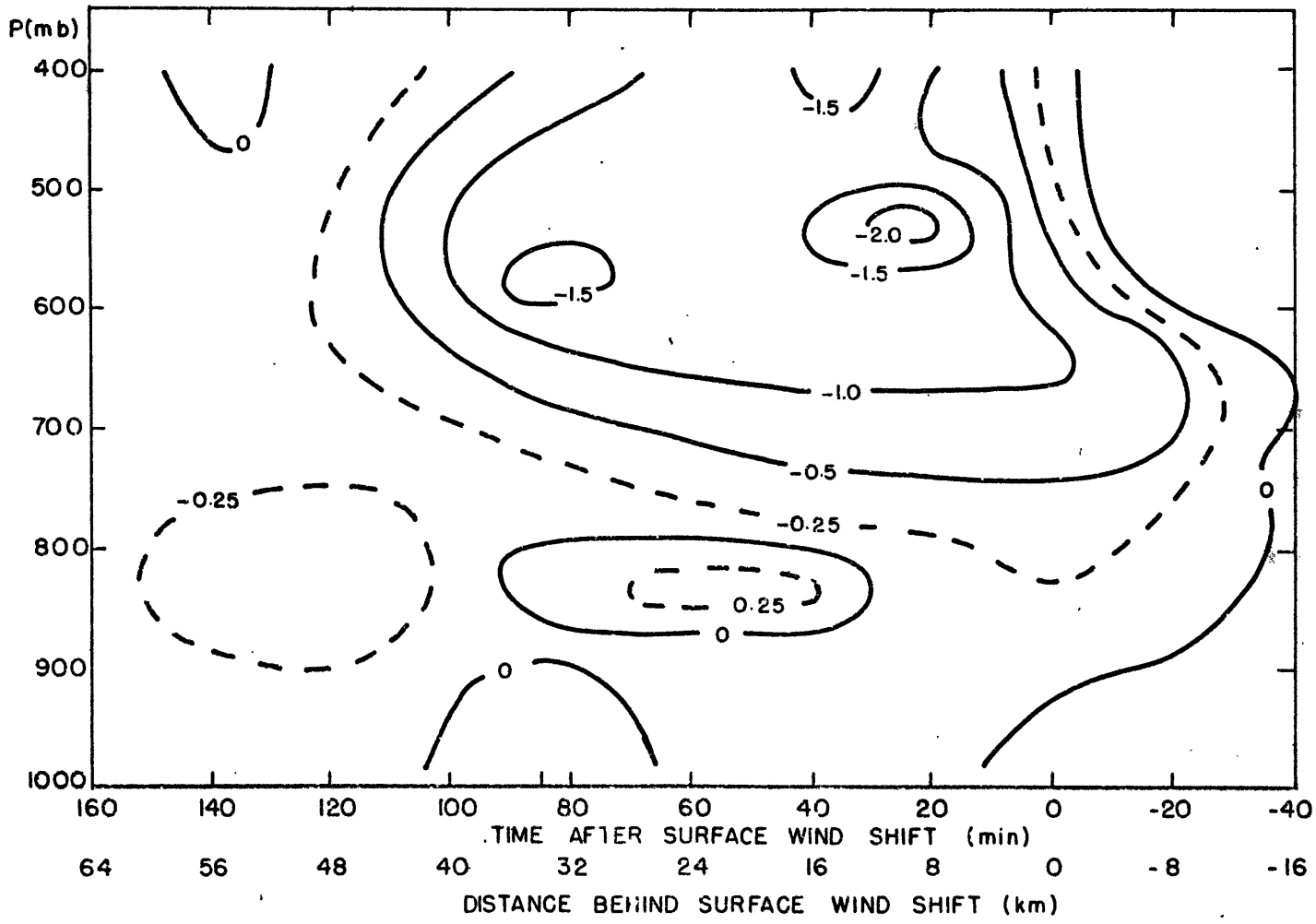

Fig. 19. Values of $\overline{\theta_e' \omega'}$ in $^{\circ}C$ mb sec^{-1}, determined from groups of about 10 observations each, using values of net balloon ascent rates for ω.

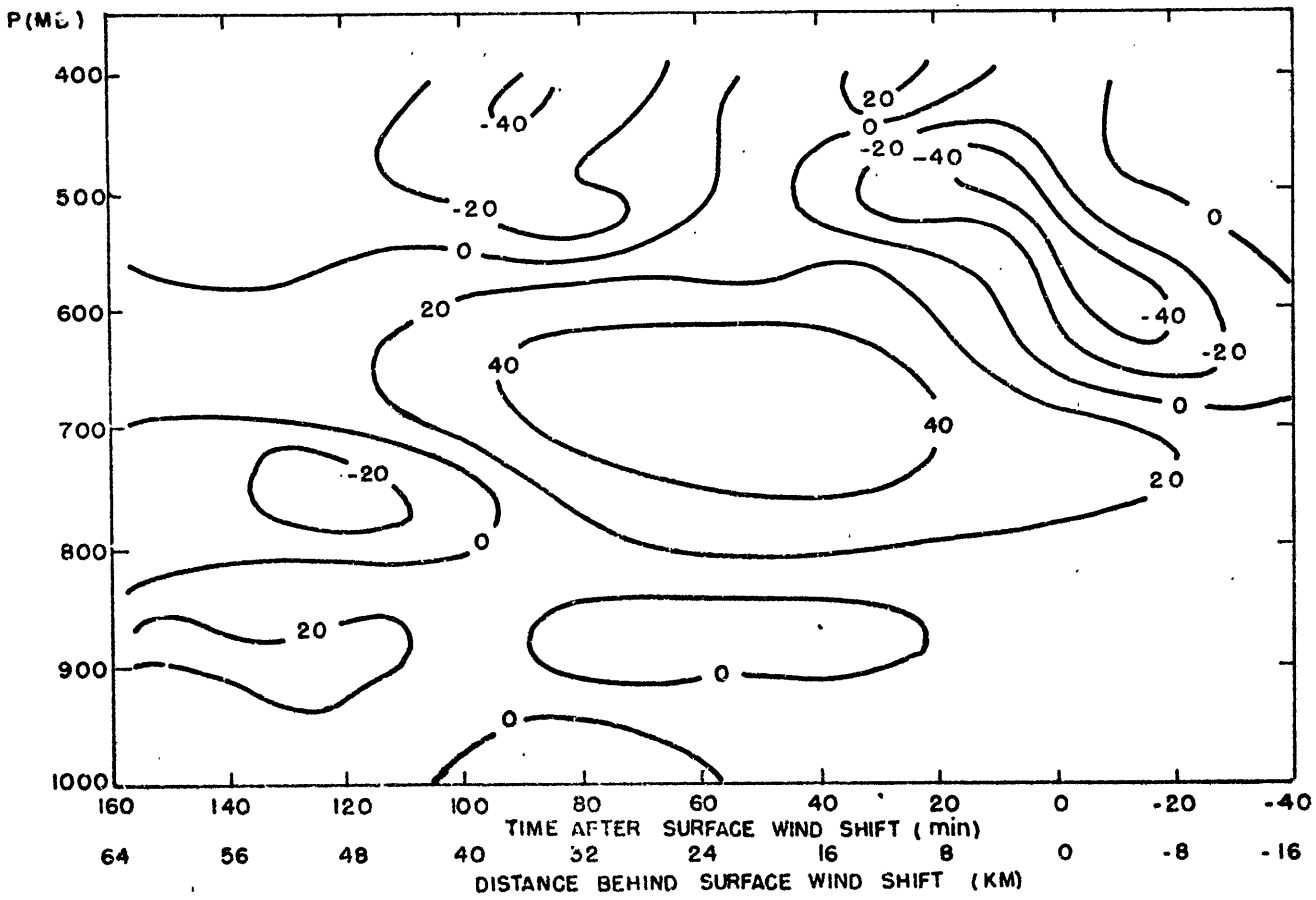

Fig. 20. Values of $\partial_p(\overline{\theta_e'\omega'})$ in °C min^{-1} x 10^{-2}, determined from Fig. 19.

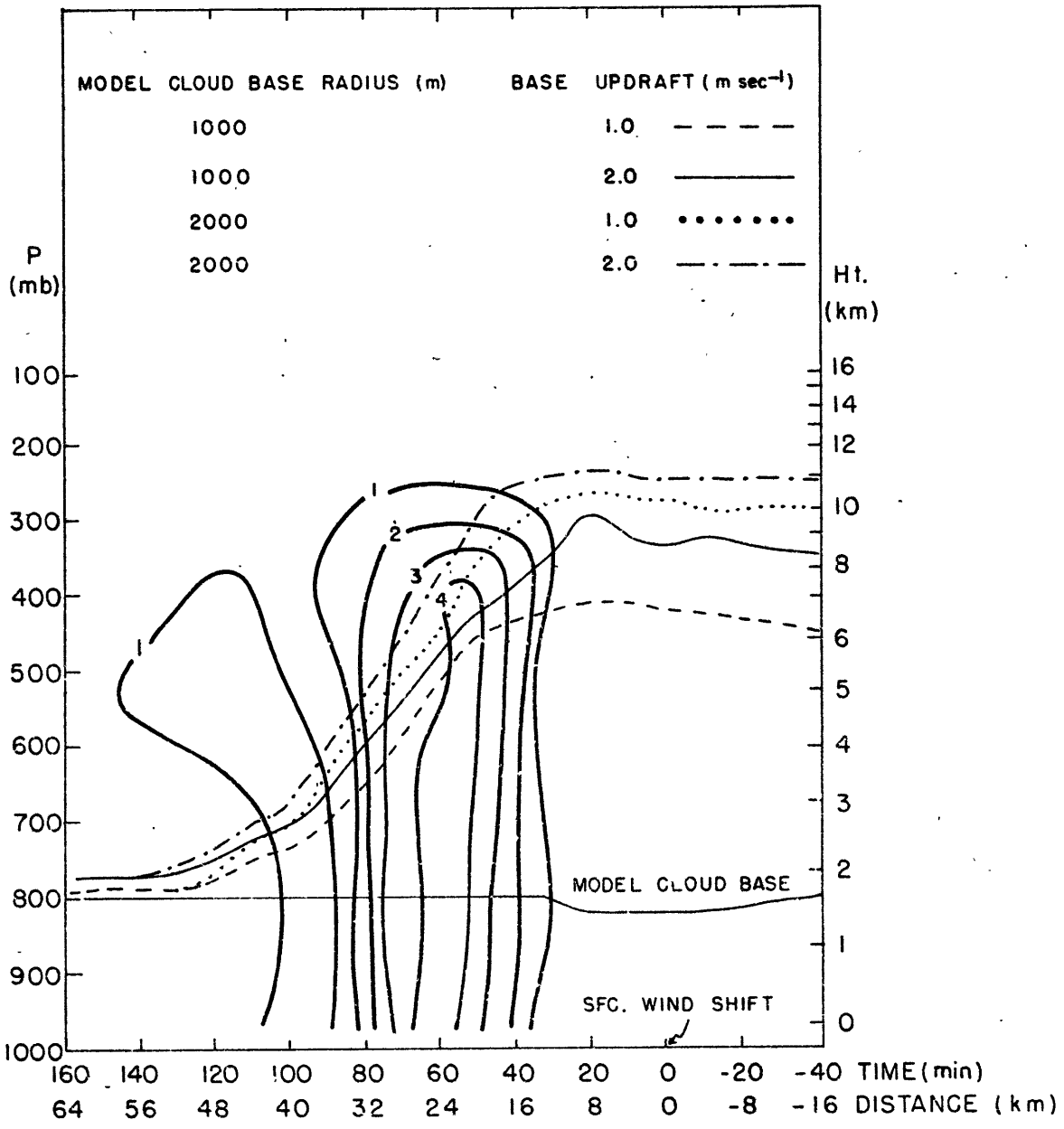

Fig. 21. A vertical cross section moving with the front in which heavy solid lines are radar RHI log Z_e contours at 1940 CST. Also pictured are cloud-top heights derived from the Squires-Turner model for various base conditions.

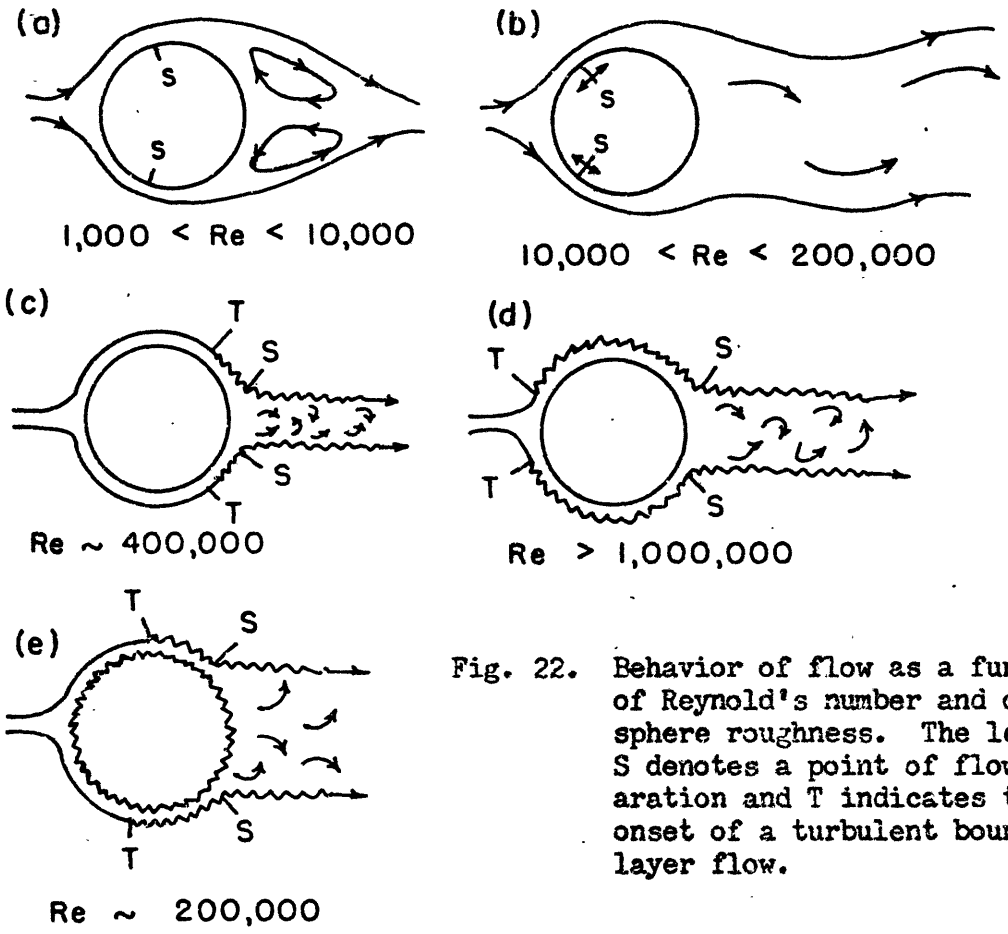

Fig. 22. Behavior of flow as a function of Reynold's number and of sphere roughness. The letter S denotes a point of flow separation and T indicates the onset of a turbulent boundary layer flow.

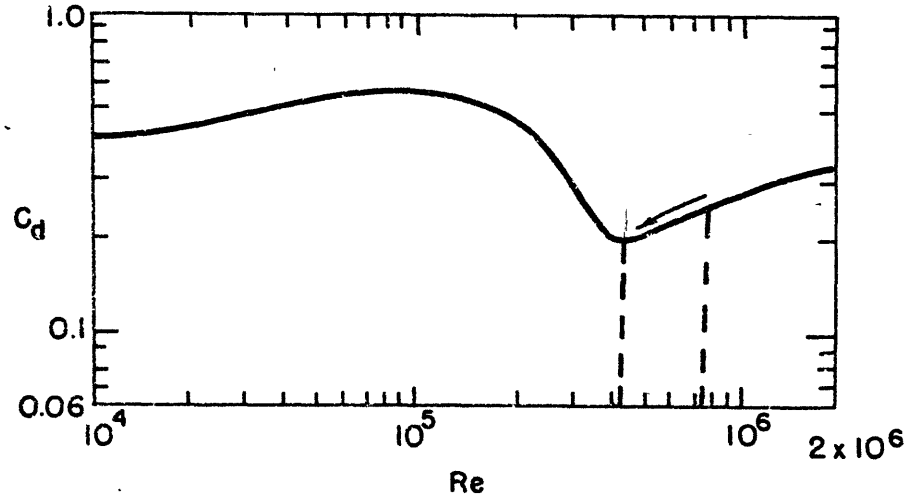

Fig. 23. The C_d versus Re relationship used for this case. The arrow indicates values of Re for a typical balloon during its ascent.

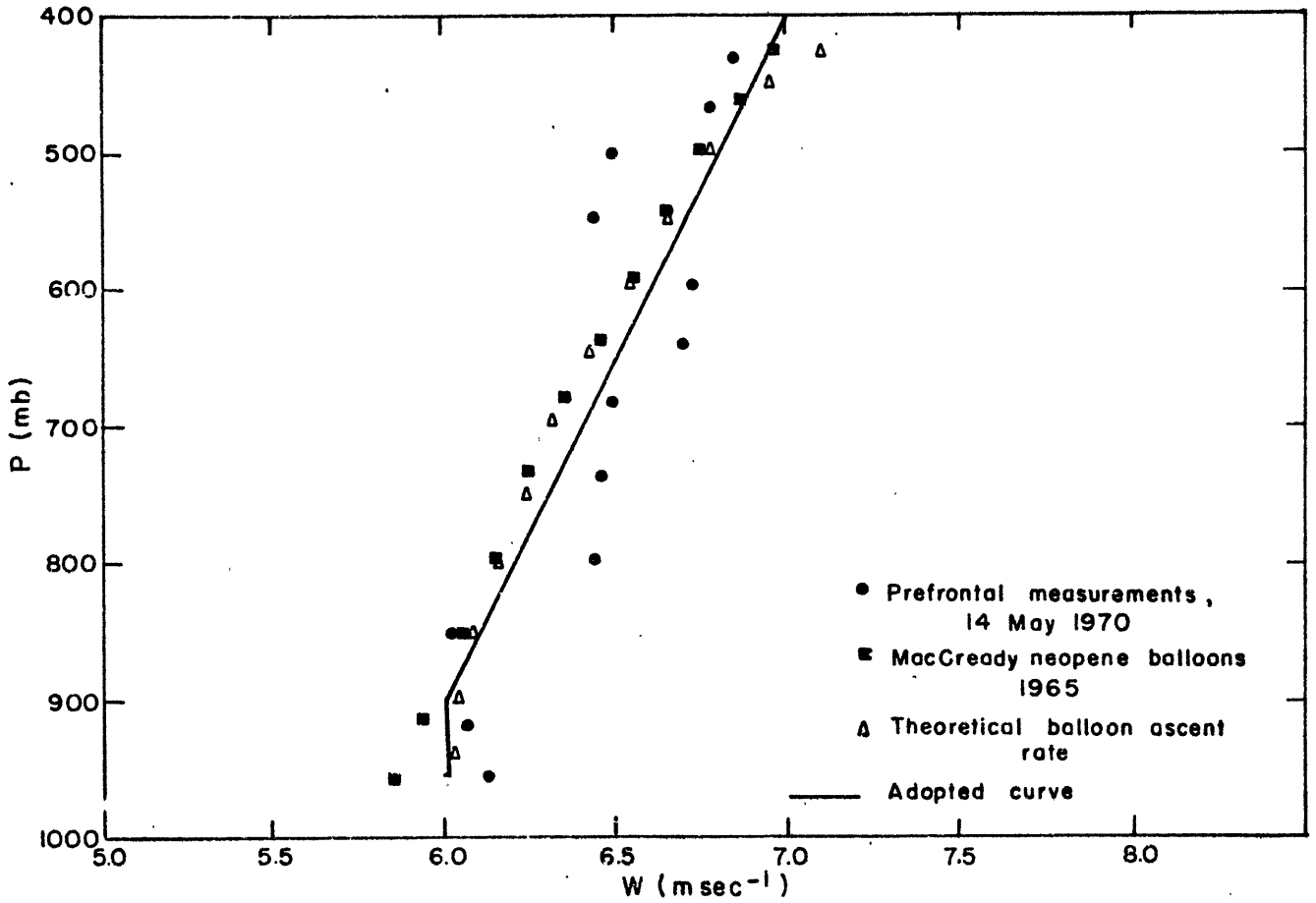

Fig. 24. Various estimates of ascent rates in still air for 2-m diameter balloons from experiments and theoretical considerations. The increase of still-air balloon ascent rate with height used in this study is taken from the solid curve.

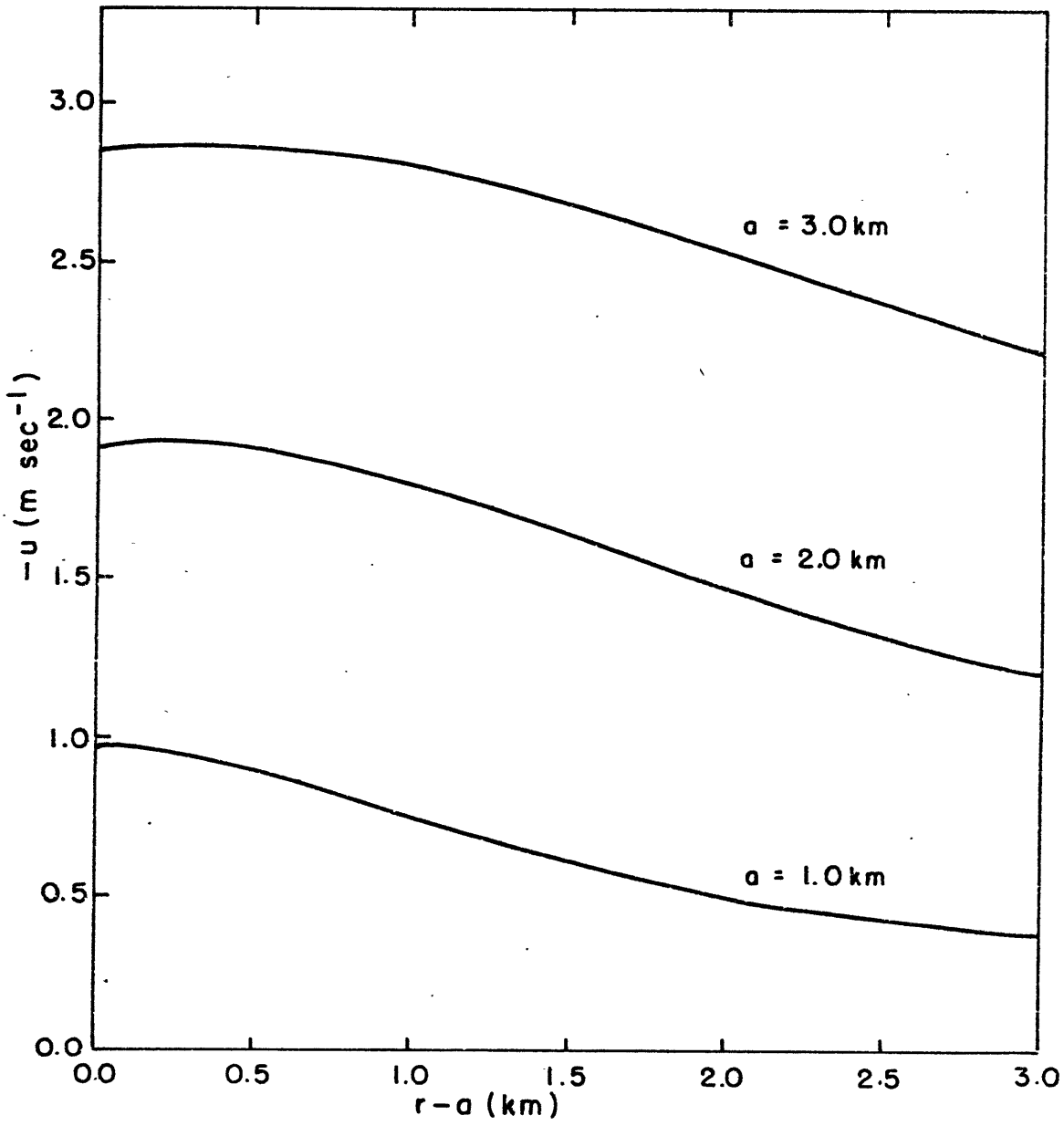

Fig. 25a. Inward entrainment velocities as a function of distance from the cloud's edge and of cloud radius.

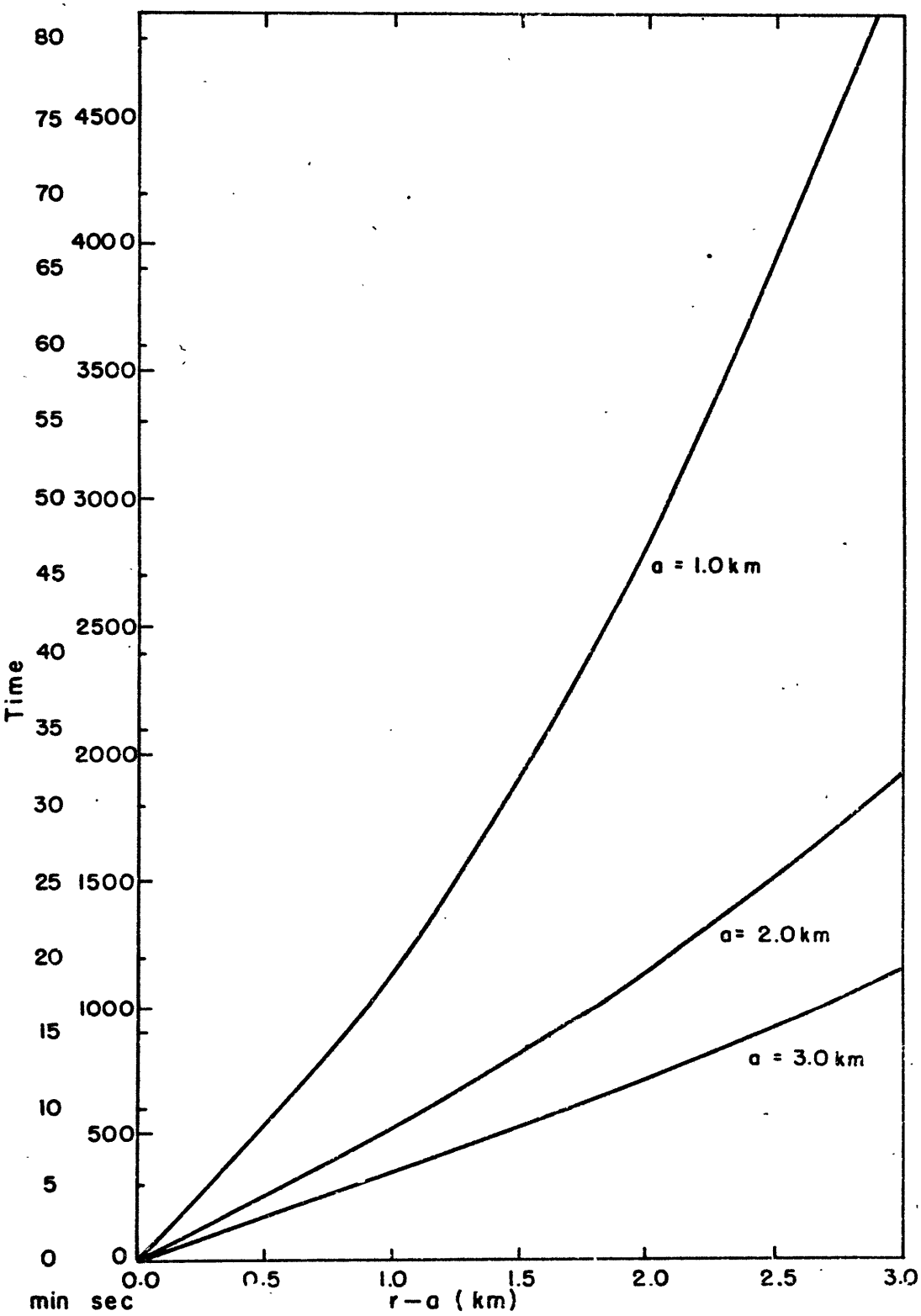

Fig. 25b. Time needed for a balloon to reach a model cloud as a function of distance from the cloud's edge and of cloud radius.

REFERENCES

Air Ministry Meteorological Office, 1961: Handbook of Meteorological Instruments. Part II, London, Her Majesty's Stationery Office, 209 pp.

Barnes, S. L., J. H. Henderson, and R. J. Ketchum, 1971: "Rawinsonde Observation and Processing Techniques at the National Severe Storms Laboratory." NOAA TM ERL-53. April, 1971.

Davies-Jones, Robert P., 1974: "Discussion of Measurements Inside High-Speed Thunderstorm Updrafts." Journal of Applied Meteorology. Vol. 13, pp. 710-717.

———— and James H. Henderson, 1973: "Characteristics of Thunderstorm Updraft Soundings." Preprints of the Eighth Conference on Severe Local Storms. October, 1973 Denver, Colorado. pp. 1-5.

Fankhauser, James C., 1969: "Convective Processes Resolved by a Mesoscale Rawinsonde Network." Journal of Applied Meteorology. Vol. 8, pp. 778-798.

———— , 1971: "Thunderstorm-Environment Interactions Determined from Aircraft and Radar Observations." Monthly Weather Review. Vol. 99, pp. 171-192.

———— , 1974: "The Derivation of Consistent Fields of Wind and Geopotential Height from Mesoscale Rawinsonde Data." Journal of Applied Meteorology. Vol. 13, pp. 637-646.

Henderson, James H., 1971: "The Internal Structure of a Thunderstorm as Revealed by θ_w Surfaces." Preprints of the Seventh Conference on Severe Local Storms. October, 1971, Kansas City, Missouri, pp. 234-239.

Lindzen, Richard S., 1974: Private communication.

Meneely, Jack M., 1972: "A Study of the Convective Storms of 14 May 1970 Using Data from the NSSL Rawinsonde Mesonetwork." S.M. Thesis. Dept. of Meteorology, MIT, 100 pp.

MacCready, Paul B., 1965: "Comparison of Some Balloon Techniques." Journal of Applied Meteorology. Vol. 4, pp. 504-508.

———— and Henry R. Jex, 1964: "Study of Sphere Motion and Balloon Wind Sensors." NASA TM X-53089, 40 pp.

Newton, Chester W. and Harriet R. Newton, 1959: "Dynamical Interactions between Large Convective Clouds and Environment with Vertical Wind Shear." Journal of Meteorology. Vol. 16, pp. 483-496.

O'Brien, J. J., 1970: "Alternative Solutions to the Classical Vertical Velocity Problem." Journal of Applied Meteorology. Vol. 9, pp. 197-203.

Ogura, Y., 1963: "The Evolution of a Moist Convective Element in a Shallow, Conditionally Unstable Atmosphere: A Numerical Calculation." Journal of the Atmospheric Sciences. Vol. 20, pp. 407-424.

Phillips, Norman A., 1973: Introduction to Dynamical Meteorology. MIT class notes (19.61).

Squires, P. and J. S. Turner, 1962: "An Entraining Jet Model for Cumulonimbus Updraughts." Tellus. Vol. 14, pp. 422-434.

Wonnacott, Thomas H. and Ronald J. Wonnacott, 1972: Introductory Statistics. 2nd. ed. New York: John Wiley & Sons, Inc., 510 pp.

Yanai, M., S. Esbensen, and J. Chu, 1973: "Determination of Bulk Properties of Tropical Cloud Clusters from Large-Scale Heat and Moisture Budgets." Journal of the Atmospheric Sciences. Vol. 30, pp. 611-627.